RICE UNIVERSITY

Effects of bubble coalescene, permeability, and degassing process on the transition from explosive to effusive eruption of rhyolitic magma

by

Chinh Thuc Nguyen

A THESIS SUBMITTED
IN PARTIAL FULFILLMENT OF THE
REQUIREMENTS FOR THE DEGREE

Doctor of Philosophy

APPROVED, THESIS COMMITTEE:

Helge M. Gonnermann, Chair
Associate Professor, Department of Earth Science, Rice University

Adrian Lenardic
Professor, Department of Earth Science, Rice University

Brandon Dugan
Associate Professor, Department of Earth Science, Rice University

George J. Hirasaki
Professor, Department of Chemical and Biomolecular Engineering, Rice University

Houston, Texas
April, 2016

ACKNOWLEDGEMENTS

First and foremost, I would like to thank my advisor, Dr. Helge Gonnermann, in guiding me throughout my doctorate program and also in the completion of this thesis. I came to Rice with little knowledge of volcanology and have learned a lot about physical volcanology, ideas to design laboratory experiments as well as writing and publishing peer-reviewed papers. His time and patience in explaining basic knowledge as well as guiding to understand fluid dynamic principles are very much appreciated.

I would like to thank Dr. Adrian Lenardic, Dr. Brandon Dugan and Dr. George Hirasaki for agreeing to be in my graduate committee as well as their feedbacks in the completion of my thesis. I appreciate their teaching in several classes I have taken, or their research advice. I also would like to thank my collaborators in sharing ideas and publishing journal papers, including Dr. Christian Huber, Dr. Joe Dufek, Dr. Andrew Gouldstone, Dr. Michael Manga as well as Anthony Maiorano, Yang Chen and Carolina Munoz. I specially thank Dr. Bruce Houghton and Dr. Rebecca Carey not only for their excellent collaboration but also providing me many volcanic samples to make my research possible. An extended thank to Dr. Juli Morgan for showing me how to enjoy teaching the introduction class in Earth science. I enjoyed working with her and have learned a lot from her.

Throughout my time at Rice, I have enjoyed many long discussions, both in research and in daily life, with my research group and other fellow students. Special thanks to Pranabendu Moitra, Austin Blaser, Sahand Hazimirza, Thomas Giachetti, Chiara Montagna and Amalia Bonanno for their friendship, research critics, advice and support during difficult times. I also extend my thanks to several undergraduate students who have assisted me in many laboratory experiments, both failed and successful. Those include Yang Chen, Josh Crozier, Sarah Gerenday and Sofia Avendano.

I also would like to thank all the staff who have helped me during my time at

Rice, Dr. Mary Ann Lebar, Ms. Bonnie Hoffman, Ms. Soookie Sanchez, Ms. Pat Jordan, Ms. Lee Wilson and Ms. Sandra Flechsig, as well as Dr. Sherry Vanderslice in the Graduate Office. My special thanks to Mr. Dwight Dear and Mr. Eliberto Batres for helping me with machine shop which was very useful for my scientific experiments, especially when you spent extra time and efforts to help me and my guests.

Finally, I would like to thank my family for their support. My special dedication to my grandfather and my father for implanting in me the curiosity to understand the world surrounding us at a young age. Without their encouragement and support, I would not have accomplished what I have today.

ABSTRACT

Effects of bubble coalescene, permeability, and degassing process on the transition from explosive to effusive eruption of rhyolitic magma

by

Chinh Thuc Nguyen

This thesis consists of two parts that address bubble coalescence and the degassing process inside the magma conduit during volcanic eruptions. The first part focuses on analog fluid experiments and resultant scalings for bubble coalescence, due to gravitational and capillary forces, with application to magmatic systems. I find that film drainage is due to capillary forces at dimensionless Bond numbers, Bo < 0.25, whereas gravitational forces result in film thinning at Bo > 0.25. The film drainage time scale is given by $t \sim C\ ln(\alpha)\,\tau$, and is orders of magnitude faster than previously assumed for magmatic systems. Here $C \sim 10$ is an empirical constant, α is the ratio of initial film thickness to film thickness at the time of rupture, and τ is the characteristic capillary or buoyancy time scale at values of Bo < 0.25 and Bo > 0.25, respectively. These scalings could be used to estimate the time for bubble coalescence under static conditions, such as in a magma chamber or post-fragmentation in pyroclasts.

The second part of the thesis focuses on pyroclast permeability, a consequence of bubble coalescence during volcanic eruptions. I analyze porosity and permeability of rhyolitic pyroclasts from four different Plinian eruptions. One of these is the A.D. 1912 eruption of Novarupta volcano, Alaska, which is comprised of five

different episodes ranging from explosive to effusive activity. For this eruption, I find that the degree of interconnectivity, measured as the ratio of connected to total porosity, decreases with phenocryst content and with increasing eruption intensity. Through numerical modeling of diffusive bubble growth during eruptive magma ascent, I conclude that magma permeability is unlikely a sufficient condition for the transition from explosive to effusive activity. Instead, it is likely that a decrease in magma ascent leads to the transition from explosive to effusive activity during the waning stages of the eruption. Subsequently, I compare and contrast the porosity and permeability data from all four Plinian eruptions investigated: the A.D. 181 Taupo eruption, New Zealand; the A.D. 1060 Glass Mountain eruption, California; the A.D. 1314 Kaharoa eruption; and the A.D. 1912 Novarupta eruption, Alaska. I find that the Kaharoa samples have the lowest values of porosity and permeability of these four Plinian eruptions. Porosity and permeability, as well as pyroclastic textures of Kaharoa samples closely resemble those of the effusive Episode V of the 1912 Novarupta eruption. I hypothesize that the Kaharoa eruption might have undergone a high degree of open-system degassing.

Contents

Illustrations

Tables

Chapter 1

Introduction

Decrease in pressure during magma ascent leads to a reduction in volatile solubility, as a consequence volatiles exsolve into a gas phase to form bubbles (e.g., *Sparks*, 1978; *Toramaru*, 1989). Volatile exsolution, in particular water, increases magma viscosity. This adversely affects bubble growth, leading to a build-up of bubble overpressure, which is the difference between gas pressure inside bubbles and surrounding melt pressure. When the overpressure exceeds the tensile strength of the magma, it will fragment the magma, resulting in an explosive eruption (Figure 1.1). Bubble coalescence, on the other hand, may form interconnected pathways through which magmatic gases can flow out of the magma, thereby reducing gas pressure (e.g., *Eichelberger et al.*, 1986; *Rust and Cashman*, 2011; *Castro et al.*, 2012). Therefore, bubble coalescence may play a crucial role in eruption dynamics and intensity. This dissertation consists of two parts that investigate bubble coalescence during volcanic eruptions, as well as the resultant permeable flow of magmatic gases during Plinian eruptions.

Due to a lack of direct observation of magmatic processes inside the volcanic conduit during eruptions, volcanologists have to reconstruct these processes from the eruptive products, in conjunction with laboratory experiments and numerical models. The process under consideration herein is bubble coalescence rate. Specifically, the time it takes for inter-bubble liquid (melt) films to drain under conditions of no bubble growth or external deformation. In the first part of my thesis, I quan-

tify film drainage time using dimensionless Bond number, a ratio of gravitational forces to capillary forces. Cooling times of pyroclasts have been estimated to be within seconds to minutes (e.g., *Thomas and Sparks*, 1992; *Hort and Gardner*, 1998), whereas film drainage times for rhyolitic melts in this study are estimated to be within days to years. Therefore vesicle interconnectivity and, hence, permeability measured in pyroclasts is likely a good representation of magma permeability at the time of fragmentation. This work is presented in Chapter 2 and was published in *Nguyen et al.* (2013).

Abrupt transitions from explosive to effusive episodes are commonly observed in Plinian eruptions. It has been a subject of debate to what extent the onset of magma permeability and subsequent gas loss affect these transitions. In the second part of my thesis, I analyze pyroclasts from Plinian eruptions because they record magma permeability at the time of magma fragmentation. In Chapter 3, I present this analysis of porosity and permeability, as well as textural observation of pyroclasts from all five well-constrained eruptive episodes of the 1912 Novarupta eruption, which range from explosive to effusive activity. I investigate the effects of magma permeability and ascent rate on the explosive-effusive transition using numerical modeling of diffusive bubble growth coupled with conduit flow. This work was published in *Nguyen et al.* (2014).

To assess the variability in open-system degassing on the transition from explosive to effusive eruptions, I compare and contrast porosity and permeability data from four different Plinian eruptions: the A.D. 1912 eruption of Novarupta volcano, Alaska; the A.D. 1314 Kaharoa eruption, New Zealand; the A.D. 1060 Glass Mountain eruption, Northern California and the A.D. 181 Taupo eruption, New Zealand. This work is presented in Chapter 4.

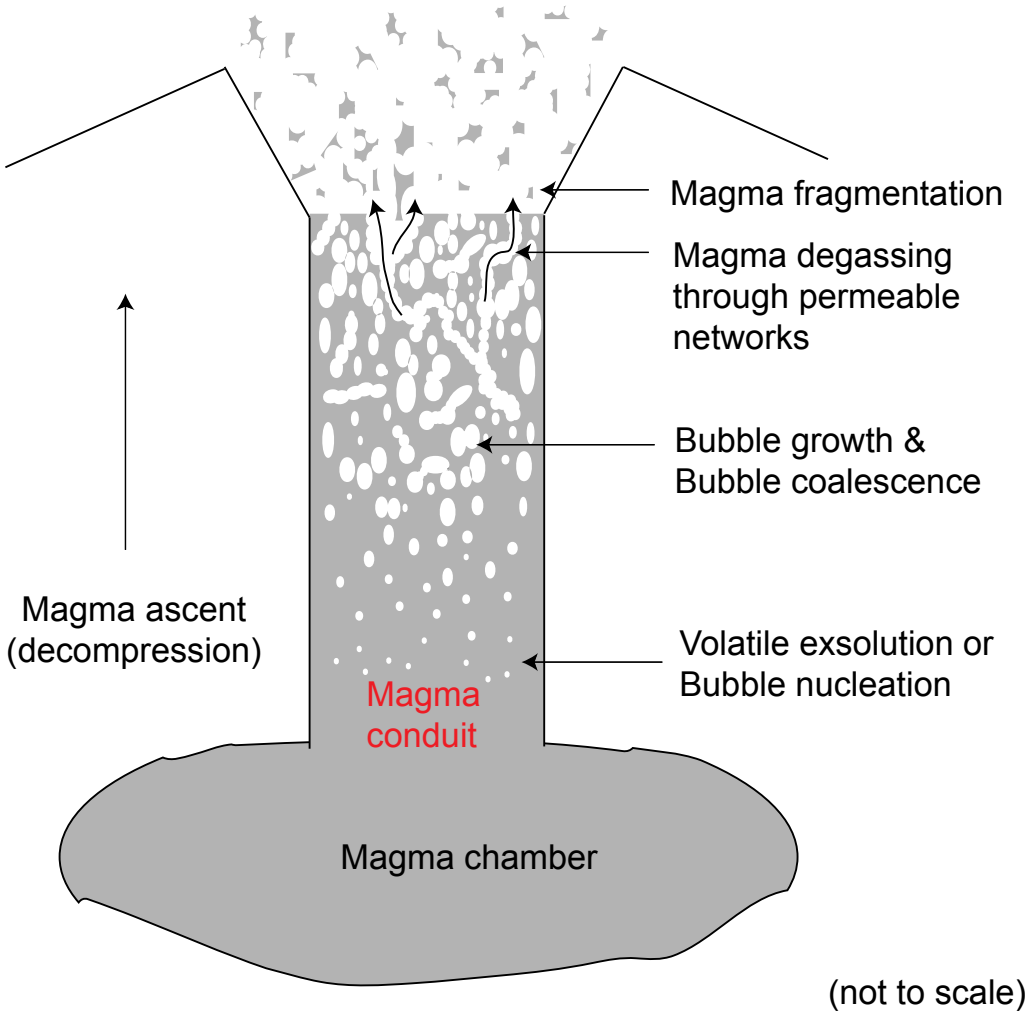

Figure 1.1 : A schematic diagram illustrating a sequence of a typical explosive volcanic eruption, from bubble nucleation, growth, coalescence to the development of magma permeability, open-system degassing and fragmentation.

I

Chapter 2

Film drainage and the lifetime of bubbles

†This Chapter has been edited, reformatted and reprinted from Nguyen, C.T., H. M. Gonnermann, Y. Chen, C. Huber, A. A. Maiorano, A. Gouldstone, and J. Dufek (2013), Film drainage and the lifetime of bubbles. Geochemistry, Geophysics, Geosystems, 14(9), 1-16, doi: 10.1002/ggg3.20198, American Geophysical Union.

I present the results of new laboratory experiments that provide constraints on inter-bubble film thinning and bubble coalescence as a consequence of liquid expulsion by gravitational and capillary forces. To ensure dynamic similarity to magmatic systems, the experiments are at small Reynolds numbers (Re $\ll 1$) and cover a wide range of Bond numbers ($10^{-3} \leq$ Bo $\leq 10^{2}$). Results indicate that at Bo< 0.25 film drainage is due to capillary forces, whereas at Bo> 0.25 gravitational forces result in film thinning. The film drainage time scale is given by $t \sim C\, ln(\alpha)\, \tau$, and is orders of magnitude faster than often assumed for magmatic systems. Here $C \sim 10$ is an empirical constant and α is the ratio of initial film thickness to film thickness at the time of rupture and τ is the characteristic capillary or buoyancy time scale at values of Bo< 0.25 and Bo> 0.25, respectively.

2.1 Introduction

Magmatic processes that govern explosive volcanic eruptions are largely inaccessible to direct observation. To reconstruct the subsurface processes that determine

eruptive style and intensity, scientists rely on indirect observations and direct observations from eruptive products, that are pyroclasts. Of fundamental importance for volcanic eruptions are magmatic volatiles and their exsolution because they affect magma buoyancy (e.g., *Gonnermann and Manga*, 2007), magma rheology (e.g., *Stein and Spera*, 1992; *Manga et al.*, 1998; *Rust and Manga*, 2002; *Pal*, 2003; *Llewellin and Manga*, 2005), as well as the potential energy required for explosive eruptive behaviors (e.g., *Sparks*, 1978; *Alidibirov and Dingwell*, 2000; *Spieler et al.*, 2004; *Koyaguchi and Mitani*, 2005; *Namiki and Manga*, 2005; *Mueller et al.*, 2008; *Koyaguchi et al.*, 2008; *Namiki and Manga*, 2008; *Alatorre-Ibargüengoitia et al.*, 2010).

Volatile exsolution results in the formation of bubbles within the ascending magma, which may become preserved as vesicles in pyroclasts. Fundamental properties of pyroclasts are therefore the volume fraction of vesicles and their size distribution (e.g., *Sparks*, 1978; *Sparks and Brazier*, 1982; *Whitham and Sparks*, 1986; *Houghton and Wilson*, 1989; *Toramaru*, 1989, 1990; *Cashman and Mangan*, 1994; *Blower et al.*, 2003; *Burgisser and Gardner*, 2005). They are thought to provide fundamental constraints on the magma vesiculation process and by inference on magma ascent rates and dynamics (e.g., *Rutherford and Hill*, 1993; *Lovejoy et al.*, 2004; *Gaonac'h et al.*, 2005; *Toramaru*, 2006; *Blundy and Cashman*, 2008; *Rutherford*, 2008; *Gonnermann and Houghton*, 2012). Vesicle volume fraction and size distribution are thought to provide a time-integrated record of syneruptive bubble nucleation, bubble growth, bubble coalescence and open-system degassing through permeable bubble networks that are formed by bubble coalescence (e.g., *Eichelberger et al.*, 1986; *Westrich and Eichelberger*, 1994a; *Klug and Cashman*, 1996; *Saar and Manga*, 1999; **?**; *Burgisser and Gardner*, 2005; *Okumura et al.*, 2006; *Wright et al.*, 2006; *Namiki and Manga*, 2008; *Okumura et al.*, 2008; *Wright et al.*, 2009; *Rust and Cashman*, 2011; *Castro et al.*, 2012).

Of these three processes - nucleation, growth and coalescence - bubble coalescence is perhaps the most difficult one to reconstruct quantitatively from vesicle size distributions, in part because of a relative dearth of rigorous quantitative constraints on coalescence rates (e.g., *Herd and Pinkerton*, 1997; *Klug and Cashman*, 1996; *Klug et al.*, 2002; *Lovejoy et al.*, 2004; *Gaonac'h et al.*, 2005; *Burgisser and Gardner*, 2005; *Gardner*, 2007; *Bai et al.*, 2008; *Gonde et al.*, 2011; *Castro et al.*, 2012). Not only is this of importance for the eruptive process itself, but also to assess the extent to which vesicles record bubble coalescence during the time interval between pyroclast formation by magma fragmentation and quenching.

The objective of this study is to provide some new constraints on bubble coalescence rates. Coalescence is the process whereby the liquid film that separates adjacent bubbles thins and ruptures, transforming two or more individual bubbles into a single bubble of larger size (*Chan et al.*, 2011, and references therein). Because coalescence is a consequence of thinning of the liquid film that separates bubbles, the rates of film thinning under different conditions of driving and resisting forces provide a fundamental constraint on bubble coalescence rates and will be the focus of this study.

Film thinning can be caused by liquid expulsion due to (1) gravitational forces, associated with the density difference between bubbles and surrounding liquid (e.g., *Jones and Wilson*, 1978; *Proussevitch et al.*, 1993a; *Debrégeas et al.*, 1998); (2) capillary forces (e.g., *Proussevitch et al.*, 1993a); (3) bubble growth, due to decompression or diffusion of dissolved gases from the liquid to bubbles (e.g., *Gardner*, 2007); as well as (4) shearing induced by the flow of the entire suspension, for example during magma ascent (e.g., *Okumura et al.*, 2006, 2008; *Castro et al.*, 2012), or perhaps induced by bubble coalescence itself (e.g., *Martula et al.*, 2000).

Here I present new results of laboratory experiments on film drainage of "bare" viscous bubbles (*Debrégeas et al.*, 1998), as a consequence of liquid expulsion (drainage) by both gravitational and capillary forces. The results of my experiments provide a base case against which experiments or predictions of bubble coalescence in more complicated cases, for example those involving multiple bubbles or growing bubbles, can be compared. Figure 2.1 illustrates the analogy between such film drainage in experiments and vesicular magmas, as preserved in pyroclasts. We refer the reader to Section 2.2 for a general introduction to film drainage and to Section 2.3 for a detailed discussion of our experiments, including the similarity between film drainage in our experiments and in magmas. I discuss our experimental results in Section 3.6 and provide a brief discussion of potential applications of our results to magmatic systems in Section 2.5.

2.2 Film Drainage

2.2.1 Previous Work

The drainage of liquid films has been studied extensively (e.g., *Charles and Mason*, 1960; *Princen*, 1963; *Hartland*, 1970). In my experiments the film was the surfactant-free liquid layer surrounding a stationary air bubble suspended beneath the free surface of a liquid layer. Formulations for the variation in film thickness, δ, with time, t, have been derived from lubrication theory under the assumption of immobile interfaces, that is no-slip boundaries on either side of the liquid film (e.g., Figure 2.2a; *Charles and Mason*, 1960; *Hartland*, 1970; *Ivanov and Traykov*, 1976; *Toramaru*, 1988; *Proussevitch et al.*, 1993a)

$$t \sim \frac{3n^2}{16\pi}\frac{\eta A^2}{F}\left(\frac{1}{\delta^2}-\frac{1}{\delta_0^2}\right). \tag{2.1}$$

Here $\delta = \delta_0$ when $t = 0$, $A \approx \pi R^2$ is the area of the draining film, R is the bubble radius, and η is the liquid viscosity. F is the force, either gravitational or capillary, acting on the drop and causing film drainage, and n is the number of immobile film interfaces.

For $n = 2$, a strongly stabilizing surfactant layer or other impurities cause both sides of the liquid film to be immobile. The velocity of the liquid within the film approaches zero at the interfaces and the resultant flow approximates to a Hagen-Poiseuille velocity profile (e.g., *Lee and Hodgson*, 1968). In the absence of surfactants or other impurities that may change the film interfaces from being a completely free-slip boundary, it is expected that $n \ll 2$ (*Hartland*, 1970). In this case, the flow within the film should be a plug flow (e.g., Figure 2.2b; *Lee and Hodgson*, 1968). In practice, many applications may involve partially mobile interfaces (e.g., *Chesters and Hofman*, 1982; *Chesters*, 2009; *Yiantsios and Davis*, 1991; *Abid and Chesters*, 1994; *Oldenziel et al.*, 2012) with some intermediate value of n in the range of $0 < n < 2$.

Precise values of n for bubbles in magmas, where the film interfaces may not be immobile, do not exist and it has typically been assumed that $n = 2$ (*Toramaru*, 1988; *Proussevitch et al.*, 1993a; *Klug et al.*, 2002; *Cashman and Mangan*, 1994; *Klug and Cashman*, 1996; *Mangan and Cashman*, 1996; *Cruz and Chouet*, 1997; *Navon and Lyakhovsky*, 1998; *Castro et al.*, 2012). I will subsequently show that this can result in significant inaccuracies of estimated film drainage times.

2.2.2 The Capillary Length

If $R \ll \sqrt{\sigma/\Delta\rho g}$, film drainage and bubble coalescence (neglecting bubble growth and deformation) are expected to be a consequence of capillary film drainage, with $F = 2\pi\sigma A/R$. Here $\Delta\rho$ is the density difference between bubble and surrounding

liquid, g is the acceleration due to gravity and σ is surface tension.

In contrast, for $R \gg \sqrt{\sigma/\Delta\rho g}$, gravitational drainage is expected to dominate and $F = 4\pi R^3 \Delta\rho g/3$ *Charles and Mason* (1960); *Hartland* (1970). The length scale

$$\lambda = \sqrt{\sigma/\Delta\rho g} \tag{2.2}$$

is called the capillary length and for bubbles in silicate melts it is thought to be of the order of 1 mm (*Proussevitch et al.*, 1993a).

2.2.3 Gravitational Drainage of "Bare" Viscous Bubbles

Consistent with previous results (*Debrégeas et al.*, 1998; *van der Schaaf and Beerkens*, 2006), I find that in the absence of any surfactants or impurities, Equation (2.1) does not reproduce the experimentally observed rates of gravitational film drainage, even for very small values of n (e.g., *Davis and Smith*, 1976; *Traykov et al.*, 1977).

An alternate equation for the lifetime of such "bare" viscous bubbles, where films are not protected by surfactants or impurities, is based on fully mobile film interfaces (*Debrégeas et al.*, 1998; *van der Schaaf and Beerkens*, 2006). Consider a buoyant bubble of radius R, surrounded by a liquid film beneath a free surface (Figure 2.1a). Assuming a longitudinally uniform film thickness ($\partial\delta/\partial\phi = 0$) and velocity within the film ($\partial u/\partial\phi = 0$), an equation for the drainage velocity is given by

$$u(\theta) = c(\theta)\frac{1}{\eta}\Delta\rho g R^2, \tag{2.3}$$

where c is a parameter that depends on the latitudinal position θ and the driving force for film drainage is given by $F = 4\pi R^3 \Delta\rho g/3$. Local mass conservation, assuming that the liquid is incompressible, leads to

$$\frac{1}{R}\frac{\partial(\delta u)}{\partial\theta} + \frac{\partial\delta}{\partial t} = 0, \tag{2.4}$$

where δ is the film thickness. Substituting equation (2.3) in the continuity equation leads to

$$\left.\frac{d\delta}{dt}\right|_{\theta=0} = -\frac{1}{C_g}\frac{\delta\Delta\rho g R}{\eta}, \tag{2.5}$$

where $u = 0$ at $\theta = 0$. Integration with separation of variables (*Debrégeas et al.*, 1998; *van der Schaaf and Beerkens*, 2006) results in

$$t_g = C_g \ln\left(\frac{\delta_0}{\delta_f}\right)\underbrace{\frac{\eta}{\Delta\rho g R}}_{\tau_g}. \tag{2.6}$$

Here, t_g is the time required for gravitational film drainage at the apex of the bubble from an initial thickness, δ_0, to a final thickness, δ_f, at which spontaneous rupture occurs. $\tau_g = \eta/(\Delta\rho g R)$ is the characteristic buoyancy time scale and C_g is an empirical constant.

2.2.4 Capillary Drainage of "Bare" Viscous Bubbles

In magmas, bubble sizes may range over many orders of magnitude, often with $R \ll \lambda$. In the absence of bubble growth, coalescence at $R < \lambda$ is a consequence of capillary film drainage (Figure 2.1b), which is not well constrained by experiments, because of the difficulty of working with bubbles at the required small values of R and Bo (see Section 2.3.2). Here we show that the general form of Equation (2.6) also applies for film drainage of bare viscous bubbles at $R \ll \lambda$.

Using a similar approach to the derivation of Equation (2.6), I obtain for the velocity of the melt film

$$u(\theta) = c(\theta)\,\frac{1}{\eta}\sigma, \tag{2.7}$$

where the driving force that generates the flow is due to surface tension, $F = 2\sigma A/R$, and spans two orders of magnitude in our experiments. Using the conti-

nuity equation for mass balance along θ, that is Equation (3.4), we obtain

$$\left.\frac{d\delta}{dt}\right|_{\theta=0} = -\frac{1}{C_c}\frac{\delta\sigma}{\eta R}. \tag{2.8}$$

From integration by separation of variables the capillary film drainage time is obtained as

$$t_c = C_c \ln\left(\frac{\delta_0}{\delta_f}\right) \underbrace{\frac{\eta R}{\sigma}}_{\tau_c}, \tag{2.9}$$

where $\tau_c = \eta R/\sigma$ is the characteristic capillary time scale and C_c is an empirical constant.

2.3 Experiments

2.3.1 Overview

I performed experiments in which a bubble of laboratory air was injected at the bottom of a layer of polydimethylsiloxane melt (PDMS a.k.a. silicone oil) and rose to the free surface. In our experiments the width of the experimental box was always at least five times larger than the bubble diameter to avoid any boundary effects. During the experiments, bubble motion underwent two stages. The first stage was the buoyant ascent of the bubble toward the interface and the second was the drainage of the interfacial film above the stationary bubble (*Pigeonneau and Sellier*, 2011). Once the bubble approached the surface, its rise velocity rapidly decreased, forming a protruding hemispherical cap of radius, $R_{\text{cap}} \sim R = (3V/4\pi)^{1/3}$, where V is the volume of the bubble. Subsequently during the second stage, the liquid film that formed the cap thinned from an initial thickness, δ_0, to a thickness, δ_f, at which the bubble spontaneously ruptured (Figures 2.4 and 2.5). The whole process was captured at up to 80 frames per second using a CCD (charge-coupled

device) camera connected to a Zeiss SteREO® microscope (Figures 2.3). The captured images were analyzed to measure bubble dimensions, as well as the time elapsed during stage two, that is between when the bubble rise velocity became negligible and when the bubble spontaneously ruptured (Figure 2.4). This duration is herein defined as drainage time, t_d, and corresponds to a change of film thickness from $\delta_0 \sim 100\,\mu$m to $\delta_f \sim 100$ nm, or $\ln(\delta_0/\delta_f) \approx 7$.

2.3.2 Dynamic Similarity

Dynamic experiments on silicate melts are complicated, due in part to the requirement for high temperatures. To overcome this and other difficulties, analogue materials are commonly used in the study of magmatic processes (*Mader et al.*, 2004). However, for any laboratory experiment to provide useful constraints on the natural system, careful consideration must be given to appropriate scaling of laboratory conditions with respect to the natural processes in question.

Two fluid-dynamical processes are considered to be dynamically similar, if the ratios of all forces acting on corresponding fluid volumes and surfaces in the two systems are the same (*Kline*, 1986). This can be achieved rigorously through dimensional analysis, which permits the reduction of a large number of parameters to a small number of dimensionless numbers (e.g., *Bolster et al.*, 2011). In the cases under consideration, the driving forces for film drainage of bare viscous bubbles are gravitational and surface tension forces, whereas the resisting force is due to viscosity (*Debrégeas et al.*, 1998). I will show subsequently why my laboratory experiments are dynamically similar to gravitationally dominated, as well as surface tension dominated interbubble film drainage in magmas.

Reynolds Number

Inertial forces during film drainage of stagnant bubbles, that is in the absence of an external flow, can be neglected if the Reynolds number, $\mathrm{Re} = \rho U L/\eta \ll 1$. Here Re represents the film Reynolds number, which is the ratio of inertial to viscous forces associated with the flow at the scale of the liquid film, where U is the characteristic velocity, and L is the characteristic length scale. For film drainage surrounding a stationary bubble, $L \sim \delta$ and $U \sim u$.

I find that for all of our experiments $\mathrm{Re} \ll 1$, implying that our results are applicable to film drainage in cases where the forces that resist fluid motion are dominated by the viscous force. It can be verified that in silicate melts, ranging from mafic to silicic in composition, gravitational or capillary drainage of melt films under most any realistic scenario will be at $\mathrm{Re} \ll 1$ (e.g *Toramaru*, 1988; *Proussevitch et al.*, 1993a; *Manga and Stone*, 1994).

Ohnesorge Number

The Ohnesorge number, $\mathrm{Oh} = \eta/\sqrt{2\rho\sigma \mathrm{R}}$, represents the ratio of viscous to inertial and capillary forces (e.g., *Ohnesorge*, 1936; *Kočárková et al.*, 2013). For all of our experiments $\mathrm{Oh} \gg 1$, indicating that viscous forces dominate film drainage. Consistent with previous work (e.g., *Kočárková et al.*, 2013, and references therein), we find no dependence of our results on the Ohnesorge number.

Bond Number

The transition between capillary and gravitational film drainage occurs at $R \approx \lambda$. At this transition $t_c = t_g$, so that from Equations (2.6) and (2.9)

$$\frac{C_g}{C_c} = \frac{\Delta\rho g R^2}{\sigma}. \tag{2.10}$$

The term on the right-hand side of Equation (2.10) is conventionally defined as the Bond number (e.g., *Stone*, 1994),

$$\mathrm{Bo} = \frac{\Delta\rho g R^2}{\sigma}. \tag{2.11}$$

At Bo$\gg 1$, it is expected that gravitational forces dominate film drainage, whereas for Bo$\ll 1$ surface tension forces are expected to be dominant (e.g., *Proussevitch et al.*, 1993a; *Stone*, 1994; *Pigeonneau and Sellier*, 2011). As discussed in detail in Section 3.6, my experimental results show that the transition from capillary to gravitation film drainage occurs at $\mathrm{Bo_t} = C_c/C_g = 0.25$, which corresponds to $R = \lambda/2$. Accordingly, bubble shapes change from near spherical at $\mathrm{Bo} < 0.25$ to hemispherical at $\mathrm{Bo} > 0.25$ (e.g., *Pigeonneau and Sellier*, 2011, Figure 2.6). By varying bubble radii, our experiments spanned the full range of dynamical behavior, from $\mathrm{Bo} \ll 1$ to $\mathrm{Bo} \gg 1$ (Table 1). This allows us to obtain a self-consistent scaling for film drainage for both capillary-dominated and gravity-dominated film drainage.

2.3.3 Geometric Similarity

The coalescence of bubbles suspended in viscous liquids, if not caused by deformation due to bulk flow of the suspension, is the consequence of the thinning of inter-bubble liquid films. It can be caused by either bubble growth, gravitational forces, capillary forces or some combination thereof. Here we discuss why

and how our experiments with single bubbles can provide constraints on inter-bubble film drainage, by gravitational or capillary forces, in liquids containing many closely spaced bubbles, as in vesicular magmas.

The geometric constraints of packing a large volume fraction of bubbles into a given volume of melt, require some degree of bubble deformation, relative to an ideal spherical shape (e.g., *Princen et al.*, 1980). Because the Laplace pressure is greater for smaller bubbles than for larger ones, the latter deform more readily than smaller bubbles as they impinge upon one another. The resultant arrangement is often one where smaller bubbles protrude into larger ones. The resultant inter-bubble films are not flat or of uniform thickness, but of concave/convex shape and thicken toward plateau borders (e.g., Figure 2.1c-e; *Proussevitch et al.*, 1993a; *Gaonac'h et al.*, 1996; *Klug and Cashman*, 1996; *Polacci et al.*, 2001; *Klug et al.*, 2002; *Rust and Manga*, 2002; *Rust and Cashman*, 2004; *Giachetti et al.*, 2010; *Shea et al.*, 2010; *Castro et al.*, 2012).

Regardless of the detailed geometry, film drainage is a consequence of liquid flow within the film, caused by a gradient in liquid pressure toward the plateau borders (e.g., *Proussevitch et al.*, 1993a). In the absence of externally applied deformation, for example due to magma flow, and neglecting bubble growth, this pressure gradient will be a consequence of capillary and gravitational forces. If the dominant force is due to gravity (Bo> 0.25), and irrespective of the precise orientation of the inter-bubble film relative to the center of gravity, there will be an average pressure gradient of $\Delta\rho g$ within the suspension. This pressure gradient causes downward flow within the plateau borders and flow toward the plateau borders within the inter-bubble films (*Proussevitch et al.*, 1993a).

If, on the other hand, the dominant force is due to surface tension (Bo< 0.25),

then the dominant pressure gradients within the inter-bubble film arise because of changes in the radius of curvature of the film's bounding surface. Surface tension requires a pressure jump across the liquid-gas interface, equal to the value of surface tension divided by the local radius of curvature, $2\sigma/R_c$. Because the gas pressure inside the bubble is essentially uniform, changes in capillary pressure along the liquid-gas interface require lateral pressure gradients within the film itself. Typically, the radius of curvature is smallest in the vicinity of plateau borders, as illustrated in Figure 2.1b-e and also in a wide range of publications focused on vesicles in pyroclasts (e.g., *Klug and Cashman*, 1994; *Klug et al.*, 2002; *Formenti and Druitt*, 2003; *Gurioli et al.*, 2005; *Adams et al.*, 2006a; *Degruyter et al.*, 2010; *Giachetti et al.*, 2010; *Houghton et al.*, 1998; *Baker et al.*, 2012). Therefore, the liquid pressure within the inter-bubble film is smallest near the plateau borders, resulting in capillary flow from the inter-bubble films toward the plateau borders.

Although my experiments comprise a single bubble at the surface of a larger volume of liquid, the liquid film that surrounds my bubble is subjected to the same average gravitational pressure gradient $\Delta\rho g$ as the liquid comprising an inter-bubble film that is located somewhere within a bubbly suspension. Similarly, capillary stresses, in both my experiments and bubble suspensions, scale as the ratio of surface tension to bubble radius, σ/R. Figure 2.1c-f shows that in both magmas and my experiments there is a change in the radius of curvature that results in lateral pressure gradients within the film. Although, in detail there may be small geometric differences between my experiments and bubbles in magma, which for the same Bond number may result in small differences between film drainage times. However, because the overall force balance remains unaffected, my experiments provide to first order a viable analog to inter-bubble film drainage

in vesicular magmas, assuming that external deformation or bubble growth are negligible.

2.4 Results

2.4.1 Film Drainage in PDMS

The drainage times, t_d, of the liquid film surrounding air bubbles in PDMS fluid are shown as a function of R in Figure 2.7a. For a given viscosity the value of t_d increases with R until there is a transition in the dynamics of film drainage and t_d decreases with R. This inflection in the trend of t_d vs. R represents the transition between capillary and gravitational film drainage, at $R = \lambda/2 = 0.75$ mm and $\mathrm{Bo} = 0.25$.

A graph of the dimensionless drainage time t_d/t_g vs. Bo is shown in Figure 2.7b. It demonstrates that the drainage time for all experiments with $\mathrm{Bo} \geq 0.25$ can be predicted by Equation (2.6), with $t_d/t_g \approx 1$ for $C_g = 5$. We also show that the values of t_d/t_g determined from the published results of *Debrégeas et al.* (1998) and *Kočárková* (open circles) overlap with our results and do not show a dependence of C_g on Bond number, which is consistent with previous results (*Kočárková et al.*, 2013).

Because my experiments span two orders of magnitude on either side of $\mathrm{Bo} = 0.25$, I am also able to obtain an empirical relation for the capillary drainage time of bare viscous bubbles. I find that for $\mathrm{Bo} < 0.25$ a value of $C_c = 20$ in Equation (2.9) provides a good estimate of capillary drainage time, so that $t_c/t_d \approx 1$ (Figure 2.7c).

It should be noted that Equation (2.1) does not provide an adequate fit to most

of my experimental results. This is demonstrated in Figure 2.8, which compares measured to predicted values of drainage time. Whereas, Equations (2.6) and (2.9) provide a good match to observed values, Equation (2.1) with $n = 2$, as frequently used for film drainage in magmas (e.g. *Cashman et al.*, 1994; *Klug and Cashman*, 1996; *Mangan and Cashman*, 1996; *Cruz and Chouet*, 1997; *Herd and Pinkerton*, 1997; *Navon and Lyakhovsky*, 1998; *Castro et al.*, 2012), overestimates drainage times by up to 8 or 9 orders of magnitude. Even for very small values of the poorly constrained parameter n, only part of the full data set can be matched.

2.4.2 Film Drainage in Silicate Melts

Observed and Predicted Drainage Times

Figure 2.8 demonstrates that our scaling relations obtained from film drainage in PDMS also predict film drainage in silicate melts with reasonable accuracy. For silicate melts, *Kočárková et al.* (2013) suggest a modest dependence of C_g on Bond number near the transition to capillary drainage, with the reason for such a dependence remaining unresolved. I find that a Bond number dependent C_g, as suggested by *Kočárková et al.* (2013), does not improve the fit compared to $C_g = 5$. Although no empirical values of t_c currently exist for silicate melts, the fact that gravitational film drainage in silicate melts is consistent with "bare" viscous films suggests that film drainage times in silicate melts at small Bond numbers can be assessed using Equation (2.9).

Surface Tension

Surface tension in the PDMS experiments is almost constant and differs from the silicate melt experiments of *Kočárková* by only a factor of 1.5 (Table 1). It is therefore

important to ascertain that our results have dynamic similarity to natural silicate melts, where the variability in surface tension may only be approximately one order of magnitude (e.g., *Walker and Mullins*, 1981; *Bagdassarov et al.*, 2000; *Mangan and Sisson*, 2005; *Gardner and Ketcham*, 2011; *Gardner*, 2012; *Kočárková*), with surface tension in our experimental liquids falling at the lower end of this range. Surface tension affects the dynamics of film drainage through the aforementioned force balances (Equation 2.10, Section 2.3.2). In my experiments, surface tension forces vary by orders of magnitude, from 10^{-5} N to 10^{-2} N, exceeding the range in surface tension forces achievable by reasonable variations in surface tension alone, for either analog fluids or silicate melts. Consequently, my experiments span a wide range of dynamic behavior with the ratio of gravitational to capillary forces ranging from Bo $\ll 1$ to Bo $\gg 1$ (Figure 2.7).

Viscosity

Because the viscosity of natural silicate melts can exceed the viscosities of PDMS fluids, the extrapolation of my results to magmatic systems requires dynamic similarity. The liquid viscosity in my experiments ranged from 10 to 10^3 Pa s, within the range of mafic to intermediate magmas (e.g. *Giordano et al.*, 2008; *Hui and Zhang*, 2007). Silicic melts, especially at low water content and low temperature can have viscosities that are substantially larger (e.g. *Hui and Zhang*, 2007), resulting in proportionally smaller velocities (Eq. 2.3 and 2.7) and hence longer drainage times. The film Reynolds number $\ll 1$ for even the least viscous magmas, implying that the force balance is dominated by viscous stresses in both, PDMS experiments and magmas across the full spectrum of naturally occurring compositions, temperatures and water contents. As already discussed in Section 2.3.2, a dependence on

the Ohnesorge number is also not expected. Consequently, my empirical results should be dynamically similar to gravitational and capillary film drainage in magmas ranging from basalt to water-poor rhyolite, in the absence of crystals or other stabilizing impurities, as well as bubble growth or shear deformation.

Interface Mobility

The flow during the drainage of inter-bubble films depends strongly on the nature of the interfaces between the liquid film and the surrounding gas phase. In many applications it is desirable to inhibit or slow the drainage of inter-bubble films, thereby creating a more stable suspension or foam. This is usually achieved by adding surfactants, which, among other things, limit the mobility of the film interfaces. Consequently, liquid flow within the film is similar to flow in a vary narrow gap, bounded by two rigid walls. The flow velocity at each interface approaches zero, making the interface immobile, that is a no-slip boundary (Figure 2.2a). In this case Equation (2.1) should be used to estimate the film drainage time, as it is derived using no-slip boundary conditions (*Charles and Mason*, 1960; *Hartland*, 1970; *Ivanov and Traykov*, 1976). If, on the other hand, there are no impurities at the film interface, the flow velocity is the same at the interface as in the interior (Figure 2.2b). The interfaces of such a "bare" film are therefore fully mobile. Drainage times of liquid films with such free-slip boundaries are given by Equations (2.6) and (2.9) (*Debrégeas et al.*, 1998; *van der Schaaf and Beerkens*, 2006).

Figure 2.8 demonstrates that in the absence of crystals or other impurities film drainage times in silicate melts are consistent with fully mobile interfaces. In the absence of crystals or other impurities that may stabilize inter-bubble films, Equations (2.6) and (2.9) should be used to predict film drainage times in silicate melts,

because calculations based on Equation (2.1) will invariably result in vast overpredictions of drainage times.

2.4.3 Measurement Errors

Drainage Time

For all experiments, the standard deviation in measured bubble radii, R, is less than 1%. The resultant error bars for R and Bo are smaller than the size of symbols used to present the experimental data (Figures 2.7 and 2.8). The experiments covered a range of t_d from approximately 1 s to 5000 s. Figure 2.4 illustrates the method by which t_d was measured from the time-lapse bubble images. From repeat measurements of t_d on individual samples, we estimated the standard deviation of t_d measurements scaled as $0.25\, t_d^{2/3}$, which is also smaller than the size of the data symbols.

Film Thickness

Some degree of uncertainty is also associated with the initial and final film thickness, δ_0 and δ_f, respectively. They affect the predicted drainage time (Eqs. 2.6 and 2.9) through the value of $\ln(\delta_0/\delta_f)$. I measured initial film thickness (on the order of hundred's of micrometers) using high resolution digital images of the bubbles and surrounding films that allowed us to measure δ_0 with an accuracy within 5%, with values ranging from $\sim 10^{-5}$ m to $\sim 10^{-4}$ m. These values are not dissimilar to the maximum thickness of inter-bubble films observed in some natural volcanic samples (e.g. *Gaonac'h et al.*, 1996; *Klug and Cashman*, 1996; *Navon and Lyakhovsky*, 1998; *Formenti and Druitt*, 2003; *Burgisser and Gardner*, 2005; *Polacci et al.*, 2006; *Bai et al.*, 2008; *Giachetti et al.*, 2010; *Shea et al.*, 2010; *Giachetti et al.*, 2011).

The critical film thickness prior to the time of rupture was determined from the light reflectance of the film across a spectrum of wavelengths, using instrumentation provided by Filmetrics Incorporated. The method uses an iterative procedure to constrain film thickness and optical parameters from the spectral reflectance measurements. The spot size of these measurements is 200 μm, resulting in a spatially averaged film thickness across the measurement area. The measured values of δ_f are typically of the order of 10^{-7} m (Figure 2.9). This is consistent with theoretical predictions (e.g., *Sheludko*, 1966; *Coons et al.*, 2003) and also observations of minimum film thicknesses in natural silicate melts (Figure 2.9; *Klug and Cashman*, 1996; *Debrégeas et al.*, 1998; *Navon and Lyakhovsky*, 1998; *Burgisser and Gardner*, 2005; *Castro et al.*, 2012; *Kočárková*). From repeat measurements, the error in δ_f is estimated to be within few percent of the measured value. In contrast to films with immobile interfaces where drainage time scales as δ_f^{-2} (Equation (2.1)), our predicted drainage times depend on $\ln(\delta_0/\delta_f)$. Consequently, the uncertainty in drainage time predictions due to measurement errors in δ_0 and δ_f is less than a factor of approximately 2 and does not significantly bias results.

2.5 Implications for Magmatic Systems

Bubble coalescence in magmatic systems often involves ascent-driven magma decompression and shear deformation (e.g. *Sparks*, 1978; *Toramaru*, 1988; *Proussevitch et al.*, 1993a; *Cashman et al.*, 1994; *Mader et al.*, 1994; *Klug and Cashman*, 1996; *Larsen et al.*, 2004; *Burgisser and Gardner*, 2005; *Okumura et al.*, 2006; *Moitra et al.*, 2013). To assess the conditions under which these processes significantly increase the rates of bubble coalescence requires constraints on the time scales of inter-bubble film drainage in the absence of bubble growth or external deformation. In other words,

capillary and gravitational film drainage give a lower bound on coalescence rates.

2.5.1 Predicted Film Drainage Time in Silicate Melts

Film drainage rates depend on bubble size, as well as material properties, such as viscosity and surface tension. The typical vesicle size ranges between 10^{-6} m and 10^{-2} m for silicic pumices (e.g. *Toramaru*, 1990; *Klug and Cashman*, 1994; *Gaonac'h et al.*, 1996; *Blower et al.*, 2003; *Klug et al.*, 2002; *Rust and Cashman*, 2004; *Gaonac'h et al.*, 2005; *Giachetti et al.*, 2010; *Shea et al.*, 2010) and even larger in basaltic scoria (e.g. *Mangan et al.*, 1993; *Mangan and Cashman*, 1996; *Vergniolle*, 1986; *Lautze and Houghton*, 2007; *Polacci et al.*, 2008, 2009). Surface tension for natural silicate melts ranges within an order of magnitude, from 0.03 to 0.3 N m^{-1} (e.g., *Epel'baum et al.*, 1973; *Murase and McBirney*, 1973; *Khitarov et al.*, 1979; *Walker and Mullins*, 1981; *Taniguchi*, 1988; *Bagdassarov et al.*, 2000; *Mangan and Sisson*, 2005; *Gardner and Ketcham*, 2011; *Gardner*, 2012). In contrast, melt viscosity can vary by many orders of magnitude (e.g., *Hess and Dingwell*, 1996; *Hui and Zhang*, 2007).

For the range of feasible parameters discussed above, I estimate the drainage time in both capillary and gravitational regimes using Equations (2.6) and (2.9). The results are shown in Figure 2.10 and indicate that film drainage times for adjacent bubbles in basaltic melts, even in the absence of bubble growth or external deformation, will be 10s of seconds or less. In intermediate and silicic melts, film drainage times are considerably larger, with up to $\sim 10^9$ s in dry rhyolitic melts.

2.5.2 Post-Fragmentation Coalescence in Pyroclasts

Bubble coalescence may result in magma permeability with ensuing implications for open-system magma degassing and magma fragmentation (e.g., *Westrich and*

Eichelberger, 1994a; *Klug and Cashman*, 1996; *Saar and Manga*, 1999; **?**; *Burgisser and Gardner*, 2005; *Okumura et al.*, 2006; *Wright et al.*, 2006; *Mueller et al.*, 2008; *Namiki and Manga*, 2008; *Okumura et al.*, 2008; *Wright et al.*, 2009; *Rust and Cashman*, 2011; *Castro et al.*, 2012; *Namiki*, 2012). Because magma ascent conditions are inferred from measured textural characteristics and permeabilities in pyroclasts, it is important to assess the extent of bubble coalescence after magma fragmentation, and thus, the likelihood that measured values are significantly different from conditions prior to fragmentation.

During the time interval between magma fragmentation and quenching, when shear deformation may no longer be the dominant processes and when characteristic length scales for permeable gas flow are of the order of centimeters, bubble growth may be negligible, because permeable gas loss may efficiently dissipating gas pressure (*Rust and Cashman*, 2011; *Gonnermann and Houghton*, 2012). If this is the case, post-fragmentation bubble coalescence rates can be estimated from estimates for interbubble film drainage rates. Thus, if post-fragmentation coalescence can be shown to be negligible, then pyroclast textural characteristics, such vesicle size distributions, as well as permeabilities likely provide a reliable record of pre-fragmentation conditions.

Cooling times of pyroclasts have been estimated to be of the order of 10-100 s (e.g. *Thomas and Sparks*, 1992; *Hort and Gardner*, 1998). Figure 2.10 indicates that film drainage times may only be of similar or shorter duration as cooling times in relatively water-rich intermediate melts. Consequently, it is unlikely that there is sufficient interbubble film drainage in pyroclasts from explosive intermediate to silicic magmas to significantly change pyroclast vesicle size distributions and permeability after magma fragmentation.

2.6 Conclusions

I presented laboratory experiments wherein we measured the lifetime of stationary air bubbles suspended beneath the free surface of surfactant-free PDMS liquids. To ensure dynamic similarity to magmatic systems, all experiments were at small Reynolds numbers ($\mathrm{Re} \ll 1$) and cover a wide range of Bond number, $10^{-3} \leq \mathrm{Bo} \leq 10^{2}$, with the transition between capillary and gravitational drainage corresponding to a Bond number of 0.25. My results are consistent with similar experiments in PDMS and in silicate melts. They provide predictions of film drainage times that can be applied to bubbles in magma, if shear deformation and bubble growth are negligible, and if interbubble films are not stabilized, for example by the presence of abundant microlites. Overall, my results indicate that textural characteristics and permeabilities of pyroclasts from intermediate to silicic magmas may preserve pre-fragmentation conditions. Furthermore, film drainage times in magmas are likely orders of magnitude shorter than previous estimates that are based on formulations for liquid films with immobile interfaces.

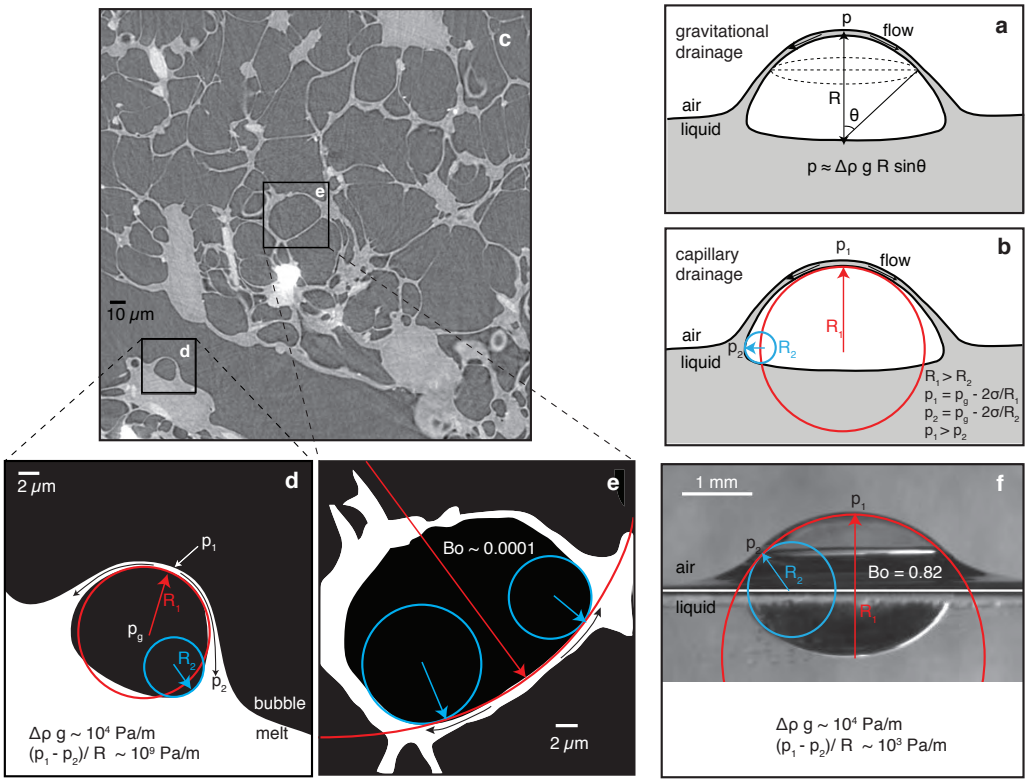

Figure 2.1 : Film drainage in vesicular magma and laboratory experiments. (a,b) Schematic diagram of a bubble and surrounding liquid, illustrating gravitational (a) and capillary (b) film drainage. (c) A CT-scan image of Soufrière Hills pumice sample PV3-800x800-504 showing vesicular texture with thin inter-bubble films (courtesy of T. Giachetti and discussed in *Giachetti et al.*, 2011). The vesicles presumably preserve the shapes, sizes and distribution of bubbles within the pyroclast prior to quenching. (d,e) Individual vesicles at higher magnification and with annotation to highlight the change in curvature along the melt film. Also indicated are estimates of the ensuing capillary pressure gradient that would have driven film drainage, $(p_2 - p_1)/R \sim 10^9$ Pa m^{-1}, for a constant pressure p_g inside the bubble and bubble radius, R. The pressure gradient due to gravity is $\Delta\rho g \sim 10^4$ Pa m^{-1}, where $\Delta\rho$ denotes the difference in density between liquid and bubble and g is the acceleration due to gravity. (f) Example of a bubble from one of our film drainage experiments, showing the change in curvature along the melt film surrounding the bubble, as well as estimated difference in pressure due to surface tension at $\sim 10^3$ Pa m^{-1}. The pressure gradient due to gravity is $\Delta\rho g \sim 10^4$ Pa m^{-1}. Regardless of precise geometry, that is multiple bubbles in magma at some orientation or a single bubble in our experiment, gravity and changes in the radius of curvature result in pressure gradients within the film that drive film drainage. Depending on bubble size, the relative magnitude of these driving forces changes, as quantified by the Bond number.

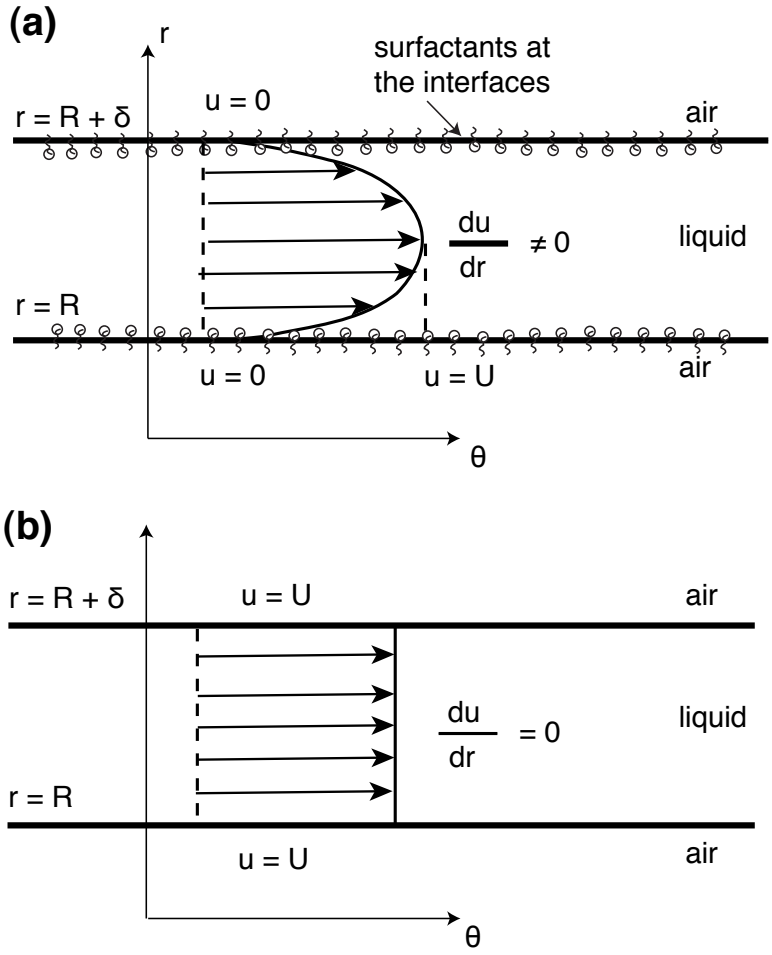

Figure 2.2 : Schematic diagrams illustrating the mobility of gas-liquid interfaces. (a) The velocity profile for flow in a film with immobile interfaces. (b) The velocity profile for fully mobile interfaces.

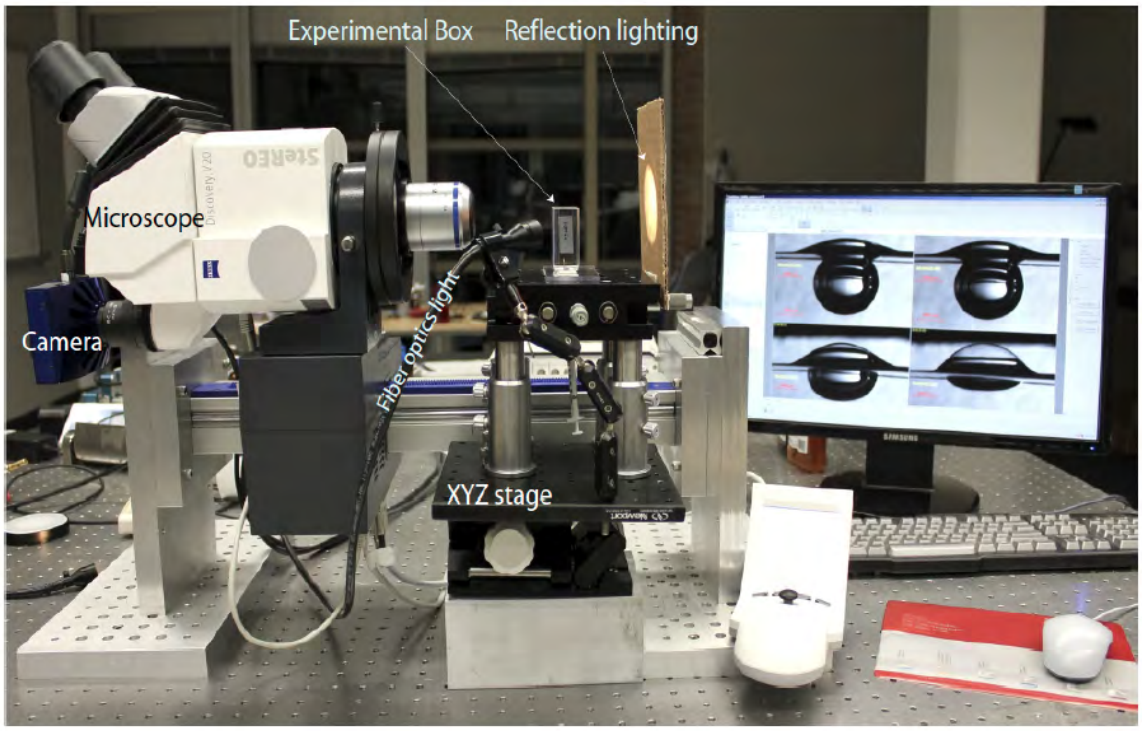

Figure 2.3 : An image of experimental set-up. An experimental box made of glass was filled with silicone oil. I injected a single bubble from the bottom of the box through a septum and let the bubble rise to the surface while the high- speed camera captured a whole sequence from when the bubble rose to the surface, the liquid drained to the time of film rupture. The images were recorded digitally using AxioVision software for Zeiss SteREO® microscope.

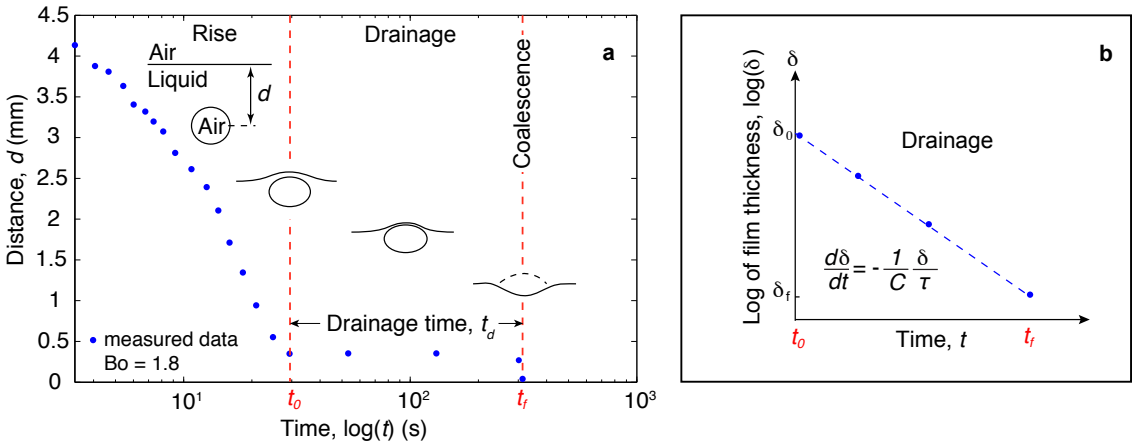

Figure 2.4 : (a) A typical experiment, showing measured position of the bubble relative to the free surface, d. As the bubble approaches the free surface its velocity decreases. Once the bubble rise velocity approaches zero, film drainage begins and the drainage time, t_d, is defined as the time thereafter until the bubble ruptures. (b) Schematic diagram of film thinning, with the constant film thinning rate $d\delta/dt$ in semi-log scale, indicating that film thickness decays exponentially with time.

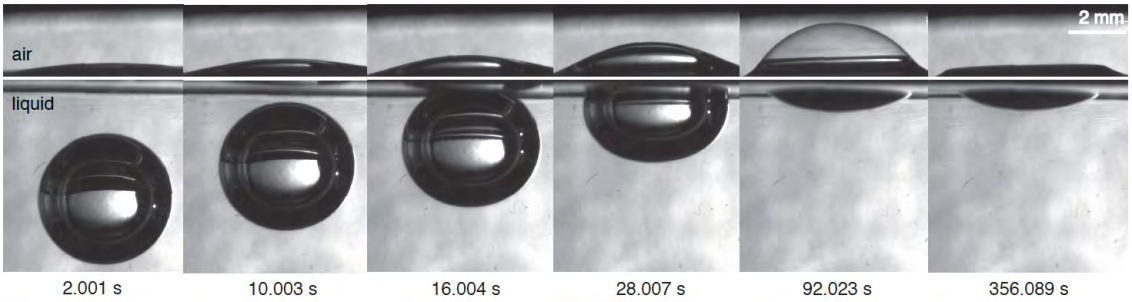

Figure 2.5 : Experimental images of one experiment starting with the bubble approaching the free interface (left) through film drainage and finally coalescence, that is film rupture (right).

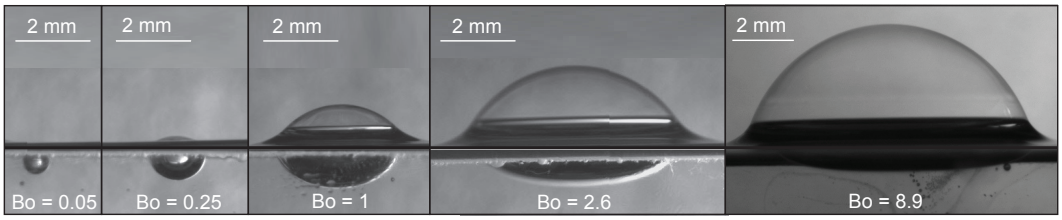

Figure 2.6 : Images showing bubble shapes for different Bond numbers, Bo. At $\mathrm{Bo} < 0.25$ surface tension forces dominate over gravitational forces, surface area is minimized and the bubble has a spherical shape. At $\mathrm{Bo} > 0.25$, gravitational forces dominate and the bubble is no longer spherical in shape. Note that in some images the edges of the flow cell make the liquid interface appear 'dirty', which is not the case.

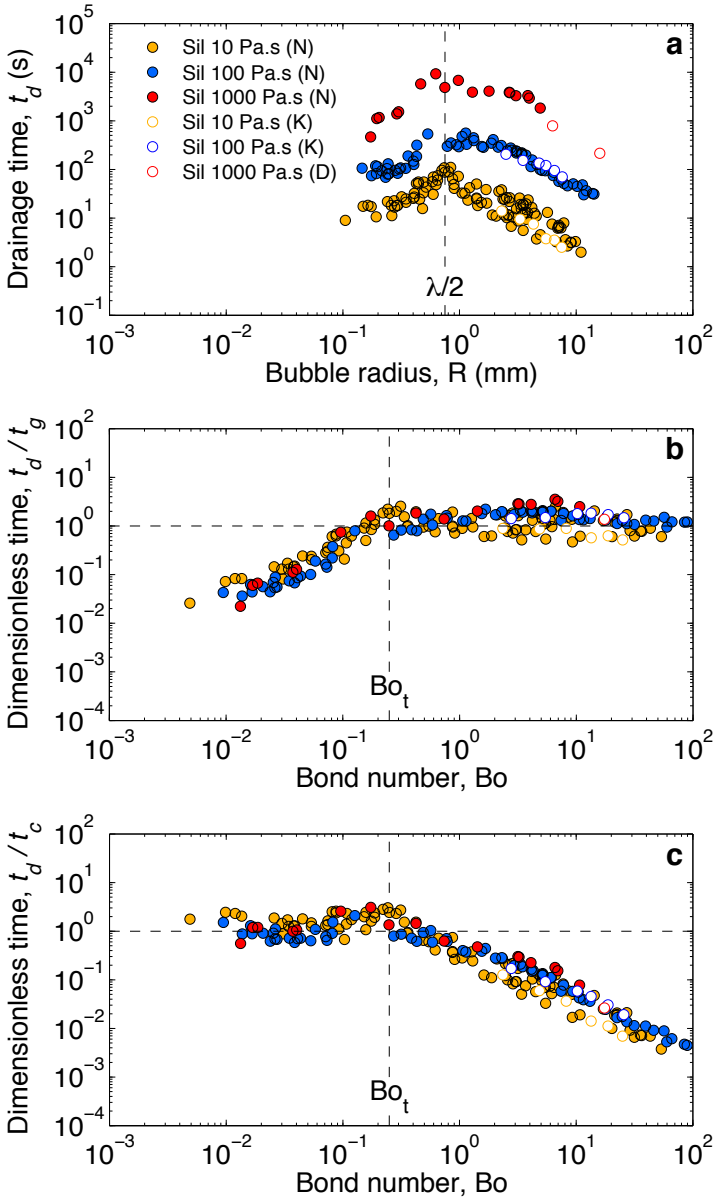

Figure 2.7 : (a) Measured film drainage time, t_d, vs. bubble radius, R. Filled circles are experiments from this study using PDMS fluids. Open circles are PDMS experiments by *Debrégeas et al.* (1998) and *Kočárková*. The transition from capillary drainage to gravitational film drainage occurs at half of the capillary length, $\lambda/2 \approx 0.75$ mm. (b) The same experiments with t_d normalized to the gravitational drainage time, t_g. At $\mathrm{Bo} > 0.25$ a value of $t_d/t_g \sim 1$ indicates that Equation (2.6) provides a good estimate for $t_{d,\,\mathrm{Bo}>0.25}$. (c) The same experiments with drainage time, t_d, normalized to the capillary drainage time, t_c. At $\mathrm{Bo} < 0.25$ the experimental drainage time also has a value of $t_d/t_c \sim 1$, indicating that Equation (2.9) provides a good estimate for $t_{d,\,\mathrm{Bo}<0.25}$.

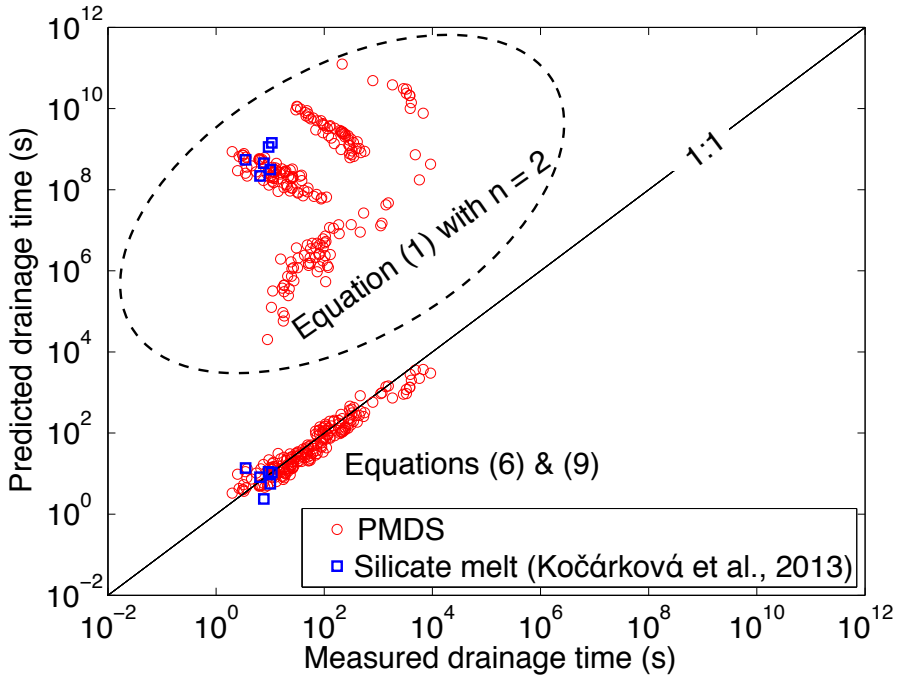

Figure 2.8 : Observed vs. predicted film drainage times. Red circles are PDMS experimental data and blue squares are silicate melt data . Experiments plotted within the dashed ellipse have predicted drainage time calculated using Equation (2.1) with $n = 2$ and overpredict drainage times by up to 9 orders of magnitude. Experiments plotted along the 1:1 line have predicted drainage times calculated using Equations (2.6) and (2.9). Drainage times for silicate melt experiments of *Kočárková et al.* (2013) are shown as blue squares, indicating that Equation (2.6) also predicts film drainage in silicate melt reasonably well. The silicate melts had compositions of 72.3% SiO_2, 13.5% Na_2O, 9.6% CaO, 4% MgO and 0.6% Al_2O_3, as well as 61.8% SiO_2, 12.6% Na_2O, 0.5% CaO, 9.4% K_2O, 7.6% MgO and 8.1% Al_2O_3. Corresponding viscosities were 64 and 154 Pa.s, densities 2344 and 2318 kg m^{-3}, and surface tension 0.322 and 0.303 N m^{-1}, respectively.

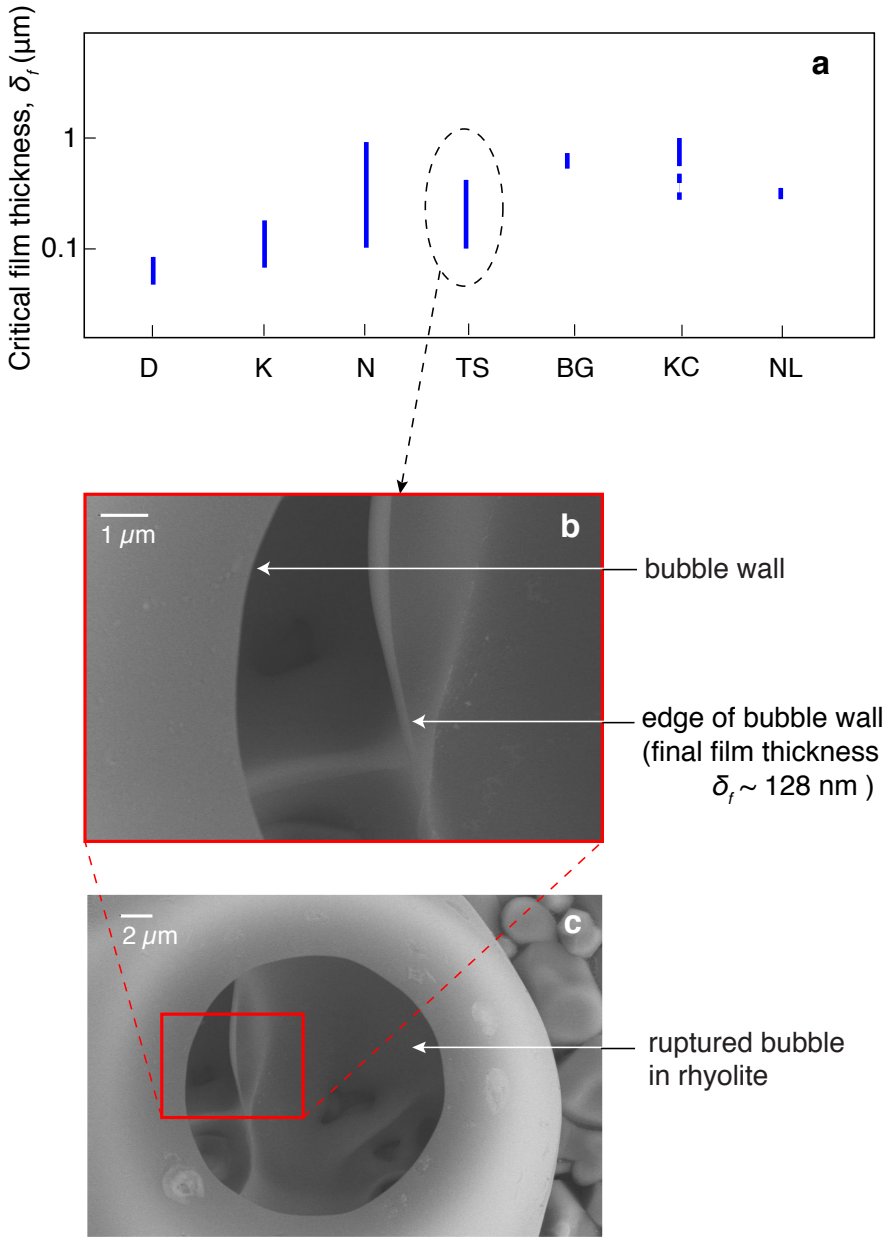

Figure 2.9 : (a) Compilation of critical film thickness measurements. The new PDMS experiments presented herein are labeled as 'N', those by *Debrégeas et al.* (1998) as 'D', and PDMS and silicate melt experiments by *Kočárková et al.* (2013) combined as 'K'. Film thickness estimates from SEM images of natural samples are labeled as 'KC' (*Klug and Cashman*, 1996), 'NL' (*Navon and Lyakhovsky*, 1998), and 'BG' (*Burgisser and Gardner*, 2005). (b) High resolution SEM image of ruptured bubble wall in natural rhyolite produced in thermal spray vesiculation experiments (*Qu et al.*, 2007; *Qu and Gouldstone*, 2008), showing that ruptured bubble walls are approximately 0.1 μm in thickness (labeled as 'TS'). (c) SEM image at higher resolution, showing the ruptured bubble.

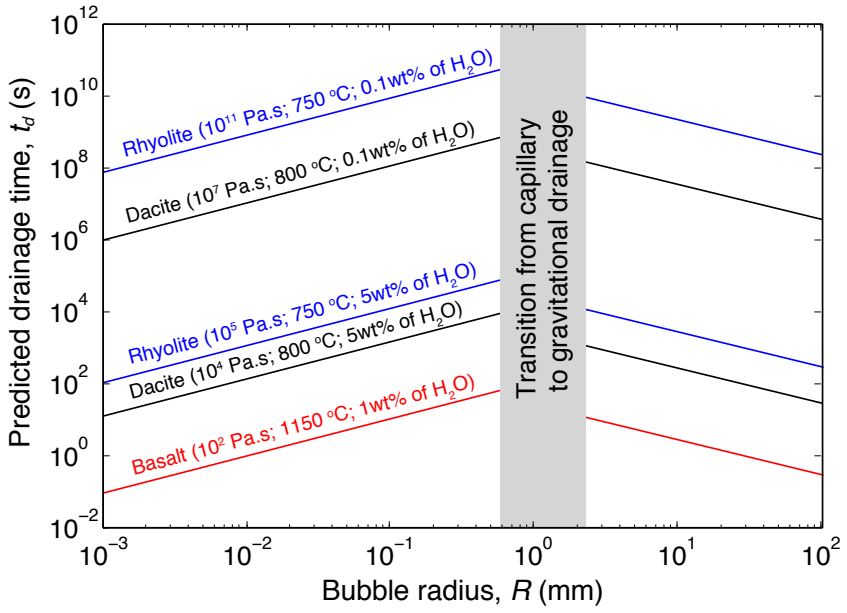

Figure 2.10 : Illustrative predictions of film drainage time (in the absence of bubble growth or shear deformation) in basalt (red), dacite (black) and rhyolite (blue) melts using viscosities from *Hui and Zhang* (2007) at the indicated temperatures and water contents. At small radii, where film drainage is dominated by capillary drainage, predicted drainage times are plotted at a surface tension of $\sigma = 0.1$ N m^{-1}, whereas gravitationally dominated film drainage is independent of surface tension.

Table 2.1 : Experimental parameters.

	Parameter	Symbol	Value	Unit
PDMS[1]	Viscosity	η	10 - 1000	Pa s
	Density	ρ	971 - 977	kg m^{-3}
	Surface tension	σ	21.2 - 21.6	mN m^{-1}
	Initial film thickness[2]	δ_0	10 - 100	μm
	Final film thickness[3]	δ_f	0.1	μm

$Notes.$ [1]Includes my experiments presented herein, as well as some experiments by *Kočárková*. [2]As described in Section 2.4.3, the initial film thickness, δ_0, was measured from the bubble images when the bubble became stagnant (Figure 2.4). [3]The film thickness at the time of rupture, δ_f, was measured as described in Section 2.4.3 and is consistent with the values determined by *Debrégeas et al.* (1998), *Kočárková*.

Chapter 3

Explosive to effusive transition during the largest volcanic eruption of the 20th century (Novarupta 1912, Alaska)

†This Chapter has been edited, reformatted and reprinted from Chinh T. Nguyen, Helge M. Gonnermann, and Bruce F. Houghton (2014), Explosive to effusive transition during the largest volcanic eruption of the 20th century (Novarupta 1912, Alaska). Geology, 42, 703-706, doi: 10.1130/G35593.1, Geological Society of America.

Silicic volcanic eruptions commonly show abrupt shifts between powerful and dangerous (Plinian) explosive episodes and gentle effusion of lava. Whether the onset of magma permeability and ensuing gas loss controls these transitions has been a subject of debate. I measured porosities and permeabilities in samples from the A.D. 1912 eruption of Novarupta volcano, Alaska, and analyzed them within the context of well-constrained eruptive sequence that encompasses sustained explosive and effusive activity. For the explosive samples, I find that the degree of vesicle interconnectivity, measured as the ratio of connected to total porosity, decreases with the phenocryst content and with increasing eruption intensity. Permeabilities of explosive samples show a weak dependence on porosity. Dome samples are not significantly different in permeability, but are of lower porosity, which together with abundant flattened vesicles is consistent with bubble collapse by permeable outgassing. Quantitative analysis indicates that outgassing alone was

insufficient to effect the transition to effusive activity. Rather, the change from explosive to effusive activity was probably a consequence of high versus low magma ascent rates.

3.1 Introduction

The degassing of magma is of critical importance for determining the style and intensity of volcanic eruptions (e.g., *Jaupart and Allegre*, 1991; *Woods and Koyaguchi*, 1994; *Dingwell*, 1996). The exsolution og magmatic volatiles into bubbles provides magma buoyancy and drives the ascent of the magma through the conduit. Exsolution of dissolved water also increases magma viscosity, which resists bubble growth. Consequently, during magma ascent the pressure inside the bubbles decreases more slowly than the pressure outside, resulting in overpressure of the exsolved volatiles and explosive magma fragmentation, once a critical overpressure, ΔP_f, has been reached (*Mueller et al.*, 2008).

An important discovery is that magmatic gases can flow through vesicular magma and escape (*Eichelberger et al.*, 1986), once bubbles coalesce to form persistent interconnected networks. This process, herein referred to as permeable outgassing, may reduce the pressure of magmatic gases and, hence, the potential for sustained explosive fragmentation. The question as to what extent permeable outgassing modulates volcanic eruptions, in particular the transition between sustained explosive and effusive activity, remains a subject of debate (e.g., *Jaupart and Allegre*, 1991; *Woods and Koyaguchi*, 1994; *Dingwell*, 1996; *Melnik and Sparks*, 1999; *Castro and Gardner*, 2008).

3.2 The A.D. 1912 Eruption of Novarupta, Alaska

To adress the above question, I characterized the porosities and permeabilities of samples from a single eruption, the A.D. 1912 eruption of Novarupta in Alaska (e.g., *Fierstein and Hildreth*, 1992; *Hildreth and Fierstein*, 2000, 2012; *Adams et al.*, 2006a,b). From 6 to 8 June 1912, the explosive stage of the Novarupta eruption started with three Plinian episodes, which lasted $\sim$ 60h, albeit with two pauses in eruptive activity. Mass eruption rates for the Plinian Episodes I-III have been estimated at $\sim$ 5, 1.6, and 1.1 x 10^8 kg.s^{-1}, respectively. This sustained explosive activity of Episodes I-III gave way to ephemeral dome growth and Vulcanian activity of Episode IV, and subsequently to stable dome growth in Episode V, producing the current Novarupta dome.

Eruptive products consist of rhyolite and dacite, as well as andesite which played a volumetrically negligible role (Table 3.5). In Episode I, first rhyolite was erupted, followed by rhyolite and dacite erupting simultaneously, together with minor andesite. Episodes II, III and IV were dominantly dacite, and Episode V was again rhyolite. Both rhyolite and dacite consist of rhyolitic melt, and the contrast in bulk chemistry is due to the higher phenocryst content of the dacitic magma (*Coombs and Gardner*, 2001; *Hammer et al.*, 2002), which increases the viscosity of the dacitic magma by about one order of magnitude relative to the rhyolite (*Mader et al.*, 2013).

3.3 Permeable Outgassing

Permeable flow of gases, once coalescing bubbles have formed an interconnected pathway, is thought to occur above a critical porosity, ϕ_c, which can range from

$\sim 30\%$ to $> 70\%$ (*Klug and Cashman*, 1996). Above ϕ_c, permeability is thought to increase with porosity to some power, n, as bubbles continue to nucleate, grow and coalesce. Although theoretical values of n fall near 2 (*Blower*, 2001), in nature they appear to be greater (*Rust and Cashman*, 2011). One hypothesis is that if the rate at which bubbles coalesce is much smaller than the rate at which the magma depcomresses and new bubbles nucleate and grow, ϕ_c and n will increase, because coalescence is kinetically limited (*Takeuchi et al.*, 2009).

3.4 Sample Measurements and Analysis

I measured porosities and permeabilities in representative samples from five episodes of the Novarupta eruption. I excluded any dense samples from Episodes IV and V that showed pervasive fine cracking, because these microcracks have an uncertain origin and would bias permeability measurements. Measured permeabilities are thererfore solely due to interconnected vesicles formed by bubble coalescence.

3.4.1 Porosity Measurements

Samples were cored into cylinders of 1cm diameter and 1-5cm length (see Appendix B). Pycnometry was performed using a Micromeritics AccuPyc II 1340®, which determined the skeletal sample volume, V_{ske} (the sum of the volumes of both solid and isolated pores), by measuring the pressure change of helium within the calibrated volume and using Boyle's law. Then the volume of connected pores was calculated as $V_{con} = V_{sample} - V_{ske}$, where V_{sample} is the volume of cylindrical core of the sample. Powderized samples were also measured using the AccuPyc II 1340® to determine the density of the skeleton (solid plus any isolated vesicles that not somehow connected to the sample surface), which then was used to calculate

the volume of isolated pores, V_{iso}. Finally, connected and total porosity were calculated as $\phi_{con} = V_{con}/V_{sample}$, and $\phi_{total} = (V_{con} + V_{iso})/V_{sample}$. Measured porosity values of all samples are listed in Tables 3.1 and 3.2.

3.4.2 Permeability Measurements

Permeability was measured using Capillary Flow Porometer (Model CFP-1100AXL-AC, Porous Media, Inc.®). Samples were sealed with impermeable epoxy resin and then mounted on plexi-glass plates for permeability measurements (see Appendix B). These samples were then placed in a chamber and completely sealed except the two ends. At the inlet air pressure, P_{in}, varied from 1.1×10^5 Pa up to 6 x 10^5 Pa; whereas the outlet pressure, P_{out}, at the other end was atmospheric pressure. Each sample was measured using 2 - 3 interchangeable flow meters, in order to achieve several orders of magnitude in flow rates at optimal accuracy. For all measurements, the controlled pressure gradient across the sample length was thus between 0 and 5×10^5 Pa m^{-1}, and the measured volumetric flow rate of air, Q, was between 3×10^{-3} and 5×10^{-7} m^3 s^{-1}, with an accuracy $\sim 5 \times 10^{-8}$ m^3 s^{-1} ($\approx 1\%$ of the minimum measured flow rate). After the measurements, samples were sectioned and examined under a transmitted light microscope, as well as a scanning electron microscope for cracks and images. Only samples that showed no cracks of any size were reported.

3.4.3 Permeability Estimation

I estimated permeability using Forchheimer's equation (e.g., *Reynolds*, 1900; *Forchheimer*, 1901; *Rust and Cashman*, 2004) for a compressible gas as follows,

$$\frac{{P_{in}}^2 - {P_{out}}^2}{2PL} = \frac{\mu}{k_1}\frac{Q}{A} + \frac{\rho}{k_2}\left(\frac{Q}{A}\right)^2, \tag{3.1}$$

where P is the pressure at which flow rate is measured, that is $P = P_{out} = 1$ atmosphere. Furthermore, $\mu = 1.86 \times 10^{-5}$ Pa.s is the air viscosity, $\rho = 1.28$ kg m^{-3} its density and A is the cross-sectional area of the sample. k_1 is the Darcian permeability and k_2 is known as the inertial permeability.

Due to the turbulent viscous dissipation flow curves become parabolic (Figure 3.2a), instead of linear, at high values of Q. This turbulent dissipation is accounted for by the k_2 term of Equation 3.1 when fitting the Q vs. $\Delta P = P_{in} - P_{out}$ data (i.e., the flow curves). In order to determine the combination of k_1 and k_2 we calculated the root-mean-square error between measured values of $Q(\Delta P)$ and those predicted by Equation 3.1 for systematically different combinations of k_1 and k_2. In other words, we used a grid search to find the values of k_1 and k_2 that minimize the root-mean-square error, defined as

$$\chi = \frac{1}{N}\left[\sum_1^N \left(1 - \frac{Q_{\text{predicted}}}{Q_{\text{measured}}}\right)^2\right]^{1/2}, \tag{3.2}$$

where N is the number of data points for a given sample. A typical example of such a grid search is shown in Figure 3.2. This result is typical of all our data and illustrates that the flow curves are indeed well-fitted by Equation 3.1. The relationship between k_1 and k_2 for all of our samples is shown in Figure 3.3 and similar to what has been reported elsewhere (*Rust and Cashman*, 2004). Permeability values of all samples are listed in Tables 3.1, 3.2 and 3.3.

3.5 Numerical Modeling

To assess the possible conditions of magma ascent, fragmentation, and permeable outgassing, I performed numerical modeling of integrated magma ascent and bubble growth for Episodes I-III, as well as for hypothetical scenarios at lower discharge rates (see Table 3.5). The models constitute isothermal, one-dimensional conduit flow of the ascending magma, coupled with diffusive bubble growth for both H_2O and CO_2 (*Gonnermann and Houghton*, 2012). Among the other parameters, the model calculates gas pressure within bubbles, which together with ϕ and k_1 (where k_1 is Darcian permeability, see details in Section 3.4) allows for prediction of magma fragmentation.

I performed numerical modeling of magma ascent coupled with diffusive bubble growth for both H_2O and CO_2. The change in ambient pressure with depth is calculated from the momentum and mass balance of magma flow within the conduit. The conduit flow calculations depend on viscosity of the magma, which in turn depends on the dissolved H_2O within the melt and the volume fraction of bubbles, both of which are calculated from diffusive bubble growth. Diffusive bubble growth in turn depends on the change in ambient pressure, which thereby couples diffusive bubble growth with conduit flow.

Modeling was for the sustained explosive Episodes I-III, as well as a case equivalent to Episodes II and III, but at a lower discharge rate, in order to illustrate the effect of lower discharge rate on eruption dynamics. Discharge rates were based on estimates published in *Hildreth and Fierstein* (2012) and details of the model parameters are listed in Tables 3.4 and 3.5.

3.5.1 Conduit Flow Model

The model assumes steady isothermal flow at a constant discharge rate, Q, within a one-dimensional cylindrical conduit of a constant radius, a. The change in ambient pressure, p_m, is calculated from the equation of momentum balance (e.g., *Wilson*, 1980; *Dobran*, 1992; *Mastin*, 2002)

$$\frac{dp_m}{dz} = -\rho g - f_m \frac{\rho u^2}{4a} - \rho u \frac{du}{dz}, \tag{3.3}$$

together with the equation of mass balance,

$$\frac{d(\rho u)}{dz} = 0. \tag{3.4}$$

Here $\rho = \rho_m(1 - \phi)$ is the magma density; ρ_m is the density of the melt; g is gravitational acceleration; $u = dz/dt = Q/(\pi a^2 \rho)$ is the magma ascent velocity; $f_m = 64/Re + f_0$ is the friction factor for pipe flow. $Re = \rho u a/\eta$ is the Reynolds number, and $f_0 = 0.02$ (e.g., *Wilson*, 1980; *Dobran*, 1992; *Mastin*, 2002).

Magma viscosity, η, is calculated using the viscosity formulation for bubble-bearing liquids (*Pal*, 2003), with the liquid viscosity given by the composition-, temperature- and dissolved water- dependent viscosity of the melt phase, using the formulation of *Hui and Zhang* (2007). In addition, the effect of phenocrysts is accounted for using the Krieger-Dougherty equation (e.g., *Mader et al.*, 2013) with a critical packing fraction of 0.65 and an exponent of -2.5 (e.g., *Gonnermann and Manga*, 2007).

3.5.2 Diffusive Bubble Growth Model

As ambient pressure, p_m, decreases the solubility of H_2O and CO_2 decreases, causing them to diffuse into bubbles. In addition, the density of the exsolved H_2O-CO_2

vapor mixture decreases as pressure decreases. Together, diffusion of H_2O and CO_2 into bubbles and decrease in density result in bubble growth, which in turn is resisted by viscosity of the surrounding melt. Therefore, diffusive bubble growth couples the conservation of mass for H_2O and CO_2 with the diffusion of H_2O and CO_2 within the melt and momentum balance for the bubble and surrounding melt.

I used the isothermal formulation first published by *Amon and Denson* (1984) and *Arefmanesh and Advani* (1991) and subsequently applied to bubbles in magma by *Proussevitch et al.* (1993b). The approach follows close to that presented in *Gonnermann and Houghton* (2012).

Assuming that the bubbles exist in a uniform packing geometry, I modeled one idealized representative bubble of spherical shape, which is surrounded by melt shell with the thickness of $S - R$, where S is the outer radius and R is the final bubble radius. The momentum balance is in this case given by *Proussevitch et al.* (e.g., 1993b)

$$\frac{\partial c_i}{\partial t} + v_r \frac{\partial c_i}{\partial r} = \frac{1}{r^2} \frac{\partial c_i}{\partial r} \left(D_i r^2 \frac{\partial c_i}{\partial r} \right), \tag{3.5}$$

where r is bubble radius, c_i is the concentration of volatile species i (either H_2O or CO_2), $v_r = dR/dt$ is the radial growth rate at the melt-vapor interface ($r = R$), and D_i is diffusion coefficient of volatile species i. The boundary conditions are given by $\left(\frac{\partial c_i}{\partial r}\right)_{r=S} = 0$ and $(c_i)_{r=R} = s_i(p_g, x_c)$ (*Gonnermann and Houghton*, 2012). Here s_i is solubility of species i as formulated in *Liu et al.* (2005), p_g is the gas pressure within the bubble, and x_c is the mole fraction of CO_2 of the H_2O-CO_2 vapor mixture within the bubble.

I assume that each bubble grows in a closed system. Therefore, it follows that

mass conservation is given by

$$\frac{d}{dt}(\rho_g R^3) = 4R^2 \rho_m \sum_i q_i, \tag{3.6}$$

where ρ_m is melt density, and ρ_g is the density of the H_2O-CO_2 vapor mixture calculated from an equation of state (*Kerrick and Jacobs*, 1981). q_i is the diffusive mass flux of volatile species i and is calculated fro mthe boundary condition $q_i = D_i\left(\frac{\partial c_i}{\partial r}\right)_{r=R}$.

The momentum balance is given by

$$p_g(t) - p_m(t) = \frac{2\sigma}{R} + 4\eta_e \frac{1}{R}\frac{dR}{dt}, \tag{3.7}$$

where t denotes times, p_g is gas pressure inside the bubble, p_m is the pressure in the surrounding melt, σ is surface tension, η_e is effective viscosity of the melt (*Lensky et al.*, 2001), which depends on the concentration of dissolved H_2O (*Hui and Zhang*, 2007).

3.5.3 Fragmentation and Permeability

The model calculations stop once the difference between pressure of the H_2O-CO_2 vapor mixture inside bubbles and the ambient pressure, $\Delta P = p_g - p_m$, exceeds the fragmentation threshold of *Mueller et al.* (2008),

$$\Delta P > \Delta P_f = (8.21 \times 10^5 MPam^{-1}\sqrt{k_1}1.54MPa)/\phi. \tag{3.8}$$

Here $\phi = R^3/S^3$ is the volume fraction of bubbles and the Darcian permebility, k_1, is calculated from ϕ using the formulation $k_1 = r^2(\phi - \phi_c)^n$ (e.g., *Blower*, 2001; *Rust and Cashman*, 2004, 2011) with values for ϕ_c, critical porosity, and n, power-law coefficient, as shown in Table 3.5 and corresponding to the curves shown in Figure 3.5K.

3.6 Results

3.6.1 Porosity

Sample porosities range approximately between 30% and 60% for Episode V and $60\% - 80\%$ for Episodes I-IV (Figure 3.1). All samples have connected porosity that is lower than total porosity by $\sim 10\% - 20\%$ (i.e., not all vesicles are interconnected). Episode I samples have a distinctly lower ratio of connected to total porosity than all other samples. Given the high eruption rates of Episode I, this may be due to less time for bubble coalescence relative to the other episodes, although Episode I samples also of substantially lower phenocryst content ($1\% - 3\%$) than those from Episodes II - IV ($30\% - 50\%$), which may also affect bubble coalescence (*Takeuchi et al.*, 2009; *Rust and Cashman*, 2011). The trend in connected versus total porosity for the dome samples of Episode V is similar to that for Episodes II - IV, but at distinctly lower total porosities (Figure 3.1). This, together with the flattened vesicle shapes of Episode V samples, is consistent with bubble collapse and loss of porosity during permeable outgassing (*Eichelberger et al.*, 1986; *Westrich and Eichelberger*, 1994b).

3.6.2 Permeability

Permeabilities (Figure 3.4) approximately follow the relation $k_1 = r^2(\phi - \phi_c)^n$ (*Blower*, 2001), where $r = 3 \times 10^{-5}$ m is the approximate median vesicle radius in the Novarupta samples (*Adams et al.*, 2006b). A range in values of ϕ_c and n can match the data, with Episode III and IV samples having on average higher values of k_1 at any given ϕ than Episode I and II samples. Feasible values of ϕ_c and n that fit the data of Episodes I-IV are $\phi_c \geq 0.5$ and $n \geq 3.5$, whereas permeabilities

of Episode V dome samples are not significantly lower, but shifted toward lower values of ϕ and ϕ_c. This is consistent with permeable outgassing (*Eichelberger et al.*, 1986; *Westrich and Eichelberger*, 1994b), but makes it unclear to what extent permeability prior to outgassing may have been higher.

3.6.3 Overpressure, Fragmentation, and Permeable Outgassing

Explosive magma fragmentation is thought to be a consequence of gas overpressure, estimated in (e.g., Equation 3.8; *Mueller et al.*, 2008), and found to range between 1 and 5 MPa. For the erupting magma to have reached ΔP_f, the characteristic viscous time, $\tau_{vis} \sim \eta/\Delta P_f$, and the characteristic permeable time, $\tau_k \sim L^2\mu/k_1\Delta P$, both had to exceed the characteristic decompression time, $\tau_{dec} \sim \Delta P/\dot{P}$. Here η is melt viscosity, $L \sim 100$m is the characteristic path length of permeable gas flow, $\mu \sim 10^{-5}$ Pa.s is the viscosity of the vapor phase (*Rust and Cashman*, 2011), and $\dot{P}$ is the decompression rate. The condition $\tau_{vis} \leq \tau_{dec}$ implies that there is insufficient time for buble growth during decompression, resulting in the build-up of overpressure. At the same time, $\tau_k \leq \tau_{dec}$ indicates that there is insufficient time for permeable outgassing, providing an upper bound, $k \leq L^2\mu/\eta$, at which permeability does not prevent the build-up of overpressure. Because the fall deposits from Episodes I-III lack textural evidence for pervasive shear fragmentation, the shortest pathway for permeable outgassing is radially toward the conduit margins, where flow fracturing may provide enhanced permeability (*Stasiuk et al.*, 1993; *Gonnermann and Manga*, 2003; *Tuffen et al.*, 2003).

At magmatic temperatures (850 °C) and pressures similar to ΔP_f, the water content of the Novarupta rhyolitic melt was ~ 1 wt% (*Liu et al.*, 2005), resulting in a viscosity η of $\sim 10^7$ Pa.s (*Hui and Zhang*, 2007), and in the presence of up to 50

wt% phenocrysts, $\eta \sim 10^8$ Pa.s for the Novarupta dacite (*Mader et al.*, 2013). Thus, the conditions $\tau_k \leq \tau_{dec}$ implies that $k_1 \leq 10^{-9}$ m^2 for permeable outgassing to have been insignificant during Episode I - III, which is the case for all samples. It is also consistent with the relatively modest predicted increase in fragmentation pressure due to measured permeabilities (*Mueller et al.*, 2008). If the magma had been pervasively flow fractured, at an average fracture spacing of $L << 100$m, gas should have escaped into highly permeable fractures at sufficient rates to have resulted in the transition from explosive to effusive eruptive activity. However, like Plinian deposits of other rhyolitic eruptions (*Castro et al.*, 2012, 2013), Episode I - III deposits lack evidence for pervasive shear fracturing. Therefore, a decrease in decompression rates to $\tau_{vis} > \tau_{dec}$ and/or $\tau_k > \tau_{dec}$ is the most feasible explanation for the cessation of sustained explosive magma fragmentation at Novarupta. All else being equal, for this to be the case, the characteristic decompression rate, $\dot{P}$, must have been less than $(\Delta P_f)^2/\eta \sim 10^6$ Pa.s^{-1}. Numerical modeling substantiates these results (Figure 3.5) and illustrates that Episode I-III magmas may have become permeable at a few hundred meters or less below fragmentation depth.

A potential caveat to this assertion is the possibility of permeable outgassing near the conduit walls, as a consequence of shear fragmentation (*Gonnermann and Manga*, 2003; *Tuffen et al.*, 2003) and/ or high permeability of the conduit wall rock (*Stasiuk et al.*, 1993; *Jaupart*, 1998). Such outgassing has been suggested, based on an increase in the proportion of dense clasts near the top og the Episode III fall deposits, and may have produced a low-porosity and high-viscosity magma annulus toward the end of Episode III (*Adams et al.*, 2006a). This would have resulted in an increase in viscous stresses and a decrease in discharge rate. Alternatively, or perhaps concurrently, a decrease in reservoir pressure would have also resulted

in a decrease in eruption rate (e.g., *Jaupart and Allegre*, 1991), albeit modulated by caldera collapse during Episodes I and III (*Hildreth*, 1991; *Fierstein and Hildreth*, 1992).

3.7 Conclusions

Nothing inherent in the characteristics of samples from the 1912 Novarupta Plinian Episodes I-III indicates that permeable outgassing by itself resulted in the transition from sustained explosive to effusive activity. Moreover, there is no indication that Episode V lava required significantly different conditions for fragmentation than prior explosive episodes; it simply did not attain those conditions. The most viable to quiescent lava effusion during Episode V is a decrease in magma ascent and, hence, decompression rate. I thus find that magma permeability was not sufficient condition for the transition from explosive to effusive activity. Instead, a decrease in magma ascent and decompression rate was necessary to end the explosive activity. Once the eruption changed to effusive, there was always sufficient time during ascent for permeable outgassing and loss of porosity.

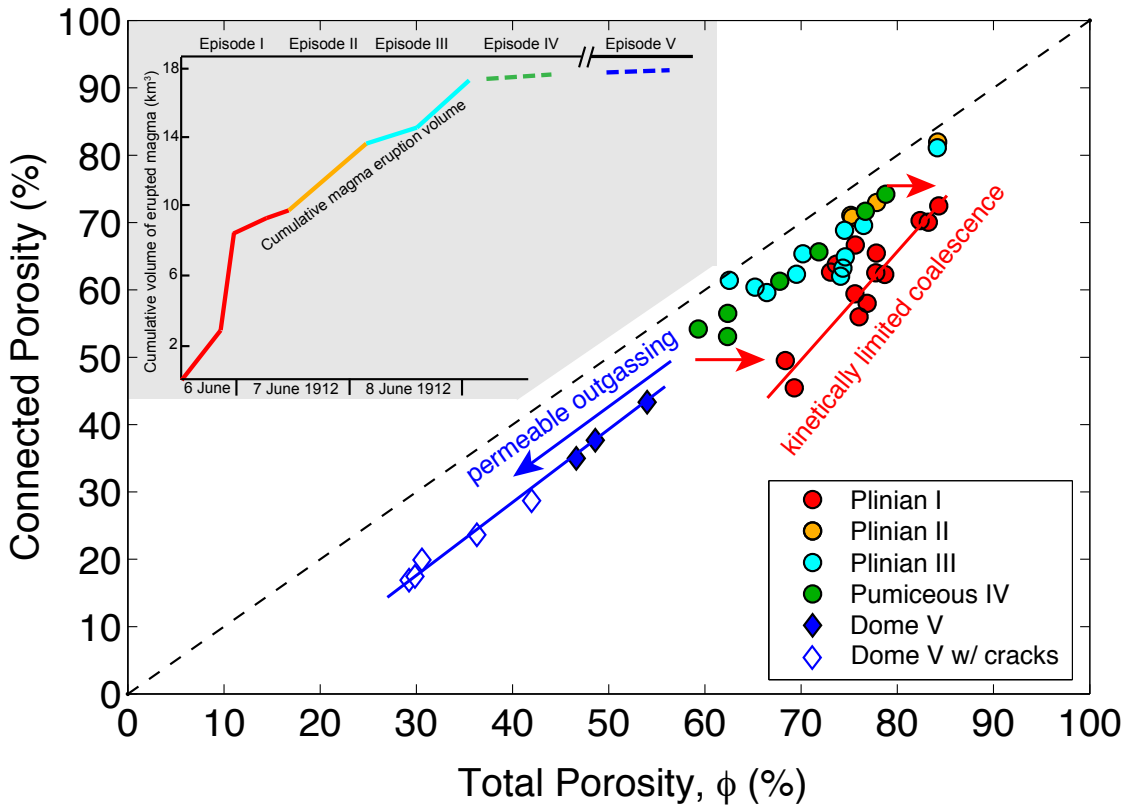

Figure 3.1 : Connected porosity as a function of total porosity, with cumulative volume of erupted magma (inset, as dense rock equivalent; (*Hildreth and Fierstein*, 2012)). Red and blue lines are drawn to guide the eye. Episode I samples have distinctly lower ratio of connected to total porosity than samples of the other episodes, which may be a consequence of kinetically limited coalescence (i.e., bubble nucleation and growth outpace rate at which bubbles coalesce).

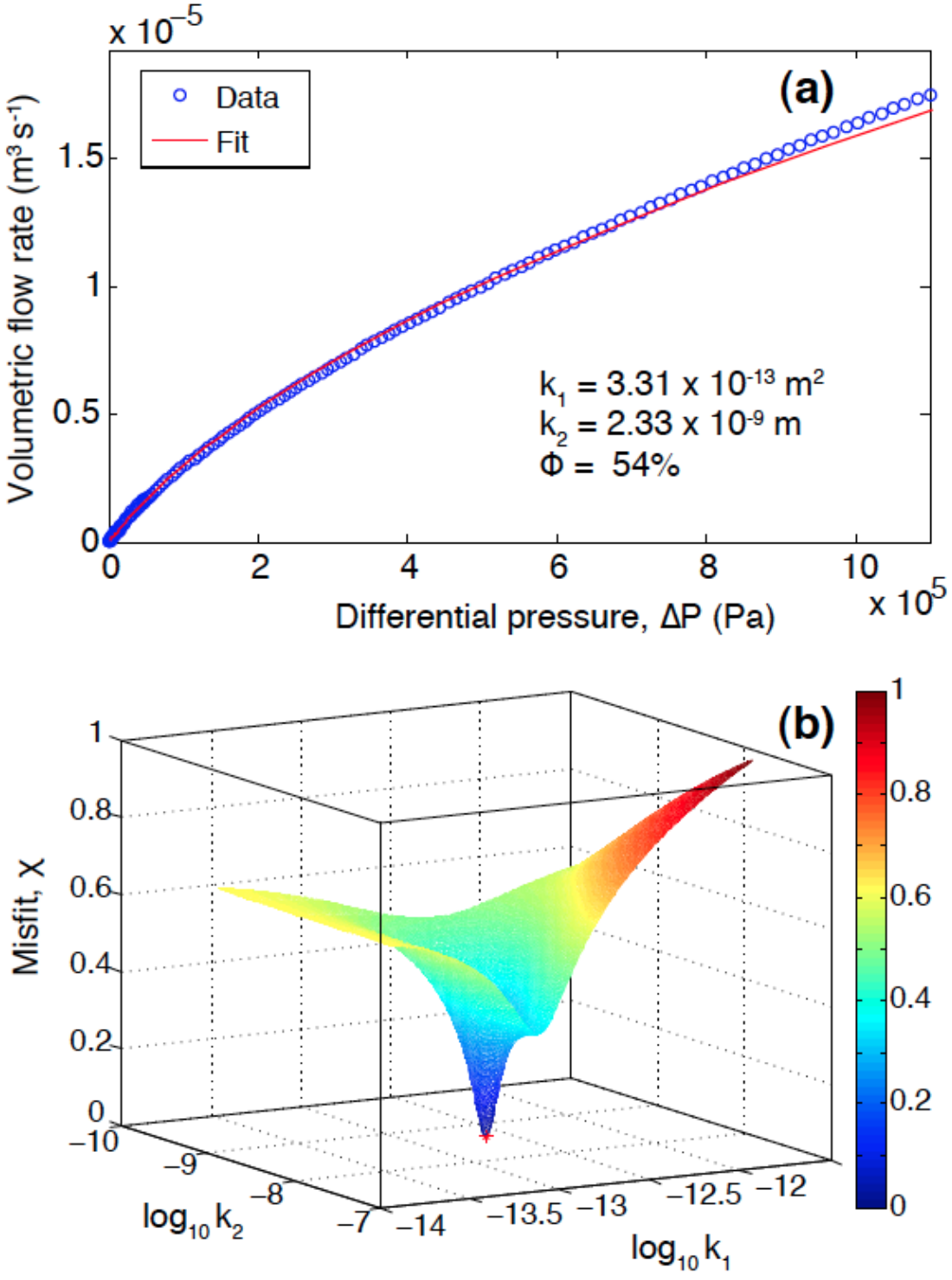

Figure 3.2 : Illustrative example of permeability estimation. Top: Measured volumetric flow rate (blue circles) as a function of pressure difference across sample, obtained using two different flow meters (100 cm^3 s^{-1} and 1000 cm^3 s^{-1}), and the best fit to the data (red curve). Bottom: Misfit χ as a function of $log_{10}(k_1)$ and $log_{10}(k_2)$. The combination of k_1 and k_2 that gives the best fit shown as the blue star.

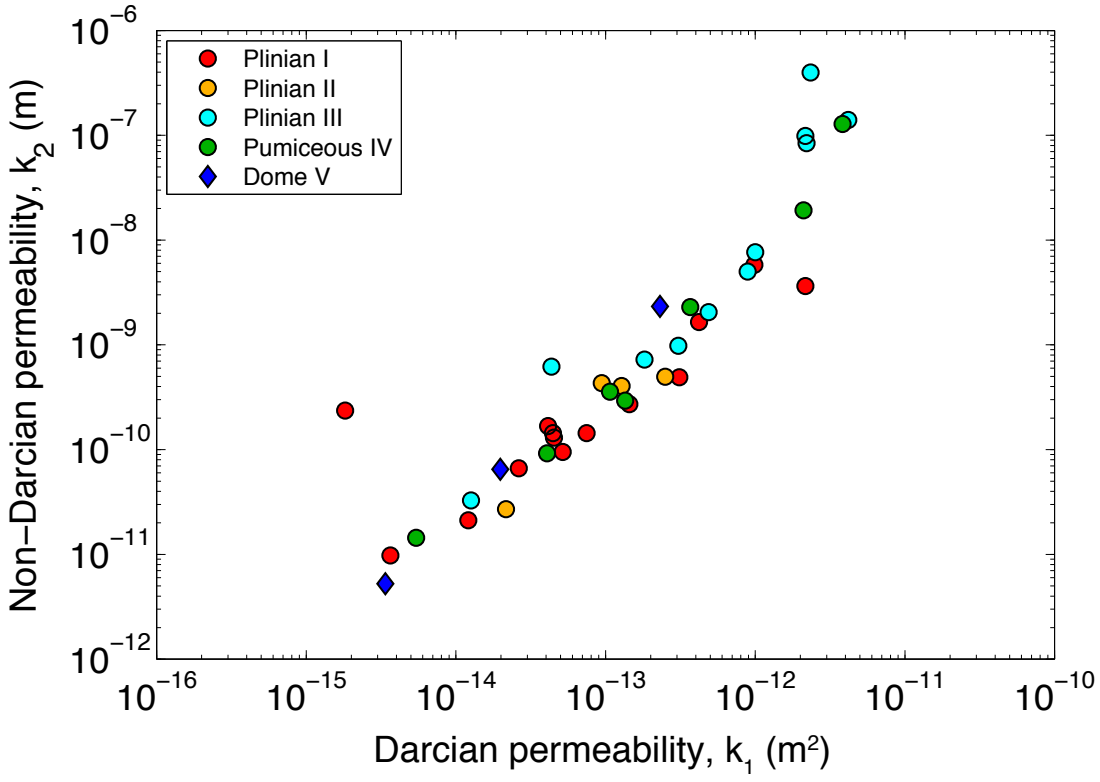

Figure 3.3 : Plot of Darcian versus non-Darcian permeabilities. In this project, non-Darcian permeability values were only used to get the best fit from the flow curves and differential pressures. I did not observe the effect of permeable outgassing due to turbulent gas flow.

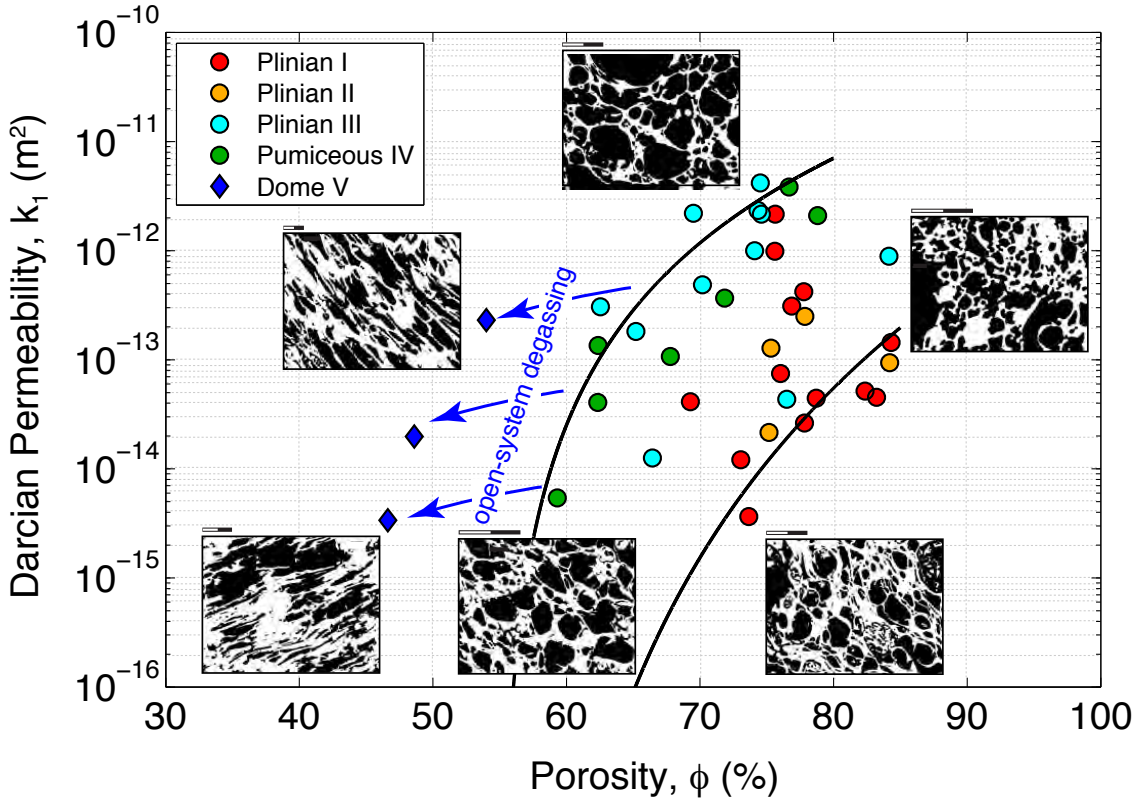

Figure 3.4 : Darcian permeability, $k1$, as a function of total porosity, ϕ. Insets are scanning electron microscopy images of selected samples, with values shown on the graph; black is vesicles, and while is matrix glass. Scale bar for each image is 100 μm.

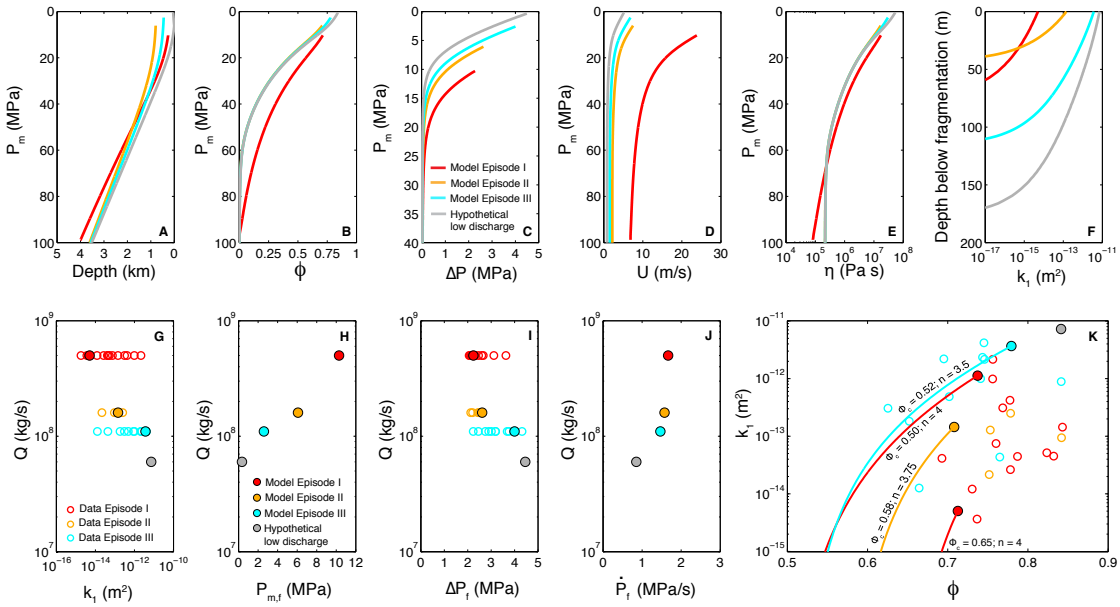

Figure 3.5 : Results from numerical mode up to depth of fragmentation (see Tables 3.4 and 3.5). A-E: Ambient pressure P_m as a function of depth (A), porosity, ϕ (B), gas overpressure, ΔP (C), ascent velocity, U (D), and magma viscosity, η (E). F: Depth below fragmentation as a function of Darcian permeability, k_1. G-J: Discharge rate, Q, as a function of Darcian permeability, k_1 (G), ambient pressure at fragmentation, $P_{m,f}$ (H), gas pressure at fragmentation, ΔP_f (I), and decompression rate at fragmentation, $\dot{P}_f$ (J). K: k_1 as a function of ϕ. Open circles in G-K are estimated or measured values for the Novarupta samples; filled circles are model predictions. Lines in K are for assumed permeabilities of $k_1 - R^2(\phi - \phi_c)^n$ with ϕ and bubble radius r calculated by the model. Note that models provide reasonable fit to observations. Furthermore, at decompression rates of < 1 MP.s^{-1} (the hypothetical low-discharge case), model predicts that fragmentation depth has moved to the surface. Further decrease in decompression rate would not result in sufficient overpressure for fragmentation.

Table 3.1 : Porosity and permeability values of Novarupta samples (Ep. I)

	Sample ID	$\Phi_{conn.}(\%)$	$\Phi_{total}(\%)$	$k_1(m^2)$	$k_2(m)$
Episode I	$89-1-5-1-2$	65.46	77.81	2.63 x 10^{-14}	6.63 x 10^{-11}
(Plinian)	$89-1-5-2-1$	56.01	76.02	7.47 x 10^{-14}	1.44 x 10^{-10}
	$89-1-5-2-2-1$	58.02	76.86	3.11 x 10^{-13}	4.90 x 10^{-10}
	$89-1-5-5-2$	45.46	69.28	4.13 x 10^{-14}	1.68 x 10^{-10}
	$89-1-5-6-1$	63.54	77.76	4.21 x 10^{-13}	1.65 x 10^{-9}
	$89-1-5-6-2$	59.41	75.60	9.87 x 10^{-13}	5.81 x 10^{-9}
	$89-1-5-9$	62.31	78.69	4.45 x 10^{-14}	1.44 x 10^{-10}
	$89-1-5-21$	70.28	82.36	5.17 x 10^{-14}	9.18 x 10^{-11}
	$89-1-5-27$	49.50	68.35	1.82 x 10^{-15}	2.36 x 10^{-10}
	$89-1-12-3$	66.68	75.62	2.16 x 10^{-12}	3.64 x 10^{-9}
	$89-1-12-4-2$	63.81	73.65	3.65 x 10^{-15}	9.76 x 10^{-12}
	$89-1-12-6$	62.65	73.05	1.24 x 10^{-14}	2.04 x 10^{-11}
	$89-1-12-7-1$	72.48	84.31	1.44 x 10^{-13}	2.72 x 10^{-10}
	$89-1-12-7-2$	70.05	83.21	4.52 x 10^{-14}	1.30 x 10^{-10}

Table 3.2 : Porosity and permeability values of Novarupta samples (Eps. II & III)

	Sample ID	$\Phi_{conn.}(\%)$	$\Phi_{total}(\%)$	$k_1(m^2)$	$k_2(m)$
Episode II	$94-01-11-02$	70.77	75.30	1.28 x 10^{-13}	4.05 x 10^{-10}
(Plinian)	$94-01-11-03$	71.07	75.17	2.16 x 10^{-14}	2.70 x 10^{-11}
	$94-01-11-04$	81.97	84.19	9.41x 10^{-14}	4.31 x 10^{-10}
	$94-01-11-05$	72.99	77.84	2.50 x 10^{-13}	4.96 x 10^{-10}
Episode III	$94-01-2003-17-1$	60.41	65.20	1.82 x 10^{-13}	7.24 x 10^{-10}
(Plinian)	$94-01-2003-17-2$	81.11	84.15	8.88 x 10^{-13}	5.01 x 10^{-9}
	$94-01-2003-17-3$	68.86	74.51	4.18 x 10^{-12}	1.40 x 10^{-7}
	$94-01-2003-17-4$	69.58	76.49	4.34 x 10^{-14}	6.20 x 10^{-10}
	$94-01-2003-17-14$	59.59	66.44	1.26 x 10^{-14}	3.27 x 10^{-11}
	$94-01-2D-01$	62.02	74.09	9.98 x 10^{-13}	7.67 x 10^{-9}
	$94-01-2D-02$	61.41	62.54	3.06 x 10^{-13}	9.81 x 10^{-10}
	$94-01-2D-03$	62.32	69.51	2.20 x 10^{-12}	8.40 x 10^{-8}
	$94-01-2D-04$	65.36	70.18	4.87 x 10^{-13}	2.05 x 10^{-9}
	$94-01-7D-01$	64.90	74.59	2.16 x 10^{-12}	9.86 x 10^{-8}
	$94-01-7D-02$	63.22	74.34	2.34 x 10^{-12}	3.97 x 10^{-7}

Table 3.3 : Porosity and permeability values of Novarupta samples (Eps. IV & V)

	Sample ID	$\Phi_{conn.}(\%)$	$\Phi_{total}(\%)$	$k_1(m^2)$	$k_2(m)$
Episode IV	$Post - HBlocks - 7$	53.07	62.34	4.06 x 10^{-14}	9.21 x 10^{-11}
(Blocks)	$Post - HBlocks - 9$	54.21	59.31	5.42 x 10^{-15}	1.44 x 10^{-11}
	$Post - HBlocks - 15 - 2$	74.22	78.80	2.10 x 10^{-12}	1.92 x 10^{-8}
	$Post - HBlocks - 17 - 1$	56.51	62.36	1.35 x 10^{-13}	2.94 x 10^{-10}
	$Post - HBlocks - 22$	65.65	71.84	3.68 x 10^{-13}	2.29 x 10^{-9}
	$Post - HBlocks - 24$	71.67	76.67	3.83 x 10^{-12}	128 x 10^{-7}
	$Post - HBlocks - 43$	61.30	67.78	1.07 x 10^{-13}	3.57 x 10^{-10}
Episode V	$R - Dome - 5 - 1$	34.97	46.63	3.78 x 10^{-15}	5.25 x 10^{-12}
(Dome)	$R - Dome - 5 - 2$	37.67	48.60	1.98 x 10^{-14}	6.50 x 10^{-11}
	$R - Dome - 8 - 2$	28.70	41.98	5.28 x 10^{-16}	7.57 x 10^{-14}
	$R - Dome - 10$	23.64	36.28	1.97 x 10^{-16}	6.13 x 10^{-15}
	$R - Dome - 15$	17.44	29.86	1.62 x 10^{-15}	1.41 x 10^{-12}
	$R - Dome - 22 - 1$	19.90	30.57	1.11 x 10^{-15}	5.63 x 10^{-13}
	$R - Dome - 22 - 2$	16.90	29.23	2.48 x 10^{-16}	3.12 x 10^{-14}
	$R - Dome - 32$	43.33	54.00	2.31 x 10^{-13}	2.33 x 10^{-9}

Table 3.4 : Compositions of Novarupta samples[a] and parameters used for modeling[b]

Sample	wt.% SiO_2 matrix glass	wt.% phenocryst	vol.% rhyolite[c]	vol.% dacite[c,d]	vol.% andacite[c]
Episode I (A)	78.8	1-5	100	0	0
Episode I (B)	72.9-78.7	1-42	47	27	26
Episode II	76.6	25-42	0	100	0
Episode III	76.6	25-42	6	94	0
Episode IV	76.6	25-42	N/A	N/A	N/A
Episode V	78.1	1-5	> 95	< 5	<1

Notes. [a] Based on *Hildreth and Fierstein* (2012) and references therein. [b] Modeling was limited to Episodes I(A), II and III. [c] Relative volumetric proportion of compositional components erupted during the given episode. [d] Matrix (melt) is rhyolitic in composition and bulk composition is due to phenocryst content.

Table 3.5 : Model parameters and values

	Episode I	Episode II	Episode III	Low dischage
Mass discharge[a], Q (kg.s^{-1})	5 x10^8	1.6x10^8	1.1$10^8$	6x10^5
Initial pressure[b], p_m (MPa)	100	125	125	125
Vapor saturation[b] (mole fraction CO_2)	0	0.5	0.5	0.5
Volume fraction phenocryst in matrix[a]	0.02	0.4	0.4	0.4
Bubble number density (m^{-3})	10^{14}	10^{14}	10^{14}	10^{14}
Conduit radius, a (m)	100	100	100	100
Percolation threshold, ϕ_c	0.65 (0.5)	0.58	0.55	0.55
Power-law coefficient, n	4	3.75	3.5	3.5

Notes. [a] Based on *Hildreth and Fierstein* (2012) and references therein. [b] Initial pressures and vapor saturation are based on the work of *Coombs and Gardner* (2001) and *Hammer et al.* (2002).

Chapter 4

Effects of permeability and open-system degassing on the transition from explosive to effusive eruption of rhyolitic magma

I analyzed porosity and permeability of pyroclastic samples from four different Plinian eruptions: the A.D. 181 Taupo eruption, New Zealand; the A.D. 1060 Glass Mountain eruption, California; the A.D. 1314 Kaharoa eruption; and the A.D. 1912 Novarupta eruption, Alaska. I found that Kaharoa samples have the lowest values of porosity and permeability compared to samples from the other three eruptions. Porosity and permeability of Kaharoa samples, as well as their pyroclastic textures, are similar to those from the effusive Episode V of the 1912 Novarupta eruption. I hypothesize that Kaharoa magma might have undergone a high degree of open-system degassing prior to magma fragmentation.

4.1 Introduction

Pyroclasts are excellent records of preserving the conditions at which fragmentation occurs, especially in rhyolitic magma when bubble coalescence time far exceeds the quenching time (*Nguyen et al.*, 2013). Therefore, these pyroclasts are used as a proxy to investigate the open-system degassing at the time of fragmentation through porosity and permeability data. In this chapter, I compare and contrast four different Plinian eruptions of similar compositions, water content, phenocryst

content, bubble size distribution as well as mass discharged rates (Table 4.1). These eruptions are the A.D. 1912 Novarupta, Alaska; the A.D. 1314 Kaharoa, Tarawera, New Zealand; the A.D. 1060 Glass Mountain; and the A.D. 181 Taupo, Lake Taupo, New Zealand.

4.2 Eruptions Studied

4.2.1 Novarupta 1912, Alaska, United States

The A.D. 1912 Novarupta eruption is the largest eruption in the 20^{th} century. It started with Episodes I-III of Plinian eruption, which lasted for $\sim$60 h, followed by Episode IV of Vulcanian activity and ended with Episode V of dome formation which is still present today as Novarupta dome (e.g., *Hildreth and Fierstein*, 2012; *Adams et al.*, 2006b). Eruptive products consist of rhyolite and dacite with some negligible volume of andesite (*Fierstein and Hildreth*, 1992). This study focuses mainly on Episode I with the highest magma discharge rate (Q = 5 x 10^8 $kg.s^{-1}$) and eruptive products comprised mostly rhyolite (*Hildreth and Fierstein*, 2012).

4.2.2 Kaharoa 1314, Tarawera,New Zealand

The A.D. 1314 Kaharoa eruption consists of two stages with the total 13 sub-Plinian to Plinian episodes that occurred along an 8-km long fissure in Tarawera, New Zealand, which produced >9.1 km^3 of rhyolite and followed by the formation of a lava dome that lasted for 4 years (*Leonard et al.*, 2002; *Nairn et al.*, 2004, 2010; *Sahetapy-Engel et al.*, 2014). The first stage produced 7 units (A to G) of lapilli fall deposits toward the southeast of the volcano and is the focus of this study. Analyses of clast size and pumice density suggest that there were some episodes of

steadiness (Unit B) with uniformed clast size and density, and unsteadiness (Unit D) with a wider range of clast size and density (*Carey et al.*, 2013; *Sahetapy-Engel et al.*, 2014). Except for a thin layer of pyroclastic density current of Unit C, the other units were comprised of well sorted lapilli fall deposits with low phenocryst content (4-7 wt.%) (*Sahetapy-Engel et al.*, 2014).

4.2.3 Glass Mountain 1060, Northern California, United States

The A.D. 1060 Glass Mountain eruption is the last episode of the post- glacial eruption of Medicine Lake Volcano, California (e.g., *Heiken*, 1978; *Grove and Donnelly-Nolan*, 1986; *Grove et al.*, 1997). The eruption comprised a Plinian period followed by rhyolite-dacite flows (*Heiken*, 1978). This study focuses on the Plinian phase, which lasted approximately 3-6 h and comprised of mostly rhyolite in the fallout deposit of 0.27 km^3 (*Heiken*, 1978; *Donnelly-Nolan et al.*, 2007). The poorly sorted lapilli products from this episode have the phenocryst content of $<5\%$ and are homogeneous in texture (*Heiken*, 1978).

4.2.4 Taupo 181, Lake Taupo, New Zealand

The A.D. 181 Taupo eruption is the youngest of the two young rhyolitic caldera-forming eruptions at the Taupo Volcanic Zone, New Zealand. It is the world's second largest known eruption in the last 2000 years (*Wilson and Walker*, 1985). The 181 Taupo eruption consists of 7 units. Unit 1 was a phreatomagmatic eruption followed by a Plinian phase of Unit 2. Units 3 and 4 were of phreatoplinian followed by a Plinian activity of Unit 5. Unit 6 recorded an extremely high magma discharge rate of 7 x $10^{10}\ kg.s^{-1}$, which produced the Taupo ignimbrite and ended with Unit 7 of dome formation (e.g., *Wilson*, 1993; *Smith and Houghton*, 1995; *Houghton et al.*,

1998, 2014). The focus of this study is Unit 5, a Plinian eruption which comprised mostly rhyolite.

4.3 Sample Analysis

I measured porosities and permeabilities of all samples using the method presented in Chapter 3, Section 3.4. All samples were drilled into cores of 0.5 - 5 cm in length and 0.5 - 2.5 cm in diameter. I discarded any sample with visually observable cracks to avoid over-estimation of porosity and permeability values.

For porosity analysis, I used a Micromeritics AccuPyc II 1340® and measured the skeletal sample volume, V_{ske} (the sum of the volumes of both solid and isolated vesicles), following Boyle's law. The volume of connected vesicles was calculated as $V_{con} = V_{sample} - V_{ske}$, where V_{sample} is the volume of cylindrical core of the sample. I also crushed some samples into powder and used the same method to determine the density of the glassy matrix, which was then used to calculate the volume of isolated vesicles, V_{iso}. Finally, connected and total porosity were calculated as $\phi_{con} = V_{con}/V_{sample}$, and $\phi_{total} = (V_{con} + V_{iso})/V_{sample}$. Details of operational procedures for pycnometry measurement are presented in Appendix A.

For permeability analysis, I used Capillary Flow Porometer (Model CFP-1100AXL-AC, Porous Media, Inc.®). The samples were sealed with epoxy except for the two ends, which only allowed for the gas flow along the sample length. At the inlet air pressure, P_{in}, varied from 1.1×10^5 Pa up to 6 x 10^5 Pa; whereas the outlet pressure, P_{out}, at the other end was atmospheric pressure. Each sample was measured using 2 - 3 interchangeable flow meters in order to achieve several orders of magnitude in flow rates. For all measurements, the controlled pressure gradient across the sample length was thus between 1 and 5×10^5 Pa m^{-1}. The measured volumetric

flow rate of air, Q, was between 3×10^{-3} and 5×10^{-7} m^3 s^{-1}, with an accuracy $\sim 5 \times 10^{-8}$ m^3 s^{-1} ($\approx 1\%$ of the minimum measured flow rate).

The data from this method were pressure gradients, $\Delta P = P_{in} - P_{out}$, and corresponding volumetric flow rates, Q. I estimated Darcian permeability, k_1, and non-Darcian permeability, k_2 applying Forchheimer's equation (e.g., *Reynolds*, 1900; *Forchheimer*, 1901; *Rust and Cashman*, 2004) for a compressible gas (Equation 3.1) and using a grid search method (e.g., *Tarantola*, 1987).

4.4 Results and Discussion

4.4.1 Porosity

Figure 4.1 shows that porosities of Kaharoa samples range approximately from 35% to 60%, which are similar to those of the effusive episode of the Novarupta eruption (Episode V, Chapter 3). Furthermore, the trend in connected versus total porosity for Kaharoa samples is also similar to that of the dome samples of Episode V. In contrast, the other three eruptions have a much higher porosity range, between 45% and 85%.

4.4.2 Permeability

Figure 4.2 shows that Kaharoa permeabilities range 1-2 orders of magnitude lower than those of the other three eruptions, even lower than that of the effusive Episode V of the Novarupta eruption. The low porosity and permeability values suggest two competing hypotheses: (1) Kaharoa magma became permeable at a low porosity threshold and magma ascent rate was much faster than bubble growth and coalescence rates; or (2) the Kaharoa magma became permeable at a high porosity

threshold, underwent a high degree of open-system degassing and the permeable pathways partially collapsed, resulting in low porosity and permeability (Figures 4.2 and 4.4, *Eichelberger et al.* (1986); *Westrich and Eichelberger* (1994a)).

The resemblance of porosity trend to that of the effusive Episode V of the Novarupta eruption, along with textural observation of flattened vesicles in many Kaharoa samples (Figure 4.3, *Carey et al.* (2013)) is likely to support the second hypothesis.

4.5 Conclusions

Of all four eruptions studied pyroclastic samples of the Kaharoa eruption display the lowest range of porosity and permeability. These low values, along with textural observation of elongate vesicles in pyroclasts, resemble those of dome samples of the effusive Episode V of the Novarupta eruption. I hypothesize that Kaharoa magma might have undergone a high degree of open-system degassing.

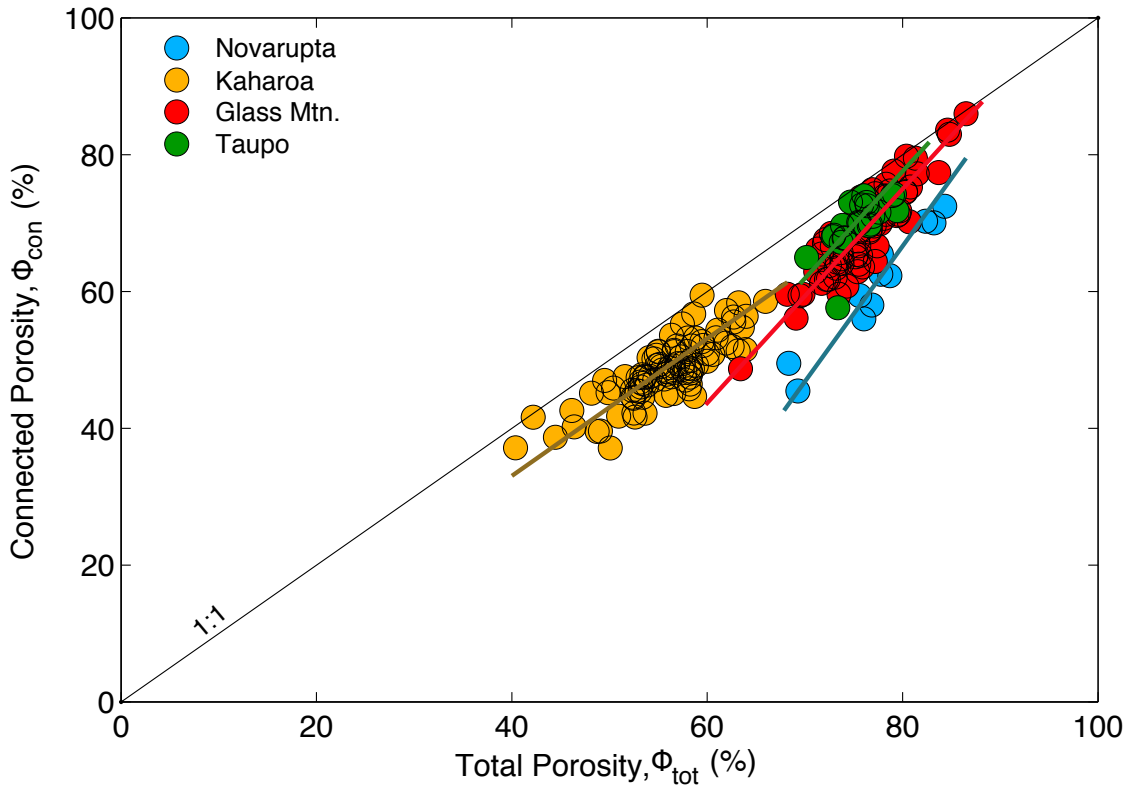

Figure 4.1 : Connected porosity, ϕ_{con} as a function of total porosity, ϕ_{tot}. Orange line represents Kaharoa porosity trend, whereas blue, red and green lines are for the porosity trends of Novarupta, Glass Mountain and Taupo, respectively. The 1:1 line is when $\phi_{con} = \phi_{tot}$.

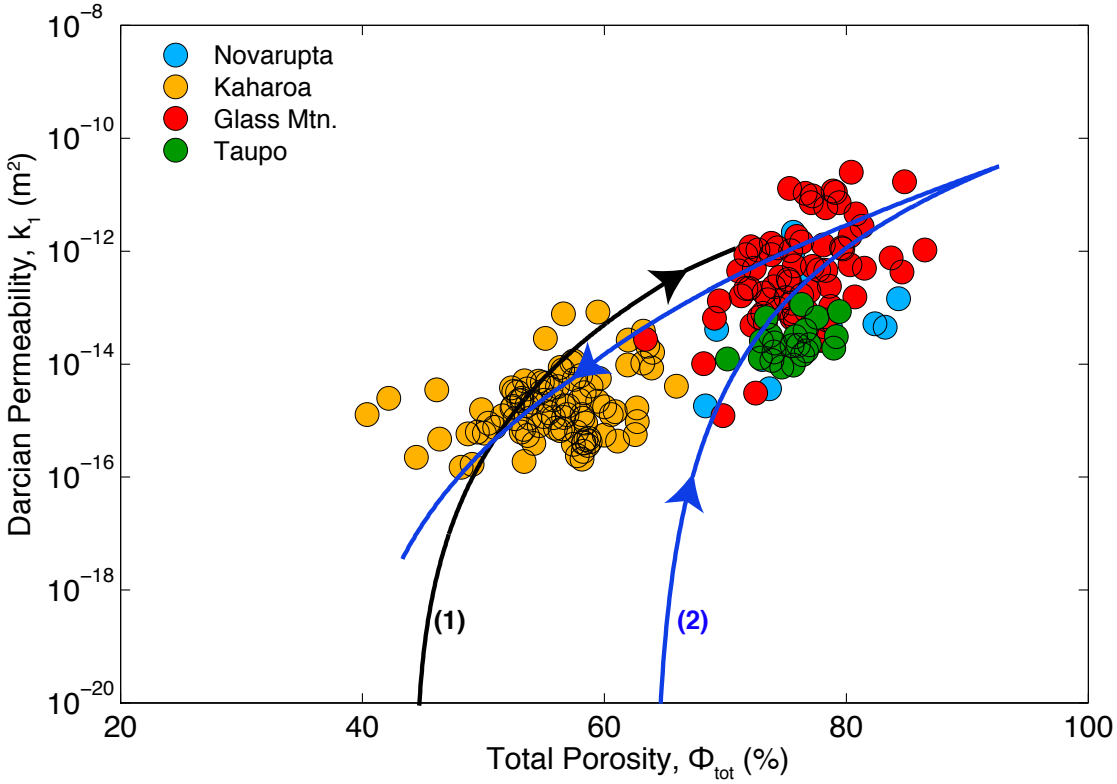

Figure 4.2 : Darcian permeability, k_1, versus total porosity, ϕ. Kaharoa samples show much lower ranges of permeability and porosity values than those of the other eruptions. Black line is a schematic diagram representing the power-law relationship of permeability and porosity in hypothesis (1), where Kaharoa magma became permeable at a low porosity threshold. Blue lines indicate a schematic diagram of permeability development in hypothesis (2), where Kaharoa magma became permeable at a high porosity threshold, underwent some degree of open-system degassing and the permeable pathways partially collapsed.

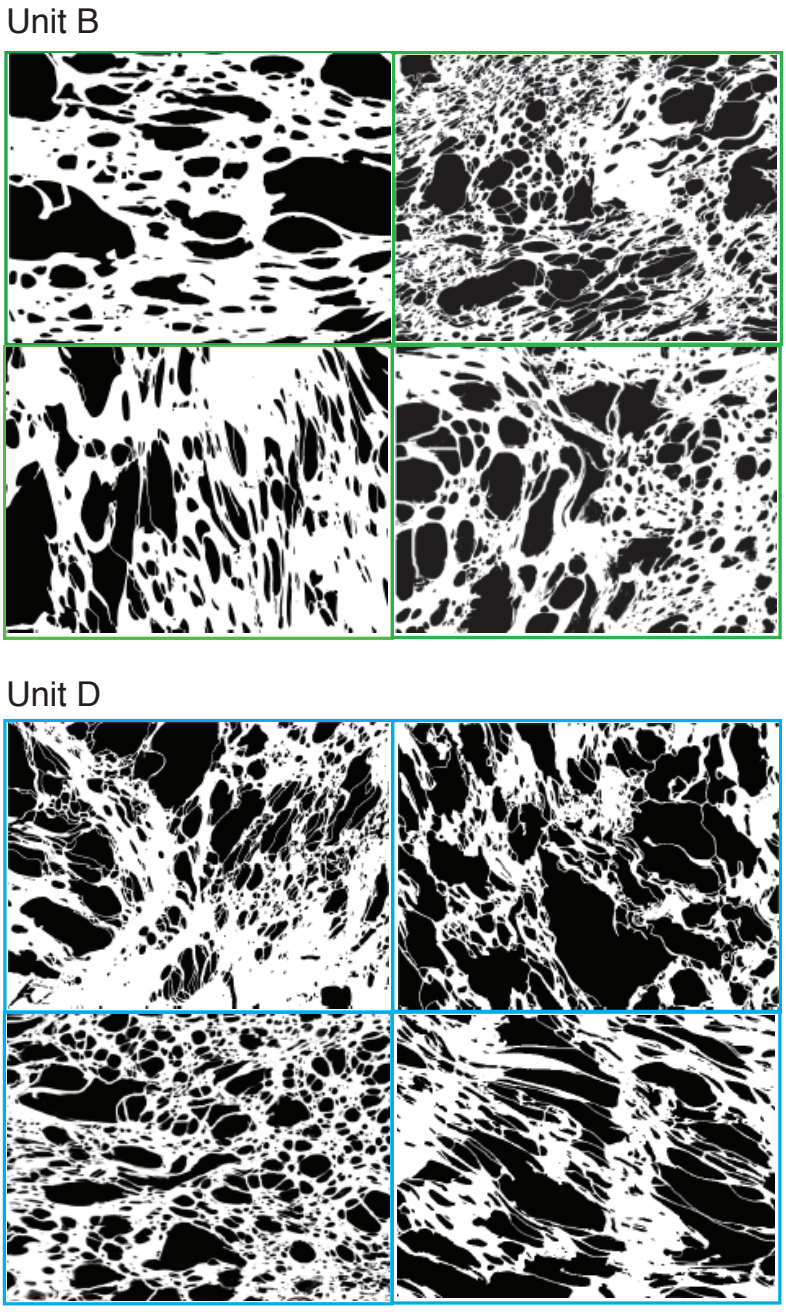

Figure 4.3 : Scanning electron images of Kaharoa samples from Units B and D show that the majority of the samples display flattened vesicles. The field of view is 500 μm (Modified from *Carey et al.* (2013)).

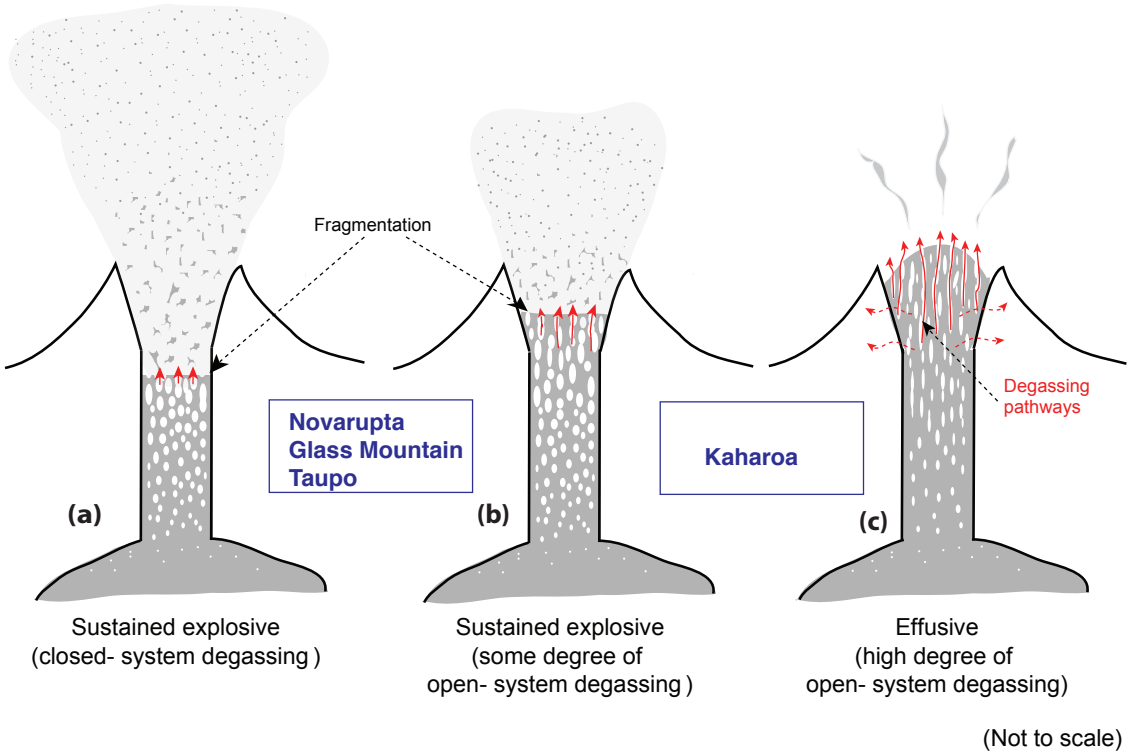

Figure 4.4 : Schematic diagram of a Plinian eruption, ranging from explosive (a, b) to effusive (c) activity. Hypothetically, Kaharoa eruption would be close to (c), whereas Novarupta, Glass Mountain and Taupo eruptions are between (a) and (b).

Table 4.1 : Composition of and other parameters of 4 eruptions in this study

	Novarupta[a]	Kaharoa[b]	Glass Mountain[c]	Taupo[d]
wt. $\%SiO_2$ in matrix glass	78.8	76 - 77	72 - 75	N/A
wt. $\%H_2O$	1	4.93	4.6	3.6 - 4.3
wt. $\%$ phenocryst	1 - 5	4 - 7	$<$5	2 - 3.5
vol. $\%$ rhyolite	100	100	100	100
Mass discharge[a], Q (kg.s^{-1})	5 x10^8	2.5 x10^8	10^8	10^8
Melt density, ρ_m (kg.m^{-3})	2400	2350	2430	2400
Melt temperature, T($\circ$C)	850	880	N/A	850
Bubble number density (m^{-3})	10^{14}	10^{14} -10^{15}	4 x10^{14}	3 x10^{14} - 3 x10^{15}
Average bubble radius, r (μm)	30	20	12.1	35

Notes.

[a] Based on *Hildreth and Fierstein* (2012) and references therein. Here we only analyzed Episode I of Novarupta eruption for relevant comparison to the other 3 eruptions. [b] Based on *Leonard et al.* (2002); *Nairn et al.* (2004, 2010); *Carey et al.* (2013); *Sahetapy-Engel et al.* (2014). [c] Based on *Heiken* (1978); *Grove and Donnelly-Nolan* (1986); *Grove et al.* (1997); *Donnelly-Nolan et al.* (2007). [d] Based on *Wilson* (1993); *Smith and Houghton* (1995); *Houghton et al.* (1998, 2014).

Chapter 5

Conclusions and Future Directions

The principal findings of the thesis include:

1. New laboratory experiments provide constraints on inter-bubble film thinning and bubble coalescence as a consequence of liquid drainage by gravitational and capillary forces. To ensure dynamic similarity to magmatic systems, the experiments are at small Reynolds numbers (Re $\ll 1$) and cover a wide range of Bond numbers ($10^{-3} \leq$ Bo $\leq 10^{2}$). Results indicate that at Bo < 0.25 film drainage is due to capillary forces, whereas at Bo > 0.25 gravitational forces result in film thinning. The film drainage time scale is given by $t \sim C\ ln(\alpha)\ \tau$, and is orders of magnitude faster than previously assumed for magmatic systems. Here $C \sim 10$ is an empirical constant, α is the ratio of initial film thickness to film thickness at the time of rupture, and τ is the characteristic capillary or buoyancy time scale at values of Bo < 0.25 and Bo > 0.25, respectively.

2. I measured porosities and permeabilities in samples from the A.D. 1912 eruption of Novarupta volcano, Alaska, and analyzed them within the context of well-constrained eruptive sequence that encompasses sustained explosive and effusive activity. For the explosive samples, I found that the degree of vesicle interconnectivity, measured as the ratio of connected to total porosity, decreases with the phenocryst content and with increasing eruption intensity. Permeabilities of explosive samples show a weak dependence on porosity. Dome samples are not significantly different in permeability, but are of lower porosity, which together

with abundant flattened vesicles is consistent with bubble collapse by permeable outgassing. Numerical modeling indicates that outgassing alone was insufficient to affect the transition to effusive activity. Rather, the change from explosive to effusive activity was probably a consequence of high versus low magma ascent rates.

3. I analyzed porosity and permeability of pyroclastic samples of four different Plinian eruptions: the A.D. 181 Taupo eruption, New Zealand; the A.D. 1060 Glass Mountain eruption, California; the A.D. 1314 Kaharoa eruption; and the A.D. 1912 Novarupta eruption, Alaska. I found that of all eruptions studied, Kaharoa samples have the lowest values of porosity and permeability recorded for a Plinian-style eruption. Furthermore, porosity and permeability data, as well as pyroclastic textures of Kaharoa samples are similar to those of effusive Episode V of the 1912 Novarupta eruption. I hypothesize that Kaharoa eruption might have undergone a high degree of open-system degassing.

5.1 Future Directions

While obtaining film drainage timescales in basic cases, such as gravitational and capillary drainage, is important, my next step is to explore the more complicated cases such as film drainage in multiple bubble systems, shear-induced film drainage and film drainage caused by fluid flows (e.g., decompression). These are more realistic processes applicable to magmatic processes inside the magma conduit during a volcanic eruption.

Even though permeability has been intensively studied, percolation threshold and permeability development are not well constrained (e.g., *Eichelberger et al.*, 1986; *Klug and Cashman*, 1996; *Mueller et al.*, 2005; *Takeuchi et al.*, 2005; *Adams et al.*,

2006a; *Wright et al.*, 2007; *Mueller et al.*, 2008; *Nakamura et al.*, 2008; *Takeuchi et al.*, 2009; *Rust and Cashman*, 2011; *Degruyter et al.*, 2012). My plan is to conduct analog experiments to investigate permeability development. Specifically, I plan to perform decompression experiments and vary decompression rates to allow for bubbles to grow and coalesce in epoxy. This epoxy is a viscous and fast-curing epoxy that can be locked in texture within minutes to capture each step of decompression process. In other words, I plan to produce synthetic porous samples resembling pumices at each step of decompression process to investigate permeability development during a volcanic eruption.

Another goal is to develop a numerical model for open-system degassing to access the inaccessible conditions inside the magma conduit prior to fragmentation. This model is similar to that of diffusive bubble growth and conduit flow model but additional parameter for open-system degassing. The purpose of this model is to understand how open-system degassing plays in a role in the transition from explosive to effusive eruption.

Appendix A

A.1 Helium Pycnometry

To determine the porosity of a volcanic rock sample, we used the AccuPyc II 1340 by Micromeritics Instrument Corporation, which includes three units for different chamber sizes (Figure A.1). Helium is used to penetrate all the connected vesicles in the porous sample in order to measure the connected void volume. Each unit includes two chambers connected to each other by an Expansion valve as seen in the diagram (Figure A.2). The principle of this method is based on Boyle's law. The ideal gas law for chamber $C1$, which is the calibration chamber, is expressed as,

$$P_1 V_1 = n_1 RT, \tag{A.1}$$

where P_1 is elevated pressure, V_1 is the chamber volume, n is the number of gas molecules in the chamber, R is the gas constant and T is the ambient temperature.

Subsequently, the ideal gas law for chamber $C2$, which is the sample chamber at atmospheric pressure, is as,

$$P_2 V_2 = n_2 RT, \tag{A.2}$$

Once started, the Fill valve opens and the gas fills the first chamber of known volume. When the Fill valve is closed, the Expansion valve between the two chambers is open, which allows gas to enter the sample chamber and the pressures in both chambers adjust to the new value, P. The mass balance of the two connected

chambers is expressed as,

$$P(V_1 + V_2 - V_{ske}) = (n_1 + n_2)RT. \tag{A.3}$$

Here V_{ske} is the skeletal volume of the sample, which is the sum of the volumes of both solid and isolated pores ($V_{ske} = V_{solid} + V_{iso}$). Equations A.1 and A.2 give the values of n_1 and n_2 as the other values are known. Replace n_1 and n_2 in Equation A.3, V_{ske} is calculated. The volume of connected pores is calculated as $V_{con} = V_{sample} - V_{ske}$, where V_{sample} is the volume of cylindrical core of the sample.

We also crushed some samples into powder to measure the density of the solid part (DRE) using the same method. The volume of the isolated pores is then calculated as,

$$V_{iso} = V_{ske} - V_{solid} = V_{ske} - \frac{m}{DRE}, \tag{A.4}$$

where m is the mass of the sample. The connected porosity and total porosity are then calculated as,

$$\phi_{con} = \frac{V_{con}}{V_{sample}}, \tag{A.5}$$

$$\phi_{tot} = \frac{V_{con} + V_{iso}}{V_{sample}}. \tag{A.6}$$

A.2 Detailed Procedures of Pycnometry Measurement

Volcanic samples are cored into cylinders of 0.5 - 2.5 cm in diameter and 1 - 5 cm in length (Figure A.3). We then measure the diameter, length and mass of the sample. The pressure range for the AccuPyc II 1340 is from 0 to 19.5 psi. Therefore, the pressure regulator should be set at $\approx$ 21 psi (Figure A.4).

Before measuring the sample, a necessary step is to calibrate the volume of the sample chamber. All the steps are shown in Figure A.5. First, the calibration is with the empty chamber, then we place the calibration standard inside the chamber and continue the calibration procedures.

Once the calibration is done, the sample is placed inside the chamber. Alternatively, the insert capsule is used to make sure that the volume of the sample is $> 10\%$ of the volume of the chamber to avoid machine error. One then sets the sample default including sample name in sequence, detailed notes, and what parameters to show in the report (Figure A.6). For higher accuracy, one could set a higher number of cycles, which will also take a longer time for each measurement. Figures A.7 and A.8 show a measurement in progress and the final report. The volume measurement is the volume of the skeleton, V_{ske}.

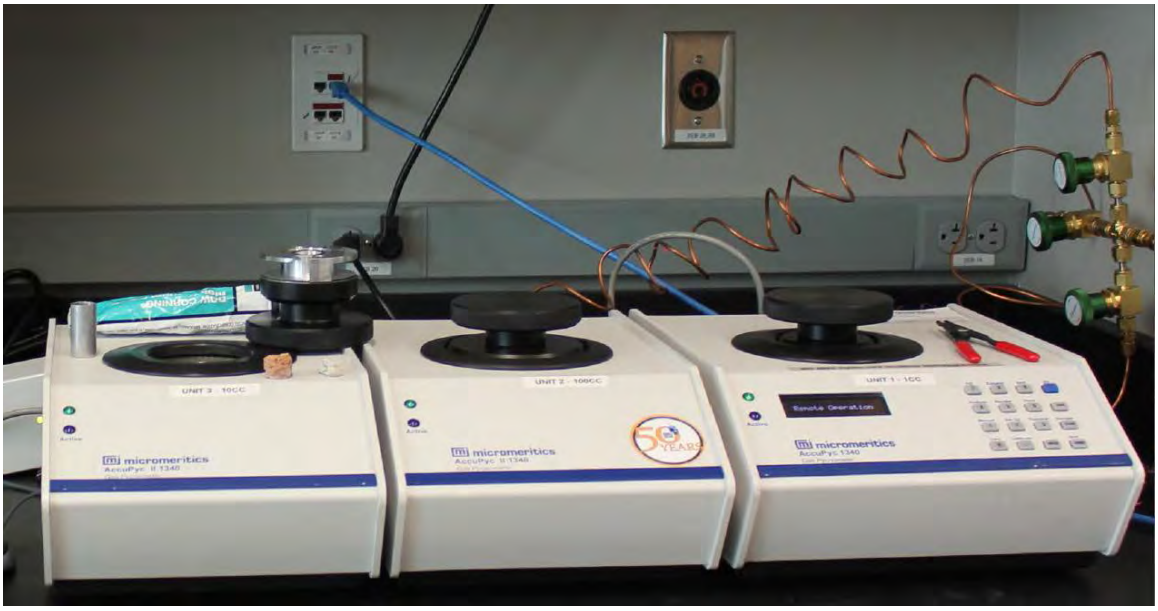

Figure A.1 : The Micromeritics AccuPyc II 1340 with three different units. Unit 1 is on the right, which is also a main unit with a screen displaying controlled parameters such as pressure, temperature, etc. This unit has the smallest chamber of 1 cm^3. Unit 2 is in the middle with the 10 cm^3 chamber, and Unit 3 on the left has the largest chamber of 100 cm^3. Of all three units, there are several inserts, which are smaller capsules to fit inside the chambers with the purpose of measuring smaller samples. Note that if the volume of the sample is less than 10% of the chamber volume, the measurement is not accurate. Therefore, chamber inserts are necessary in some cases.

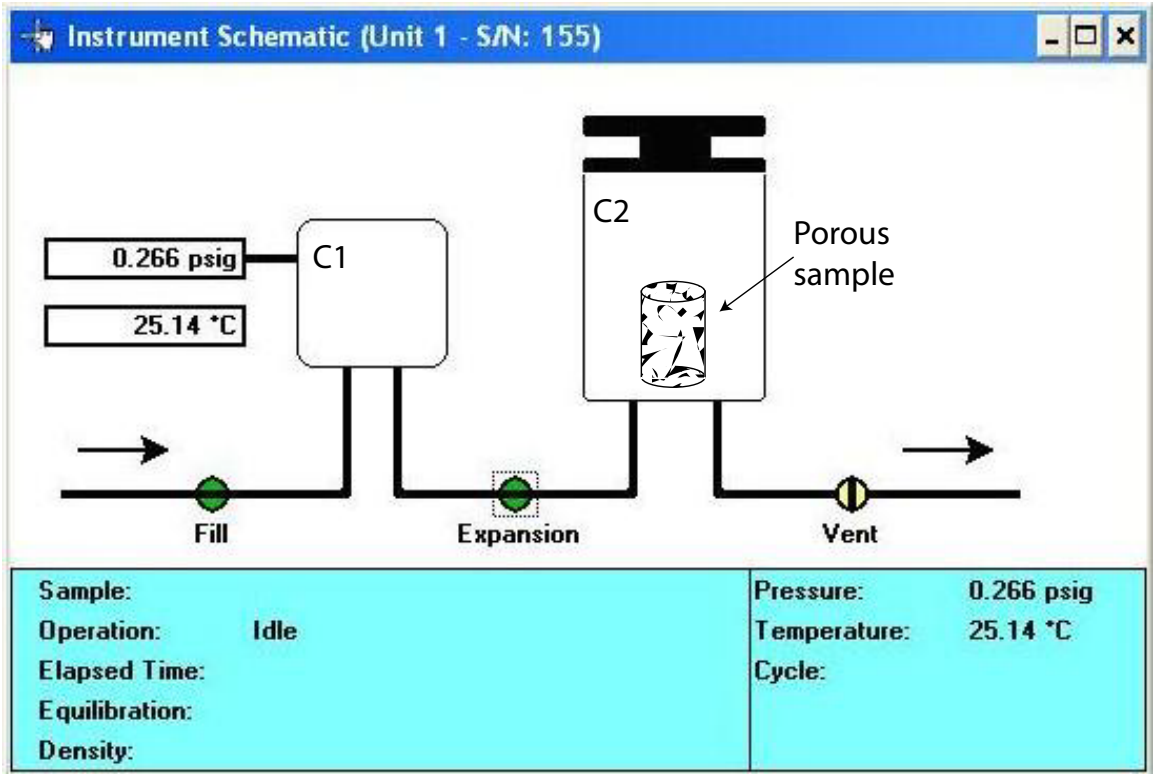

Figure A.2 : A schematic diagram of the AccuPyc II 1340 showing the calibrated chamber, $C1$ and sample chamber, $C2$. There are three valves. The Fill valve is to fill the calibrated chamber, the Expansion valve is to connect the two chambers and the Vent valve is to release the gas in the chambers after all pressure values are recorded.

Figure A.3 : Top image is a sample of an explosive pyroclast that was cored using a drill press. Bottom image is the sample core.

Figure A.4 : An image of inlet pressure. The pressure regulator should be set at $\sim$ 21 psi.

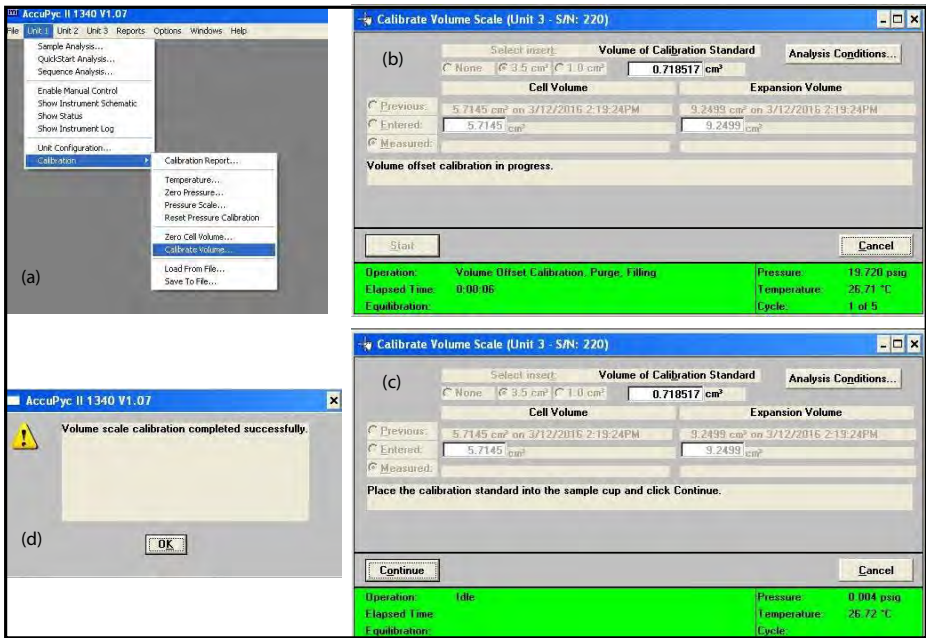

Figure A.5 : Volume calibration before measuring the sample. (a) Choose the appropriate unit and procedure for calibration. (b) Calibration with the empty chamber. (c) Calibration with the manufactured standard. (d) Calibration is done and ready for sample measurement.

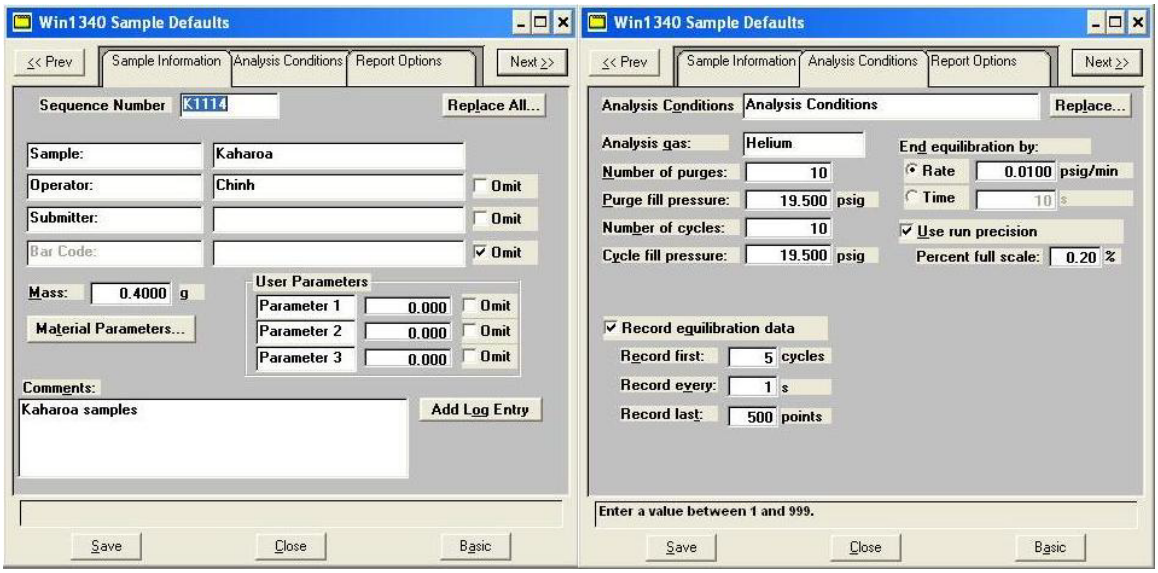

Figure A.6 : Sample defaults. To measure a set of similar samples, it is more effective to set the sample defaults with all the information as above. The left image shows basic information including sample identification, description and extra information. The right image shows all the parameters, which include the gas used for the measurement, the maximum fill pressure of 19.5 psi, equilibration either by rate or time, number of purges and number of cycles. With the last two parameters, the higher the number, the more accurate measurement. Another option for accuracy is to set at a certain percentage. Whichever is reached first (number of cycles or the set accuracy), the measurement will stop.

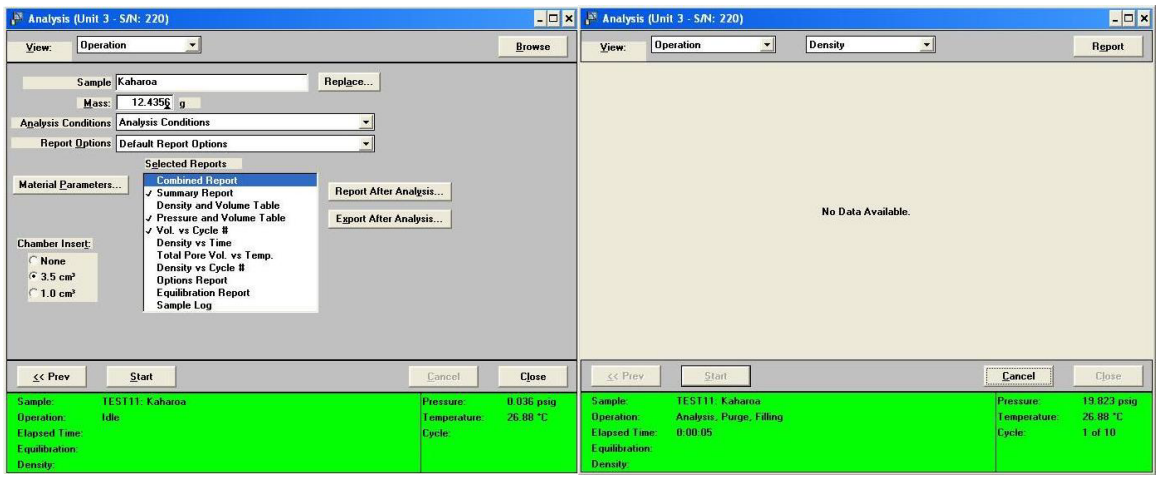

Figure A.7 : Pycnometry measurement in progress.

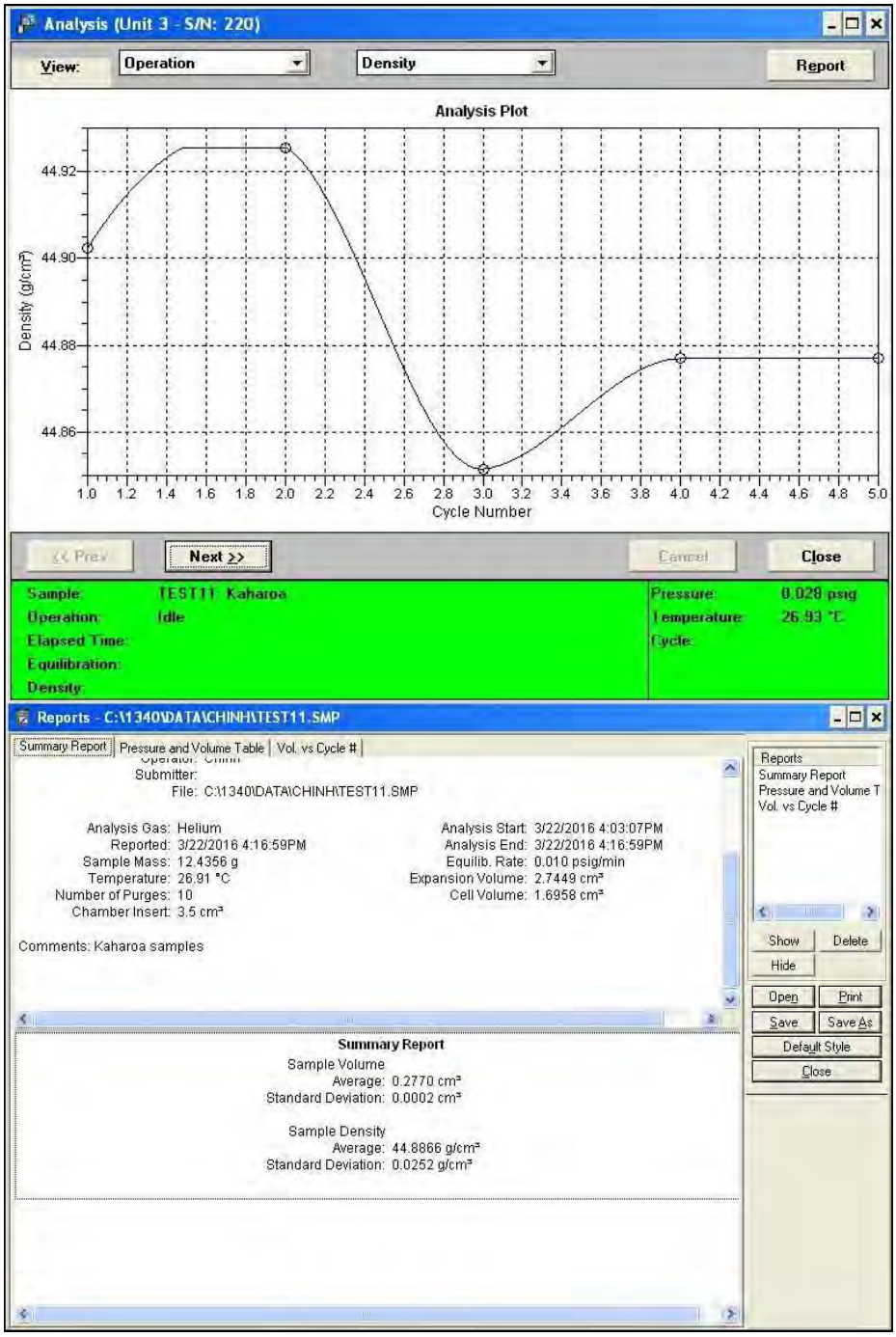

Figure A.8 : Analysis plot and summary report of the results.

Appendix B

The methodology of permeability measurement using the Capillary Flow Porometer (Model CFP-1100AXL-AC, Porous Media, Inc. ®) has been described in details in Chapter 3, Section 3.4. Here I describe gas permeametry, in which volumetric flow rates of a fluid (ambient air in this case) and the pressure gradients across the sample were measured to estimate permeability using Forchheimer's equation.

Figure B.1 shows the schematic diagram of the operational procedures of gas permeametry, in which compressed air is connected to one end of the sample, flows through the sample and exits the other end, where volumetric flow rate is recorded by a flow meter. Gas pressure increases in small steps. The differential pressures across the sample and the corresponding flow rates are measured as a function of differential pressure. Permeability of the sample is then computed using gas flow rates, pressure gradients and sample dimensions.

B.1 Sample Preparation

A plexi-glass plate with a hole of the same diameter of the sample is used to mount the sample into the hole. A coat of epoxy is applied to seal the side of the sample and left it overnight to make sure that the epoxy is completely solidified. This epoxy seal had the purpose of constraining the gas to flow along the sample axis without flowing out radially. I also used compressed air to blow through the sample before measurement to remove any dirt.

B.2 Operational Procedures of Gas Permeametry

I used several flow meters (Figure B.3) to obtain different ranges of volumetric flow rate in order to increase the accuracy of the measurement. The error for each flow meter is within 1%. To begin, I used the highest flow meter, which is 200 l/m. This flow meter allows the highest flow rate to pass through the sample corresponding to the highest pressure gradient. Unless the sample has very low permeability (expected based on very low porosity), this step is necessary because it will potentially cleanse out all the permeable pathways in the sample (tiny dusts, for example). Steps of measurement are as follows,

Step 1: Apply a small amount of vacuum grease on the O-rings of the chamber for better seal. Note that only apply a little amount, otherwise it might block the air flow. Place the sample inside the chamber and seal it (Figure B.4);

Step 2: Connect the proper flow meter to the Capillary Flow Porometer (Figure B.5), and also make sure that the porometer is connected to the computer;

Step 3: Turn on the compressed gas line, the porometer and the computer;

Step 4: Choose the proper software for the porometer (Figure B.6a);

Step 5: Once the software is open, a window pops up. Click on Auto Test to start the measurement (Figure B.6b);

Step 6: Enter the name of the output file (usually related to the sample identi-

fication) and all parameters of the sample including the sample dimensions and pressure gradient range (any value between 0 - 75 psi). One also needs to make sure to choose the appropriate test type, in this case it is gas permeametry using ambient air (Figure B.7);

Step 7: The screen will show the measurement in progress. Once the analysis is completed, a plot of pressure gradient and volumetric flow rate is displayed (Figure B.8);

Step 8: Run the report by clicking on the Report button. A report window will pop up and one can select the type of output file (Figure B.9);

Step 9: Once all is done, close the software, remove the sample, disconnect the flow meter, and turn off the gas line, porometer and computer.

Note that before measuring the real samples, one should perform a leak test with a blank steel plate. Lastly, one should measure at least one of the standards and compare the results to those posted on the side of the porometer. If the values are close to the posted values, the porometer is good for use.

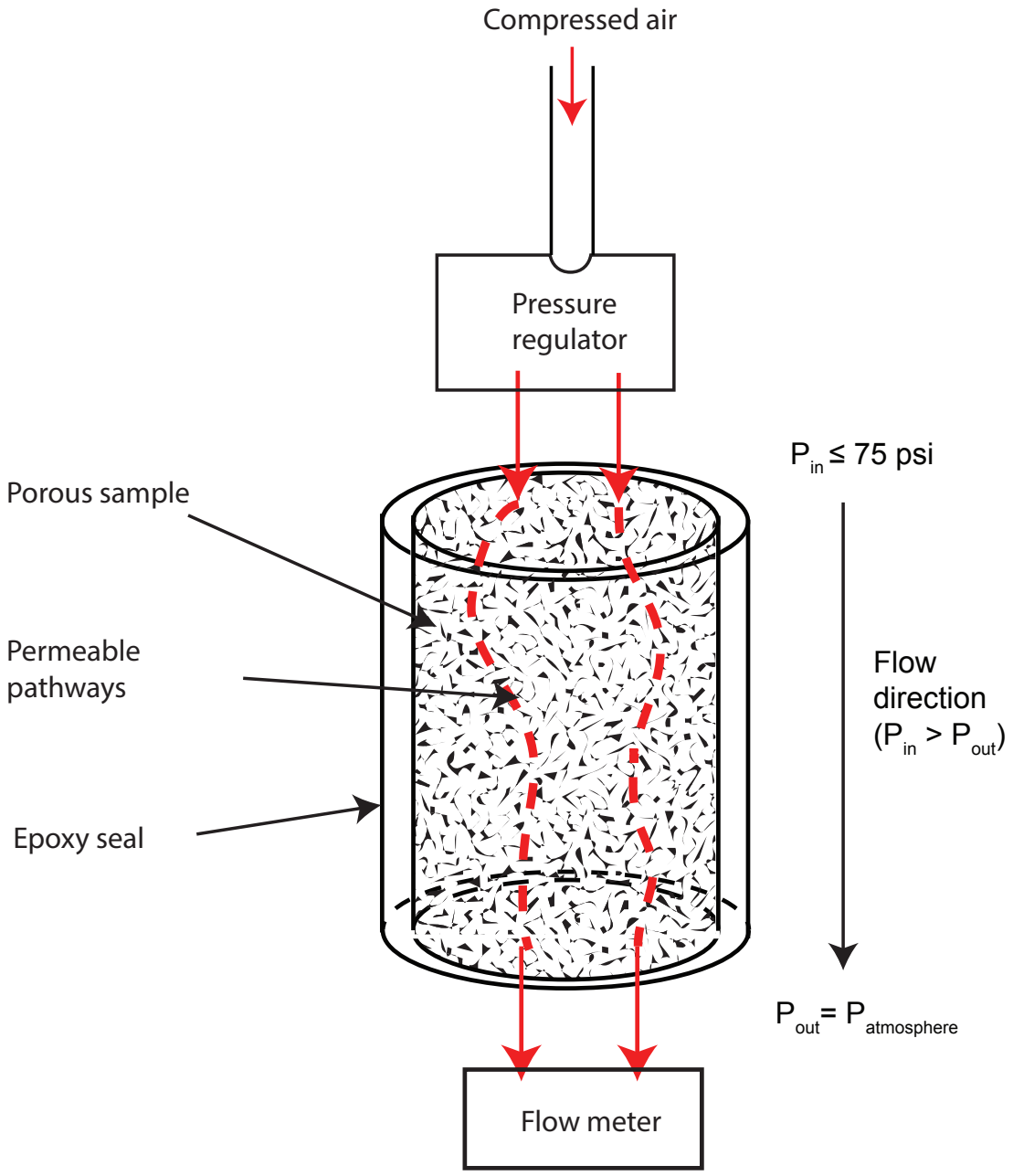

Figure B.1 : Schematic diagram showing the operational procedures for gas permeametry using the Capillary Flow Porometer. Elevated compressed air is connected to a pressure regulator, which then allows gas to enter the top of the sample and flow to the bottom at small intervals of pressure gradients. At the exit, the volumetric flow rates are recorded by a flow meter. Permeability of the sample is then computed using gas flow rates, pressure gradients and dimensions of the sample.

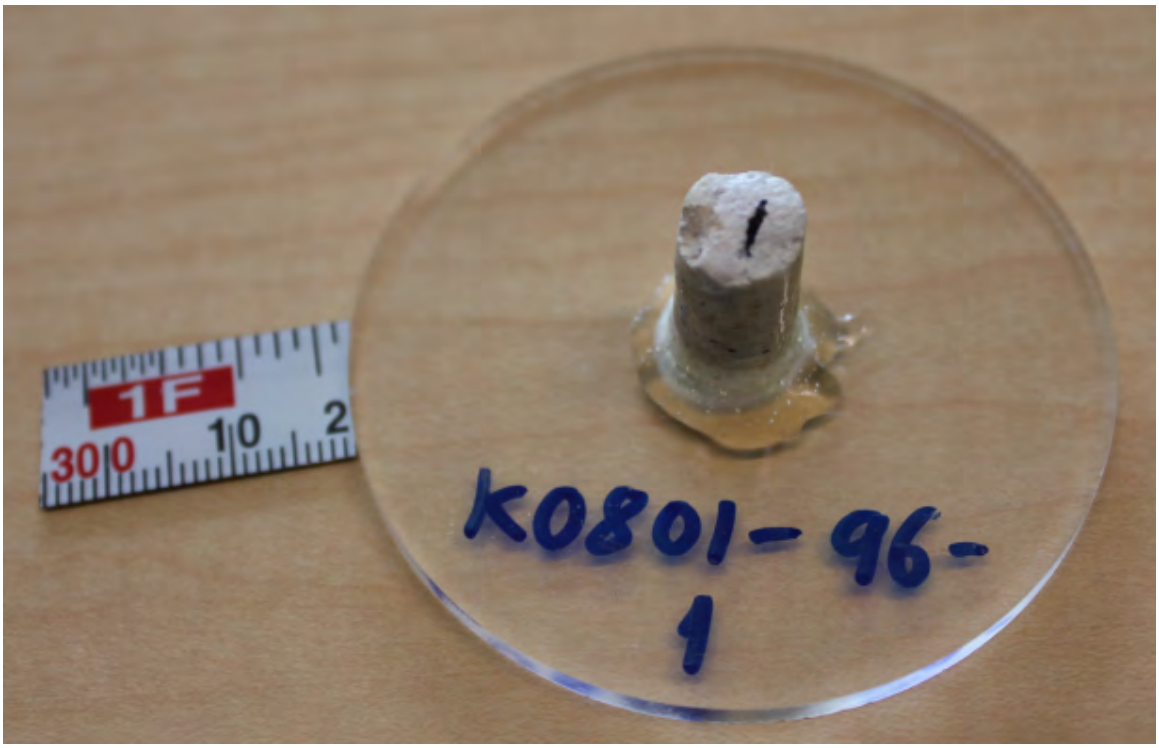

Figure B.2 : An example of sample preparation. A cylindrical sample was sealed with epoxy on the side and mounted onto a plexi-glass plate, which only allowed gas to flow through from one end to the other end of the sample.

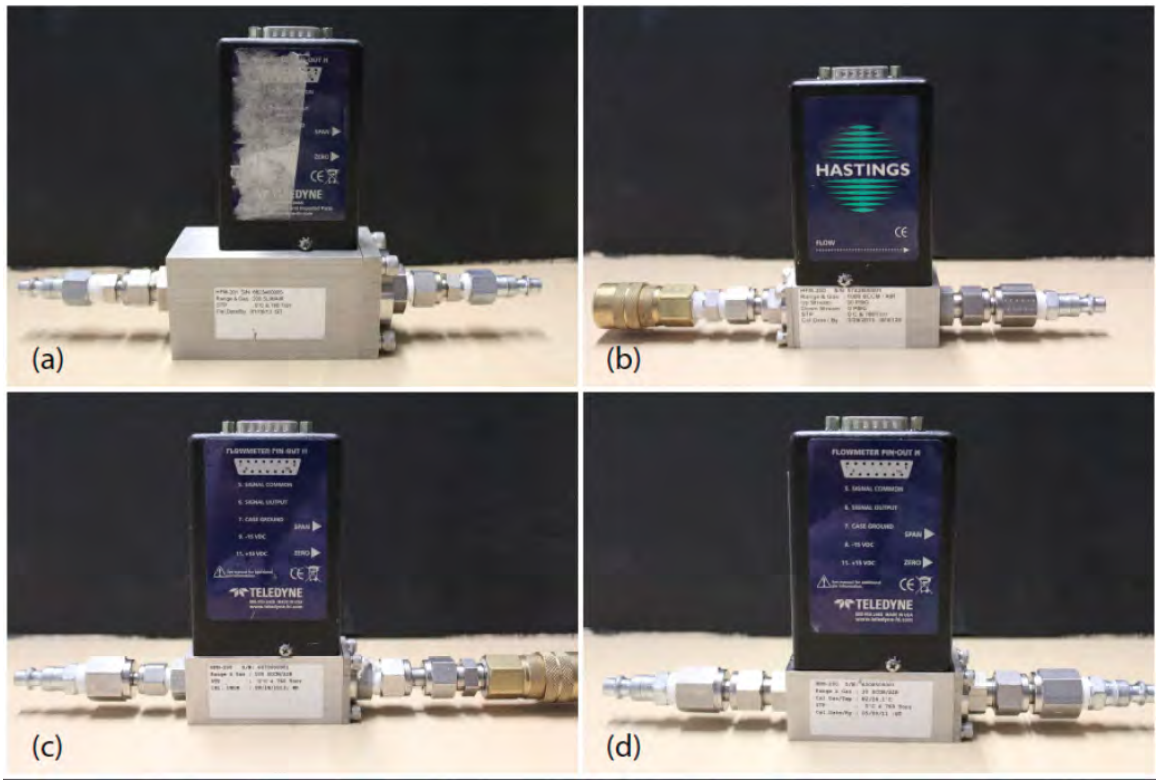

Figure B.3 : Four different flow meters used for gas permeametry. They are (a) 200 l/m, (b) 1000 cm^3/m, (c) 100 cm^3/m and (d) 30 cm^3/m. Typically, two or three meters are used for each sample measurement.

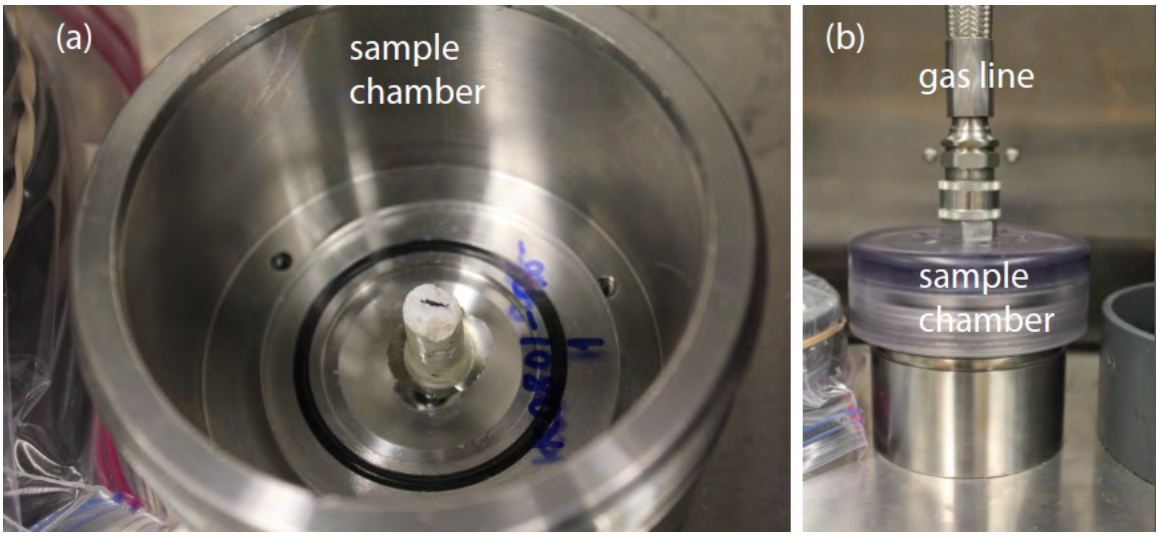

Figure B.4 : (a) Sample is placed inside the sample chamber. (b) The chamber is sealed off and connected to the gas line.

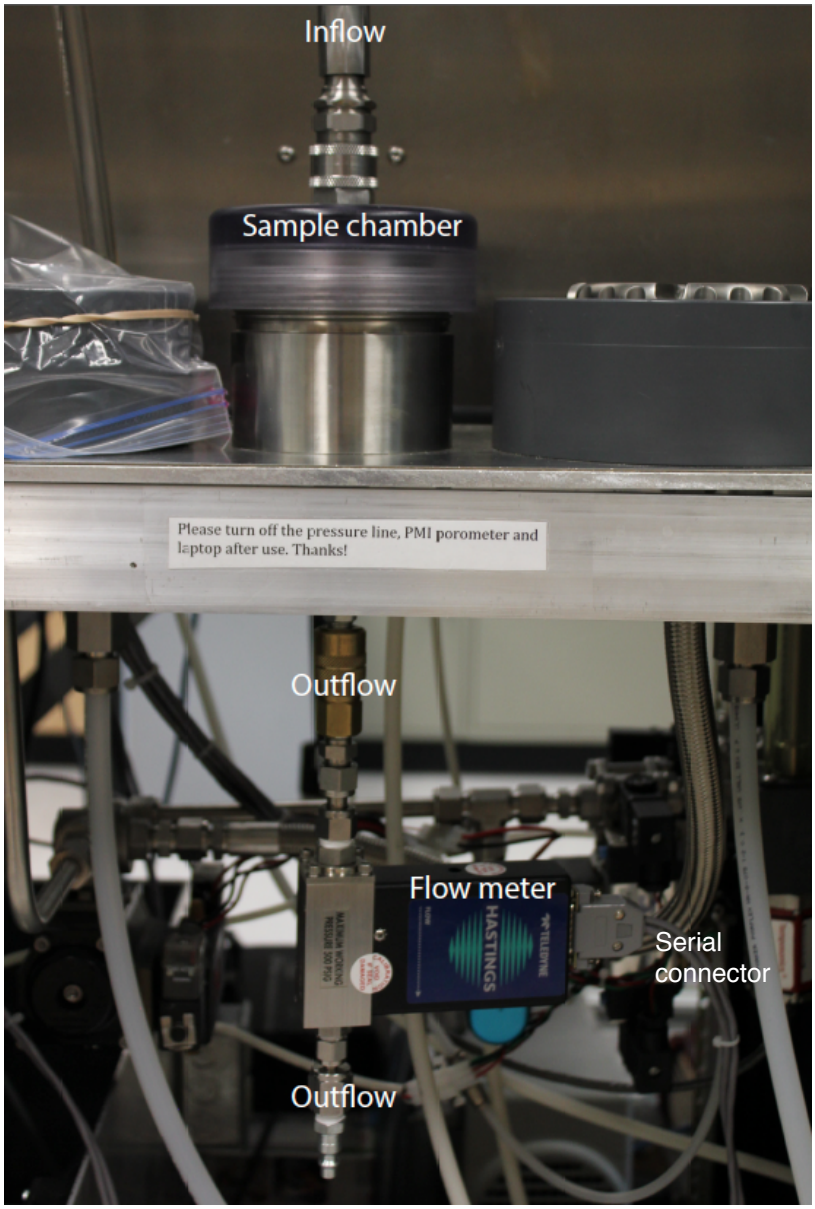

Figure B.5 : An image showing all the connections before measurement. The gas line of compressed air is connected to the sample chamber to allow inflow. A flow meter is connected to the other end of the sample to measure the volumetric flow rate.

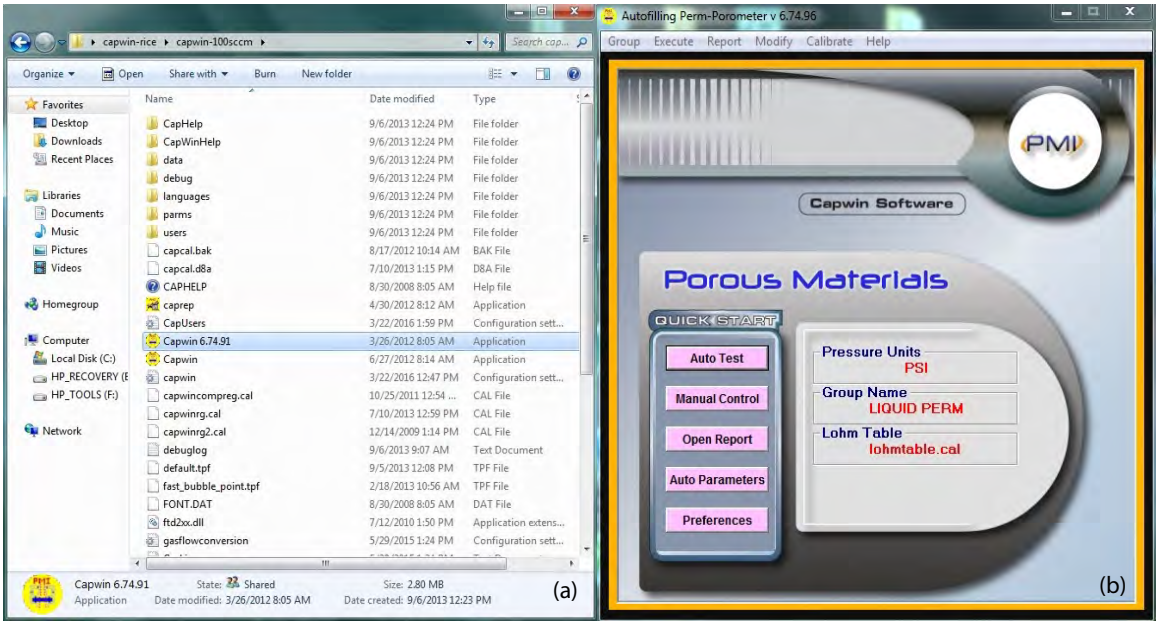

Figure B.6 : (a) The folder for choosing the proper software for the flow meter. If the flow meter of 100 cm^3/m is used, open the folder of 100 cm^3/m and choose the software Capwin 6.74.91(highlighted) (b) The software is open and ready for use.

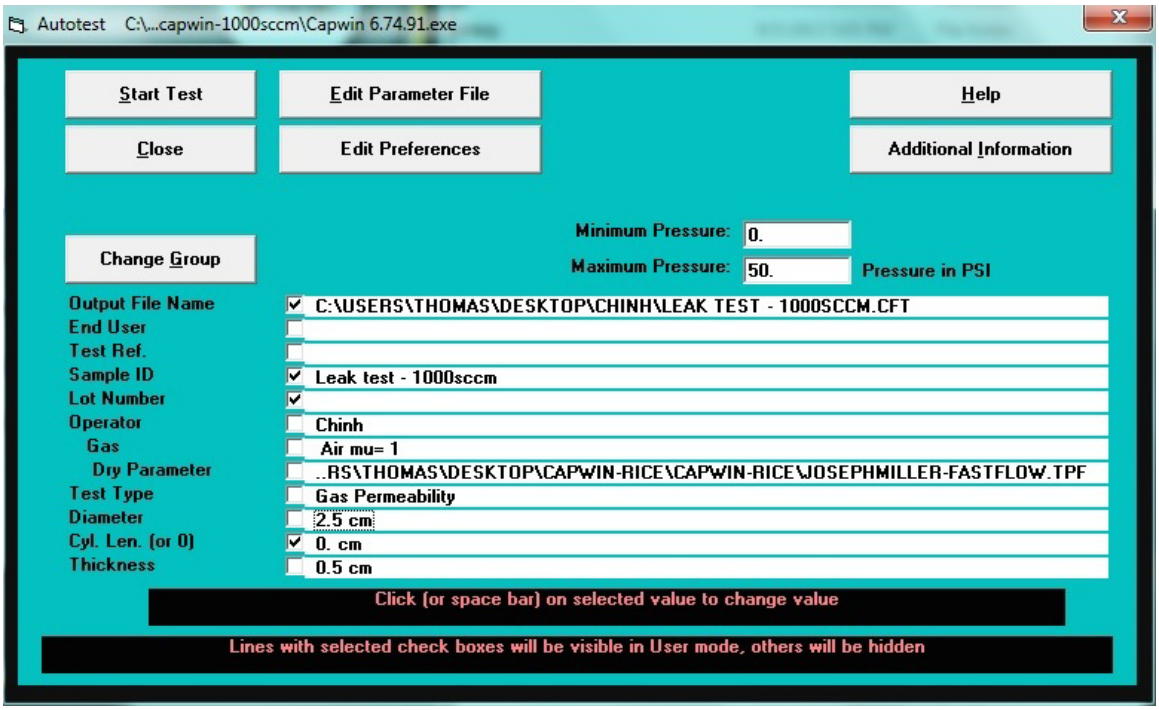

Figure B.7 : An image showing all the parameters needed for the measurement. Differential pressure range can be chosen from any value between 0 - 75 psi.

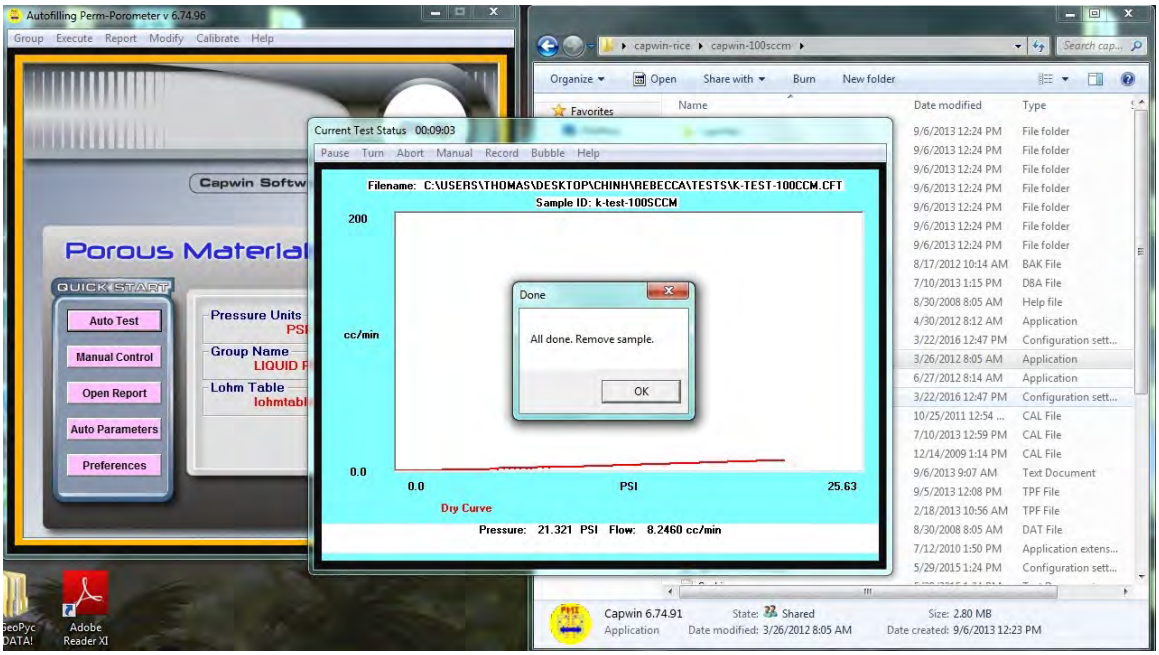

Figure B.8 : An image showing permeability measurement. Once the measurement is completed, a report shows the pressure gradient and volumetric flow rate (red).

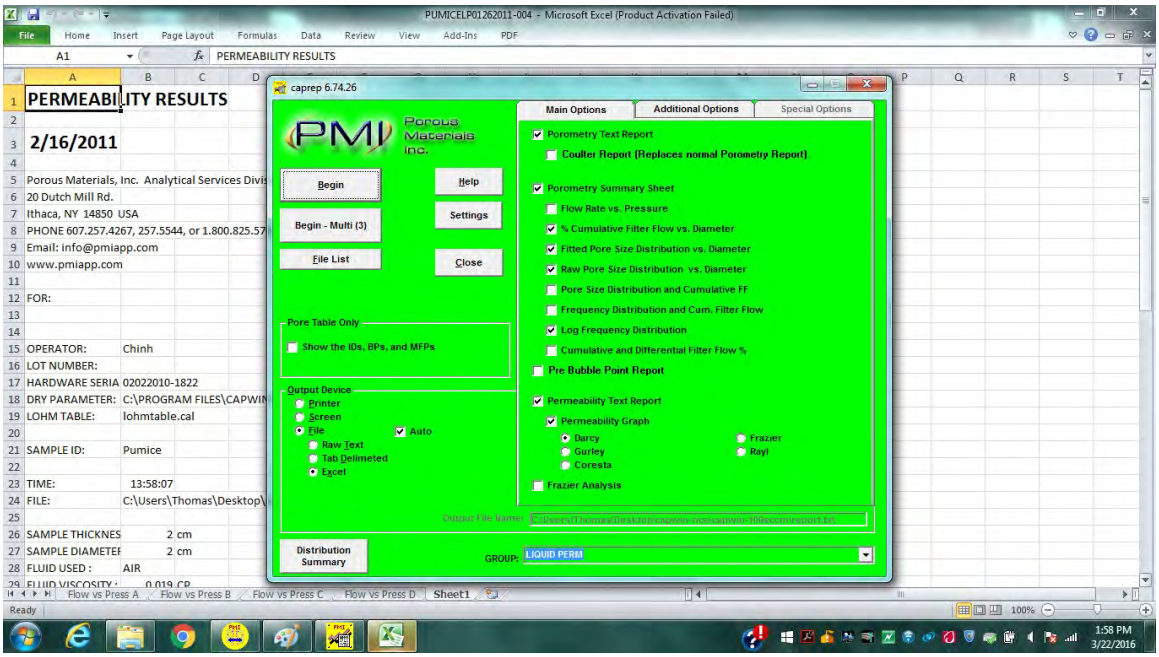

Figure B.9 : There are several options for output file. For all permeability values, use the raw data of pressure gradients and volumetric flow rates only. These data sets are then fitted using grid search method to obtain the best fit for Darcian and non-Darcian permeabilities.

Bibliography

Abid, S., and A. K. Chesters (1994), The drainage and rupture of partially mobile films between colliding drops at constant approach velocity, *Int. J. Multiphase Flow*, *20*, 613–629.

Adams, N. K., B. F. Houghton, S. A. Fagents, and W. Hildreth (2006a), The transition from explosive to effusive eruptive regime: The example of the 1912 Novarupta eruption, Alaska, *Geol. Soc. Amer. Bull.*, *118*, 620–634.

Adams, N. K., B. F. Houghton, and B. F. Hildreth (2006b), Abrupt transitions during sustained explosive eruptions: examples from the 1912 eruption of Novarupta, Alaska, *B. Volcanol.*, *69*, p. 189–206.

Alatorre-Ibargüengoitia, M. A., B. Scheu, D. B. Dingwell, H. Delgado-Granados, and J. Taddeucci (2010), Energy consumption by magmatic fragmentation and pyroclast ejection during Vulcanian eruptions, *Earth Planet Sci. Lett.*, *291*, 60–69, doi:10.1016/j.epsl.2009.12.051.

Alidibirov, M., and D. B. Dingwell (2000), Three fragmentation mechanisms for highly viscous magma under rapid decompression, *J. Volcanol. Geotherm. Res.*, *100*, 413–421, doi:10.1016/S0377-0273(00)00149-9.

Amon, M., and C. D. Denson (1984), A study of the dynamics of foam growth: analysis of the growth of closely spaced spherical bubbles, *Polymer Eng. Sci.*, *24*, 1026–1034.

Arefmanesh, A., and S. G. Advani (1991), Diffusion-induced growth of a gas bubble in a viscoelastic fluid, *Rheol. Acta*, *30*, 274–283.

Bagdassarov, N. S., A. Dorfman, and D. B. Dingwell (2000), Effect of alkalis, phosphorus, and water on the surface tension of haplogranite melt, *Am. Mineral.*, *85*, 33–40.

Bai, L., D. R. Baker, and M. Rivers (2008), Experimental study of bubble growth in Stromboli basalt melts at 1 atm, *Earth Planet. Sci. Lett.*, *267*, 533–547, doi: 10.1016/j.epsl.2007.11.063.

Baker, D. R., L. Mancini, M. Polacci, M. D. Higgins, G. A. R. Gualda, R. J. Hill, and M. L. Rivers (2012), An introduction to the application of X-ray microtomography to the three-dimensional study of igneous rocks, *Lithos.*, *148*, 262–276.

Blower, J. D. (2001), Factors controlling permeability - porosity relationships in magma, *B. Volcanol.*, *63*, 497–504.

Blower, J. D., J. P. Keating, H. M. Mader, and J. C. Phillips (2003), The evolution of bubble size distributions in volcanic eruptions, *J. Volcanol. Geotherm. Res.*, *120*, 1–23, doi:10.1016/S0377-0273(02)00404-3.

Blundy, J., and K. V. Cashman (2008), Petrologic reconstruction of magmatic system variables and processes, *Rev. Miner. Geochem.*, *69*, 179–239.

Bolster, D., R. E. Hershberger, and R. J. Donnelly (2011), Dynamic similarity, the dimensionless science, *Physics Today*, *64*, 42–47.

Burgisser, A., and J. E. Gardner (2005), Experimental constraints on degassing and permeability in volcanic conduit flow, *B. Volcanol.*, *67*, 42–56.

Carey, R., B. Houghton, S. Weaver, and S. Self (2013), Unsteady and steady phases of the Kaharoa 1314 AD eruption, Tarawera Volcano, New Zealand, *AGU Fall Meeting*.

Cashman, K. V., and M. Mangan (1994), Physical aspects of magmatic degassing II. Constraints on vesiculation processes from textural studies of eruption product, *Rev. Mineral.*, *30*, 477–478.

Cashman, K. V., M. Mangan, and S. Newman (1994), Surface degassing and modifications to vesicle size distributions in active basalt flows, *J. Volcanol. Geotherm. Res.*, *61*, 45–68, doi:10.1016/0377-0273(94)00015-8.

Castro, J. M., and J. E. Gardner (2008), Did magma ascent rate control the explosive-effusive transition at the Inyo volcanic chain, California?, *Geology*, *v. 36*, p. 279–282, doi:10.1130/G24453A.1.

Castro, J. M., A. Burgisser, C. I. Schipper, and S. Mancini (2012), Mechanisms of bubble coalescence in silicic magmas, *B. Volcanol.*, *74*, 2339–2352.

Castro, J. M., C. I. Schipper, S. P. Mueller, A. S. Militzer, A. Amigo, C. S. Parejas, and D. Jacob (2013), Storage and eruption of near-liquidus rhyolite magma at Cordon Caulle, Chile, *B. Volcanol.*, *v. 75*, p. 1–17, doi:10.1007/s00445-013-0702-9.

Chan, D. Y. C., E. Klaseboer, and R. Manica (2011), Film drainage and coalescence between deformable drops and bubbles, *Soft Matter*, *7*, 2235–2264.

Charles, G. E., and S. G. Mason (1960), The coalescence of liquid drops with flat liquid/liquid interfaces, *J. Colloid Sci.*, *15*, 236–267.

Chesters, A. K. (2009), Drainage of partially mobile films between colliding drops: a first order model, *Proc. Euromech.*, p. 234.

Chesters, A. K., and G. Hofman (1982), Bubble coalescence in pure liquids, *Appl. Scient. Res.*, *38*, 353–361.

Coombs, M. L., and J. E. Gardner (2001), Shallow storage conditions for the rhyolite of the 1912 eruption at Novarupta, Alaska, *Geology*, *v. 29*, p. 775–778, doi: 10.1130/0091-7613(2001)029<0775:SSCFTR>2.0.CO:2.

Coons, J. E., P. J. Halley, S. A. McGlashan, and T. Tran-Cong (2003), A review of drainage and spontaneous rupture in free standing thin films with tangentially immobile interfaces, *Adv. Colloid. Int. Sci.*, *105*, 3–62.

Cruz, F. G., and B. A. Chouet (1997), Long-period events, the most characteristic seismicity accompanying the emplacement and extrusion of a lava dome in Galeras Volcano, Colombia, in 1991, *J. Volcanol. Geotherm. Res.*, *77*, 121–158, doi: 10.1016/S0377-0273(96)00091-1.

Davis, S. S., and A. Smith (1976), Stability of hydrocarbon oil droplets at surfactant-oil interface, *Colloid. Polymer Sci.*, *254*, 82–99.

Debrégeas, G., P. G. de Gennes, and F. B. Wyart (1998), The life and death of ”bare” viscous bubbles, *Science*, *279*, 1704–1707.

Degruyter, W., O. Bachmann, and A. Burgisser (2010), Controls on magma permeability in the volcanic conduit during the climatic phase of the Kos Plateau Tuff eruption (Aegean Arc), *B. Volcanol.*, *72*, 63–74.

Degruyter, W., O. Bachmann, A. Burgisser, and M. Manga (2012), The effects of outgassing on the transition between effusive and explosive silicic eruptions, *Earth Planet. Sci. Lett.*, *349-350*, 161–170, doi:10.1016/j.epsl.2012.06.056.

Dingwell, D. B. (1996), Volcanic Dilemma: Flow or Blow, *Science*, *v. 273*, p. 1054–1055.

Dobran, F. (1992), Non-equilibrium flow in volcanic conduits and applications to the eruptions of Mount St. Helens, May 18, 1980 and Vesusius in A.D. 79, *J. Volcanol. Geotherm. Res.*, *49*, 285–311.

Donnelly-Nolan, J., M. Nathenson, D. Champion, D. Ramsey, J. Lowerstern, and J. Ewert (2007), Volcano Hazards Assessment for Medicine Lake Volcano, Northern California, *USGS - Scientific Investigation Report 5174-A*.

Eichelberger, J. C., C. R. Carrigan, H. R. Westrich, and R. H. Price (1986), Non-explosive silicic volcanism, *Nature*, *323*, 598–602.

Epel'baum, M. B., I. V. Babashov, and T. P. Salova (1973), Temperatures and pressures, *Geochem. Int.*, *10*, 343–345.

Fierstein, J., and W. Hildreth (1992), The plinian eruptions of 1912 at Novarupta, Katmai National Park, Alaska, *B. Volcanol.*, *v. 54*, p. 646–684.

Forchheimer, P. (1901), Wasserbewegung durch Boden, *Zeit. Ver. Deut. Ing.*, *v. 45*, p. 1781–1788.

Formenti, Y., and T. H. Druitt (2003), Vesicle connectivity in pyroclasts and implications for the fluidisation of fountain-collapse pyroclastic flows, Montserrat (West Indies), *Earth Planet. Sci. Lett.*, *214*, 561–574, doi:10.1016/S0012-821X(03)00386-8.

Gaonac'h, H., J. Stix, and S. Lovejoy (1996), Scaling effects on vesicle shape, size and heterogeneity of lavas from Mount Etna, *J. Volcanol. Geotherm. Res.*, *74*, 131–153, doi:10.1016/S0377-0273(96)00045-5.

Gaonac'h, H., S. Lovejoy, and D. Scherzter (2005), Scaling vesicle size distributions and volcanic eruptions, *B. Volcanol.*, *67*, 350–357.

Gardner, J. E. (2007), Bubble coalescence in rhyolitic melts during decompression from high pressure, *J. Volcanol. Geotherm. Res.*, *166*, 161–176, doi: 10.1016/j.jvolgeores.2007.07.006.

Gardner, J. E. (2012), Surface tension and bubble nucleation in phonolite magmas, *Geochim. Cosmochim. Acta*, *76*, 93–102.

Gardner, J. E., and R. A. Ketcham (2011), Bubble nucleation in rhyolite and dacite melts: temperature dependence of surface tension, *Contrib. Mineral. Petrol.*, *162*, 929–943.

Giachetti, T., T. H. Druit, A. Burgisser, L. Arbaret, and C. Galven (2010), Bubble nucleation, growth and coalescence during the 1997 Vulcanian explosions of Soufriere Hills Volcano, Montserrat, *J. Volcanol. Geotherm. Res.*, *193*, 215–231, doi:10.1016/j.jvolgeores.2010.04.001.

Giachetti, T., A. Burgisser, L. Arbaret, T. H. Druit, and K. Kelfoun (2011), Quantitative textural analysis of Vulcanian pyroclasts (Montserrat) using multi-scale X-ray computed microtomography: compared with results from 2D image analysis, *B. Volcanol.*, *73*, 1295–1309.

Giordano, D., J. K. Russell, and D. B. Dingwell (2008), Viscosity of mag-

matic liquids: A model, *Earth Planet. Sci. Lett.*, *271*, 123–134, doi: 10.1016/j.epsl.2008.03.038.

Gonde, C., C. Martel, M. Pichavanti, and H. Bureau (2011), In- situ bubble vesiculation in silicic magmas, *Am. Mineral.*, *96*, 111–124.

Gonnermann, H. M., and B. F. Houghton (2012), Magma degassing and fragmentation during the Plinian eruption of Novarupta, Alaska, 1912, *Geochem. Geophys. Geosyst.*, *13*, 1–20, doi:10.1029/2012GC004273.

Gonnermann, H. M., and M. Manga (2003), Explosive volcanism may not be an inevitable consequence of magma fragmentation, *Nature*, *426*, 432–435.

Gonnermann, H. M., and M. Manga (2007), The fluid mechanics inside a volcano, *Annu. Rev. Fluid Mech.*, *39*, 321–356.

Grove, T., and Donnelly-Nolan (1986), The evolution gf young silicic lavas at MIdicine Lake Volcano, California: Implications for the origin of compositional gaps in calc-alkaline series lavas, *Contrib. Mineral. Petro.*, *92*, 281–302.

Grove, T., J. Donnelly-Nolan, and T. Housh (1997), Magmatic processes that generated the rhyolite of Glass Mountain, Medicine Lake volcano, N. California, *Contrib. Mineral. Petro.*, *127*, 205–223.

Gurioli, L., B. F. Houghton, K. V. Cashman, and R. Cioni (2005), Complex changes in eruption dynamics during the 79 AD eruption of Vesuvius, *B. Volcanol.*, *67*, 144–159.

Hammer, J. E., M. J. Rutherford, and W. Hildreth (2002), Magma storage prior to

the 1912 eruption at Novarupta, Alaska, *Contrib. Mineral. Petro.*, *v. 144*, p. 144–162, doi:10.1007/s00410-002-0393-2.

Hartland, S. (1970), The profile of the drainage film between a fluid drop and a deformable fluid- liquid interface, *Chem. Eng. Sci.*, *1*, 67–75.

Heiken, G. (1978), Plinian-type eruptions in the Medicine Lake highland, California, and the nature of the underlying magma, *J. Volcanol. Geotherm. Res.*, *4*, 375–402.

Herd, R. A., and H. Pinkerton (1997), Bubble coalescence in basaltic lava: Its impact on the evolution of bubble populations, *J. Volcanol. Geotherm. Res.*, *75*, 137–157, doi:10.1016/S0377-0273(96)00039-X.

Hess, K. U., and D. B. Dingwell (1996), Viscosities of hydrous leucogranitic melts: A non-Arrhenian model, *Am. Mineral.*, *81*, 1297–1300.

Hildreth, W. (1991), The timing of caldera collapse at Mount Katmai in response to magma withdrawal toward Novarupta, *Geophys. Res. Lett.*, *18*, 1541–1544, doi: 10.1029/91GL01083.

Hildreth, W., and J. Fierstein (2000), Katmai volcanic cluster and the great eruption of 1912, *Geol. Soc. of Amer. Bull.*, *112*, 1594–1620.

Hildreth, W., and J. Fierstein (2012), The Novarupta-Katmai eruption of 1912 - largest eruption of the twentieth century: centennial perspectives, *U.S. Geological Survey, Professional Paper 1791*.

Hort, M., and J. Gardner (1998), Constraints on cooling and degassing of pumice

during Plinian volcanic eruptions based on model calculations, *J. Geophys. Res.*, *105*, 25,981–26,001.

Houghton, B., R. Carey, and M. Resenberg (2014), the 1800a Taupo eruption: "III wind" blows the ultraplinian type event down to Plinian, *Geology*, pp. 1–4, doi: 10.1130/jG35400.1.

Houghton, B. F., and C. J. N. Wilson (1989), A vesicularity index for pyroclastic deposits, *B. Volcanol.*, *51*, 451–462.

Houghton, B. F., R. J. Carey, K. V. Cashman, C. J. N. Wilson, B. J. Hobden, and J. E. Hammer (1998), Diverse patterns of ascent, degassing, and eruption of rhyolite magma during the 1.8 ka Taupo eruption, New Zealand: Evidence from clast vesicularity, *J. Volcanol. Geotherm. Res.*, *105*, 25,981–26,001, doi: 10.1016/j.jvolgeores.2010.06.002.

Hui, H., and Y. Zhang (2007), Toward a general viscosity equation for natural anhydrous and hydrous silicate melts, *Geochim. Cosmochim. Acta*, *71*, 403–416.

Ivanov, I. B., and T. T. Traykov (1976), Hydrodynamics of thin liquid films. Rate of thinning of emulsion films from pure liquids, *Int. J. Multiphase Flow*, *2*, 397–410.

Jaupart, C. (1998), Gas loss from magmas through a conduit walls during eruption, *Geol. Soc. Lond. Spec. Pub.*, *145*, 73–90.

Jaupart, C., and C. J. Allegre (1991), Gas content, eruption rate and instabilities of eruption regime in silicic volcanoes, *Earth Planet. Sci. Lett.*, *102*, 413–429, doi: 10.1016/0012-821X(91)90032-D.

Jones, A. F., and S. D. Wilson (1978), The film drainage problem in droplet coalescence, *J. Fluid Mech.*, *87*, 263–288.

Kerrick, D. M., and G. K. Jacobs (1981), A modified Redlich-Kwong Equation for H_2O, CO_2, and $H_2O - CO_2$ mixtures at elevated pressures and temperatures , *Am. J. Sci.*, *v. 281*, p. 735–767.

Khitarov, N. I., Y. B. Lebedev, A. M. Dorfman, and N. S. Bagdassarov (1979), Effects of temperature, pressure and volatiles on the surface tension of molten basalt, *Geochem. Int.*, *16*, 78–86.

Kline, S. J. (1986), *Similitude and Approximation Theory*, pp. 248 pp., Springer-Verlag New York Inc., New York.

Klug, C., and K. V. Cashman (1994), Vesiculation of May 18, 1980 Mount St. Helens magma, *Geology*, *22*, 468–472.

Klug, C., and K. V. Cashman (1996), Permeability development in vesiculating magmas: Implications for fragmentation, *B. Volcanol*, *58*, 87–100.

Klug, C., K. V. Cashman, and C. R. Bacon (2002), Structure and physical characteristics of pumice from climatic eruption of Mt. Mazama (Crater Lake), Oregon, *B. Volcanol.*, *64*, 486 – 501.

Kočárková, H. (), Stability of glass foams: Experiments at bubble scale and on vertical film, *Ph.D. dissertation*, *Université Paris - Est*.

Kočárková, H., F. Rouyer, and F. Pigeonneau (2013), Film drainage of viscous liquid on top of bare bubble: Influence of the Bond number, *Phys. Fluids*, *25*, doi:10.1063/1.4792,310.

Koyaguchi, T., and N. Mitani (2005), A theoretical model for fragmentation of viscous bubbly magmas in shock tubes, *J. Geophys. Res.*, *110*, B10,202, doi: 10.1029/2004JB003513.

Koyaguchi, T., B. Scheu, N. K. Mitani, and O. Melnik (2008), A fragmentation criterion for highly viscous bubbly magmas estimated from shock tube experiments, *J. Volcanol. Geotherm. Res.*, *178*, 58–71, doi:10.1016/j.jvolgeores.2008.02.008.

Larsen, J. F., M. H. Denis, and J. E. Gardner (2004), Experimental study of bubble coalescence in rhyolitic and phonolitic melts, *Geochim. Cosmochim. Acta*, *68*, 333–344.

Lautze, N. C., and B. F. Houghton (2007), Linking variable explosion style and magma textures during 2002 at Stromboli volcano, Italy, *B. Volcanol.*, *69*, 445–460.

Lee, J. C., and T. D. Hodgson (1968), Film flow and coalescence - I basic relations, film shape and criteria for interface mobility, *Chem. Eng. Sci.*, *23*, 1375–1397.

Lensky, N., V. Lyakhovsky, and O. Navon (2001), Radial variations of melt viscosity around growing bubbles and gas pverpressure in vesiculating magmas, *Earth Planet. Sci. Lett.*, *v. 186*, p. 1–6.

Leonard, G., J. Cole, I. Nairn, and S. Self (2002), Basalt triggering of the c. AD 1305 Kaharoa rhyolite eruption, Tarawera Volcanic Complex, New Zealand, *J. Volcanol. Geotherm. Res.*, *115*, 461–486.

Liu, Y., Y. X. Zhang, and H. Behrens (2005), Solubility of H_2O in rhyolitic melts at low pressures and a new empirical model for mixed $H_2O - CO_2$ solubility in rhyolitic melts, *J. Volcanol. Geotherm. Res.*, *v. 109*, B11,203.

Llewellin, E. W., and M. Manga (2005), Bubble suspension rheology and implications for conduit-flow, *J. Volcanol. Geotherm. Res.*, *143*, 205–217, doi: 10.1016/j.jvolgeores.2004.09.018.

Lovejoy, S., H. Gaonac'h, and D. Schertzer (2004), Bubble distributions and dynamics: The expansion- coalescence equation, *J. Geophys. Res.*, *109*, 1–16, doi: 10.1029/2003JB002823.

Mader, H. M., M. Zhang, J. C. Phillips, R. S. J. Sparks, B. Sturtevant, and E. Stolper (1994), Experimental simulations of explosive degassing of magma, *Nature*, *372*, 85–88.

Mader, H. M., M. Manga, and T. Koyaguchi (2004), The role of laboratory experiments in volcanology, *J. Volcanol. Geotherm. Res.*, *129*, 1–5, doi:10.1016/S0377-0273(03)00228-2.

Mader, M. T., E. W. Llewellin, and S. P. Mueller (2013), The rheology of two-phase magmas: A review and analysis, *J. Volcanol. Geotherm. Res.*, *v. 257*, p. 135–158.

Manga, M., and H. A. Stone (1994), Interactions between bubbles in magmas and lavas: Effects on bubble deformation, *J. Volcanol. Geotherm. Res.*, *63*, 267–279, doi: 10.1016/0377-0273(94)90079-5.

Manga, M., J. Castro, K. V. Cashman, and M. Loewenberg (1998), Rheology of bubble-bearing magmas, *J. Volcanol. Geotherm. Res.*, *87*, 15–28, doi: 10.1016/S0377-0273(98)00091-2.

Mangan, M. T., and K. V. Cashman (1996), The structure of basaltic scoria and reticulite and inferences for vesiculation, foam formation, and fragmentation in lava fountains, *J. Volcanol. Geotherm. Res.*, *73*, 1–18, doi:10.1016/0377-0273(96)00018-2.

Mangan, M. T., and T. Sisson (2005), Evolution of melt-vapor surface tension in silicic volcanic systems: Experiments with hydrous melts, *J. Geophys. Res.*, *110*, B01,202, doi:10.1029/2004JB003215.

Mangan, M. T., K. V. Cashman, and S. Newman (1993), Vesiculation of basaltic magma during eruption, *Geology*, *21*, 157–160.

Martula, D. S., T. Hasegawa, D. R. Lloyd, and R. T. Bonnecaze (2000), Coalescence-induced coalescence of inviscid droplets in a viscous fluid, *J. Colloid Sci.*, *232*, 241–253.

Mastin, L. G. (2002), Insights into volcanic conduit flow from an open-source numerical model, *Geochem., Geophys., Geosyst.*, *3*, 1–18, doi:10.1029/2001GC000192.

Melnik, O., and R. Sparks (1999), Nonlinear dynamics of lava dome extrusion, *Nature*, *v. 402*(no. 6757), p. 37–41.

Moitra, P., H. M. Gonnermann, B. F. Houghton, and T. Giachetti (2013), Relating vesicle shapes in pyroclasts to eruption styles, *B. Volcanol.*, *75*, 1–14.

Mueller, S., O. Melnik, O. Spieler, B. Scheu, and D. B. Dingwell (2005), Permeability and degassing of dome lavas undergoing rapid decompression: An experimental determination, *B. Volcanol.*, *67*, 526–538.

Mueller, S., B. Scheu, O. Spieler, and D. B. Dingwell (2008), Permeability control on magma fragmentation, *Geology*, *36*, 399–402.

Murase, T., and A. R. McBirney (1973), Properties of some common igneous rocks and their melts at high temperatures, *Geol. Soc. Am. Bull.*, *84*, 3563–3587.

Nairn, I. A., P. Shane, J. Cole, G. Leonard, S. Self, and N. Pearson (2004), Rhyolitic magma processes of the ∼AD 1314 Kaharoa eruption episode, Tarawera Volcano, New Zealand, *Volcanol. Geotherm. Res.*, *131*, 265–294.

Nairn, I. A., S. Self, J. Cole, G. Leonard, and C. Scutter (2010), Distribution, stratigraphy, and history of proximal deposits from the c. AD 1305 Kaharoa eruptive episode at Tarawera Volcano, New Zealand, *New Zealand J. Geol. and Geophys.*, *44:3*, 467–484, doi:10.1080/00288306.2001.9514950.

Nakamura, M., K. Otaki, and S. Takeuchi (2008), Permeability and pore-connectivity variations of pumices from a single pyroclastic eruption: Implications for partial fragmentation, *J. Volcanol. Geotherm. Res.*, *177*, 329–339, doi: 10.1016/j.jvolgeores.2008.04.011.

Namiki, A. (2012), An empirical scaling of shear-induced outgassing during magma ascent: Intermittent magma ascent causes effective outgassing, *Earth Planet. Sci. Lett.*, *353-354*, 72–81, doi:10.1016/j.epsl.2012.08.007.

Namiki, A., and M. Manga (2005), Response of a bubble bearing viscoelastic fluid to rapid decompression: Implications for explosive volcanic eruptions, *Earth Planet. Sci. Lett.*, *236*, 269–284, doi:10.1016/j.epsl.2005.02.045.

Namiki, A., and M. Manga (2008), Transition between fragmentation and permeable outgassing of low viscosity magmas, *J. Volcanol. Geotherm. Res.*, *169*, 48–60, doi:10.1016/j.jvolgeores.2007.07.020.

Navon, O., and V. Lyakhovsky (1998), Vesiculation processes in silicic magmas, *Geol. Soc. Lond. Spec. Pub.*, *145*, 27–50.

Nguyen, C., H. Gonnermann, Y. Chen, C. Huber, A. Maiorano, A. Gouldstone, and J. Dufek (2013), Film drainage and the lifetime of bubbles, *Geochem. Geophys. Geosyst.*, *14(9)*, 1–16, doi:10.1002/ggg3.20198.

Nguyen, C., H. Gonnermann, and B. Houghton (2014), Explosive to effusive transition during the largest eruption of the 20th century (Novarupta 1912, Alaska, *Geology*, *42*, 703–706, doi:10.1130/G35593.1.

Ohnesorge, W. (1936), Formation of drops by nozzles and the breakup of liquid jets, *J. App. Math. Mech.*, *16*, 355–358.

Okumura, S., M. Nakamura, and A. Tsuchiyama (2006), Shear-induced bubble coalescence in rhyolitic melts with low vesicularity, *J. Geophys. Res.*, *33*, 1–5, doi: 10.1029/2006GL027347.

Okumura, S., M. Nakamura, A. Tsuchiyama, T. Nakano, and K. Uesugi (2008), Evolution of bubble microstructure in sheared rhyolite: Formation of a channel-like bubble network, *J. Geophys. Res.*, *113*, 1–18, doi:10.1029/2007JB005362.

Oldenziel, G., R. Delfos, and J. Westerweel (2012), Measurements of liquid film thickness for a droplet at a two-fluid interface, *Phys. Fluids*, *24*, 022,106.

Pal, R. (2003), Rheology behavior of bubble- bearing magmas, *Earth Planet. Sci. Lett.*, *207*, 165–179, doi:10.1016/S0377-0273(98)00091-2.

Pigeonneau, F., and A. Sellier (2011), Low-Reynolds-number gravity-driven migration and deformation of bubbles near a free surface, *Phys. Fluids*, *23*, 092,102.

Polacci, M., P. Papale, and M. Rosi (2001), Textural heterogeneities in pumices

from the climatic eruption of Mount Pinatubo, 15 June 1991, and implications for magma ascent dynamics, *B. Volcanol.*, *63*, 83–97.

Polacci, M., D. R. Baker, L. Mancini, G. Tromba, and F. Zanini (2006), Three-dimensional investigation of volcanic textures by X-ray microtomography and implications for conduit processes, *Geophys. Res. Lett.*, *33*, L13,312, doi: 10.1029/2006GL026241.

Polacci, M., D. R. Baker, L. Bai, and L. Mancini (2008), Large vesicles record pathways of degassing at basaltic volcanoes, *B. Volcanol.*, *70*, 1023–1029.

Polacci, M., D. R. Baker, L. Mancini, S. Favretto, and R. J. Hill (2009), Vesiculation in magmas from Stromboli and implications for normal Strombolian activity and paroxysmal explosions in basaltic systems, *J. Geophys. Res.*, *114*, B01,206, doi: 10.1029/2008JB005672.

Princen, H. M. (1963), Shape of a fluid drop at a liquid-liquid interface, *J. Colloid Sci.*, *18*, 178–195.

Princen, H. M., M. P. Aronson, and J. C. Moser (1980), Highly concentrated emulsions, II. Real systems - The effect of film thickness and contact angle on the volume fraction in creamed emulsions, *J. Colloid. Int. Sci.*, *75*, 246–270.

Proussevitch, A. A., D. L. Sahagian, and V. A. Kutolin (1993a), Stability of foams in silicate melts, *J. Volcanol. Geotherm. Res.*, *59*, 161–178, doi:10.1016/0377-0273(93)90084-5.

Proussevitch, A. A., D. L. Sahagian, and A. T. Anderson (1993b), Dynamics of diffusive bubble growth in magmas: Isothermal case, *J. Geophys. Res.*, *98*, 22,283–22,307, doi:10.1029/93JB02027.

Qu, M., and A. Gouldstone (2008), On the role of bubbles in metallic splat nanopores and adhesion, *J. Therm. Spr. Tech.*, *17*, 486–595.

Qu, M., Y. Wu, V. Srinivasan, and A. Gouldstone (2007), Observations of nanoporous foam arising from impact and rapid solidification of molten Ni droplets, *Appl. Phys. Lett.*, *90*, 254,101–254,103.

Reynolds, O. (1900), Papers on mechanical and physical subjects, *Cambridge University Press*.

Rust, A., and M. Manga (2002), Bubble shapes and orientations in low Re simple shear flow, *J. Colloid Sci.*, *249*, 476–480.

Rust, A. C., and K. V. Cashman (2004), Permeability of vesicular silicic magma: Inertial and hysteresis effects, *Earth Planet. Sci. Lett.*, *228*, 93–107, doi: 10.1016/j.epsl.2004.09.025.

Rust, A. C., and K. V. Cashman (2011), Permeability controls on expansion and size distributions of pyroclasts, *J. Geophys. Res.*, *116*, doi:0.1029/2011JB008494.

Rutherford, M. J. (2008), Magmas ascent rates, *Rev. Miner. Geochem.*, *69*, 241–271.

Rutherford, M. J., and P. M. Hill (1993), Magmas ascent rates from amphibole breakdown: An experimental study applied to the 1980 - 1986 Mt. St. Helens eruptions, *J. Geophys. Res.*, *98*, 19,678–19,685, doi:10.1029/93JB01613.

Saar, M. O., and M. Manga (1999), Permeability - porosity relationship in vesicular basalts, *Geophys. Res. Lett.*, *26*, 111–114, doi:10.1029/1998GL900256.

Sahetapy-Engel, S., S. Self, R. Carey, and I. Nairn (2014), Deposition and generation

of multiple widespread fall units from the *c.* AD 1305 Kaharoa rhyolite eruption, Tarawera, New Zealand, *B. Volcanol.*, *76*, 836–864, doi:10.1007/s0445-014-0836-4.

Shea, T., B. F. Houghton, L. Gurioli, K. V. Cashman, J. E. Hammer, and B. J. Hobden (2010), Textural studies of vesicles in volcanic rocks: An integrated methodology, *J. Volcanol. Geotherm. Res.*, *190*, 271–289, doi:10.1016/j.jvolgeores.2009.12.003.

Sheludko, A. D. (1966), *Colloid Chemistry*, 277 pp., Elsevier, New York, U.S.A.

Smith, R., and B. Houghton (1995), Vent migration and change in eruption style during the 1800a Taupo eruption: new evidence from the Hatepe and Rotongaio phreatoplinian ashes, *B. Volcanol.*, *57*, p. 432–439.

Sparks, R. S. J. (1978), The dynamics of bubble formation and growth in magmas, *J. Volcanol. Geotherm. Res.*, *3*, 1–37, doi:10.1016/0377-0273(78)90002-1.

Sparks, R. S. J., and S. Brazier (1982), New evidence for degassing processes during explosive eruptions, *Nature*, *295*, 218–220.

Spieler, O., B. Kennedy, U. Kueppers, D. B. Dingwell, B. Scheu, and J. Taddeucci (2004), The fragmentation threshold of pyroclastic rocks, *Earth Planet. Sci. Lett.*, *226*, 139–148, doi:10.1016/j.epsl.2004.07.016.

Stasiuk, M., C. Jaupart, and R. J. S. Sparks (1993), On the variations of flowrate in non-explosive lava eruptions, *Earth Planet. Sci. Lett.*, *114*, p. 505–516, doi: 10.1016/0012-821X(93)90079-O.

Stein, D. J., and F. J. Spera (1992), Rheology and microstructure of magmatic emulsions: Theory and experiments, *J. Vocanol. Geotherm. Res.*, *49*, 157–174, doi: 10.1016/0377-0273(92)90011-2.

Stone, H. A. (1994), Dynamics of drop deformation and breakup, *Annu. Rev. Fluid Mech.*, *26*, 65–102.

Takeuchi, S., S. Nakashima, A. Tomiya, and H. Shinohara (2005), Experimental constraints on the low gas permeability of vesicular magma during decompression, *Geophys. Res. Lett.*, *32*, L10,312.

Takeuchi, S., A. Tomiya, and H. Shinohara (2009), Degassing conditions for permeable silicic magmas: Implications from decompression experiments with constant rates, *Earth Planet. Sci. Lett.*, *283*, 101–110, doi:10.1016/j.epsl.2009.04.001.

Taniguchi, H. (1988), Surface tension of melts in the system $CaMgSi_2O_6$ - $CaAl_2Si_2O_8$ and its structural significance, *Contrib. Mineral. Petrol.*, *100*, 484–489.

Tarantola, A. (1987), *Inverse Problem Theory*, Elsevier Scientific Publishing Company.

Thomas, R. M. E., and R. S. J. Sparks (1992), Cooling of tephra during fallout from eruption columns, *B. Volcanol.*, *54*, 542–553.

Toramaru, A. (1988), Formation of propagation pattern in two-phase flow systems with applications to volcanic eruptions, *Geophys. J.*, *95*, 613–623, doi: 10.1111/j.1365-246X.1988.tb06707.x.

Toramaru, A. (1989), Vesiculation process and bubble size distribution in ascending magmas with constant velocities, *J. Geophys. Res.*, *94*, 17,523–17,542, doi: 10.1029/JB094iB12p17523.

Toramaru, A. (1990), Measurement of bubble size distribution in vesiculated rocks

with implications for quantitative estimation of eruption processes, *J. Volcanol. Geotherm. Res.*, *43*, 71–90, doi:10.1016/0377-0273(90)90045-H.

Toramaru, A. (2006), BND (bubble number density) decompression rate meter for explosive volcanic eruptions, *J. Volcanol. Geotherm. Res.*, *154*, 303–316, doi: 10.1016/j.jvolgeores.2006.03.027.

Traykov, T. T., E. D. Manev, and I. B. Ivanov (1977), Hydrodynamics of thin liquid films. Experimental investigation of the effect of surfactants on the drainage of emulsion films, *Int. J. Multiphase Flow*, *3*, 485–494.

Tuffen, H., D. B. Dingwell, and H. Pinkerton (2003), Repeated fracture and healing of silicic magma generate flow banding and earthquakes?, *Geology*, *v. 31*, p. 1089–1092, doi:10.1130/G19777.1.

van der Schaaf, J., and R. G. C. Beerkens (2006), A model for foam formation, stability, and breakdown in glass-melting furnaces, *J. Colloid. Inter. Sci.*, *295*, 218–229.

Vergniolle, S. (1986), Bubble size distribution in magma chambers and dynamics of basaltic eruptions, *J. Geophys. Res.*, *91*, 12,842 –12,860, doi:10.1016/0012-821X(96)00042-8.

Walker, D., and O. Mullins (1981), Surface tension of natural silicate melts from 1,200 - 1,500 , and implications for melt structure, *Contrib. Mineral. Petrol.*, *76*, 455–462.

Westrich, H. R., and J. C. Eichelberger (1994a), Gas transport and bubble collapse in rhyolitic magma: an experimental approach, *B. Volcanol.*, *56*, 447–458.

Westrich, H. R., and J. C. Eichelberger (1994b), Gas transport and bubble collapse in rhyolitic magma: an experimental approach, *B. Volcanol.*, *v. 56*, p. 447–458.

Whitham, A. G., and R. S. J. Sparks (1986), Pumice, *B. Volcanol.*, *48*, 209–223.

Wilson, C. (1993), Stratigraphy, chronology, styles and dynamics of late Quaternary eruptions from Taupo volcano, New Zealand, *Phil. Trans. R. Soc. Lond.*, *A343*, p. 205–306.

Wilson, C., and G. Walker (1985), The Taupo eruption, New Zealand. I. General aspects, *Phil. Trans R. Soc. Lond.*, *314*, 199–228.

Wilson, L. (1980), Relationship between pressure, volatile content and ejecta velocity in three types of volcanic explosion, *J. Volcanol. Geotherm. Res.*, *8*, 297–313, doi:10.1016/0377-0273(80)90110-9.

Woods, A. W., and T. Koyaguchi (1994), Transitions between explosive and effusive eruptions of silicic magmas, *Nature*, *370*, 641–644.

Wright, H. M. N., J. J. Roberts, and K. V. Cashman (2006), Permeability of anisotropic tube pumice: Model calculations and measurements, *Geophys. Res. Lett.*, *33*, doi:10.1029/2006GL027224.

Wright, H. M. N., K. V. Cashman, M. Rosi, and R. Cioni (2007), Breadcrust bombs as indicators of Vulcanian eruption dynamics at Guagua Pinchincha volcano, Ecuador, *B. Volcanol.*, *69*, 281–300.

Wright, H. M. N., K. V. Cashman, E. H. Gottesfeld, and J. J. Roberts (2009), Pore structure of volcanic clasts: Measurements of permeability and electrical conductivity, *Earth Planet. Sci. Lett.*, *280*, 93–104, doi:10.1016/j.epsl.2009.01.023.

Yiantsios, S. G., and R. H. Davis (1991), Close approach and deformation of two viscous drops due to gravity and van der waals forces, *J. Colloid Sci.*, *144*, 412–433.